UNIVERSIDADE FEDERAL DE JUIZ DE FORA
FACULDADE DE ENGENHARIA
PROGRAMA DE PÓS-GRADUAÇÃO EM ENGENHARIA ELÉTRICA

Felipe Oliveira Barino

Machine Learning-Based long-period fiber grating demodulation: A promising tool for cost-effective in-field implementation

Juiz de Fora
2025

Felipe Oliveira Barino

Machine Learning-Based long-period fiber grating demodulation: A promising tool for cost-effective in-field implementation

Thesis submitted to the Programa de Pós-Graduação em Engenharia Elétrica at the Universidade Federal de Juiz de Fora as a partial requirement for obtaining the title of Doctor in Electrical Engineering. Concentration area: Electronic Systems.

Advisor: Prof. Dr. Alexandre Bessa dos Santos

Juiz de Fora

2025

Barino, Felipe.

Machine Learning-Based long-period fiber grating demodulation : A promising tool for cost-effective in-field implementation / Felipe Oliveira Barino. – 2025.

91 f. : il.

Advisor: Alexandre Bessa dos Santos

Thesis (PhD) – Universidade Federal de Juiz de Fora, Faculdade de Engenharia. Programa de Pós-Graduação em Engenharia Elétrica, 2025.

1. Optical sensors. 2. Wavelength demodulation. 3. Machine learning. I. Santos, Alexandre Bessa dos, orient. II. Title.

FEDERAL UNIVERSITY OF JUIZ DE FORA
RESEARCH AND GRADUATE PROGRAMS OFFICE

Felipe Oliveira Barino

Machine learning based long-period fiber grating demodulation: a promising tool for cost-effective in-field implementation

Thesis submitted to the Graduate Program in Electrical Engineering
of the Federal University of Juiz de Fora as a partial requirement
for obtaining a Doctor's degree in Electrical Engineering.
Concentration area: Electronic Systems

Approved on 21 of January of 2025.

EXAMINING BOARD

Prof. Dr. Alexandre Bessa dos Santos – Academic Advisor
Federal University of Juiz de Fora

Prof. Dr. Andrés Pablo López Barbero
Fluminense Federal University

Prof. Dr. Arnaldo Gomes Leal Junior
Federal University of Espírito Santo

Prof. Dr. André Luis Marques Marcato
Federal University of Juiz de Fora

Prof. Dr. Guilherme Márcio Soares
Federal University of Juiz de Fora

Juiz de Fora, 01/09/2025.

Documento assinado eletronicamente por **Arnaldo Gomes Leal Junior**, **Usuário Externo**, em 21/01/2025, às 17:12, conforme horário oficial de Brasília, com fundamento no § 3º do art. 4º do Decreto nº 10.543, de 13 de novembro de 2020.

Documento assinado eletronicamente por **Guilherme Márcio Soares**, **Professor(a)**, em 21/01/2025, às 17:13, conforme horário oficial de Brasília, com fundamento no § 3º do art. 4º do Decreto nº 10.543, de 13 de novembro de 2020.

Documento assinado eletronicamente por **Alexandre Bessa dos Santos**, **Professor(a)**, em 21/01/2025, às 17:14, conforme horário oficial de Brasília, com fundamento no § 3º do art. 4º do Decreto nº 10.543, de 13 de novembro de 2020.

Documento assinado eletronicamente por **Andres PAblo Lopez Barbero**, **Usuário Externo**, em 21/01/2025, às 17:14, conforme horário oficial de Brasília, com fundamento no § 3º do art. 4º do Decreto nº 10.543, de 13 de novembro de 2020.

Documento assinado eletronicamente por **Andre Luis Marques Marcato**, **Professor(a)**, em 21/01/2025, às 17:14, conforme horário oficial de Brasília, com fundamento no § 3º do art. 4º do Decreto nº 10.543, de 13 de novembro de 2020.

A autenticidade deste documento pode ser conferida no Portal do SEI-Ufjf (www2.ufjf.br/SEI) através do ícone Conferência de Documentos, informando o código verificador **2185480** e o código CRC **C651772E**.

ACKNOWLEDGEMENTS

I would like to thank the financial support from the Coordenação de Aperfeiçoamento de Pessoal de Nível Superior (CAPES), Instituto Nacional de Energia Elétrica (INERGE), Fundação de Amparo à Pesquisa do Estado de Minas Gerais (FAPEMIG), and Santo Antônio Energia.

RESUMO

Grades de longo período em fibra (LPGs) são dispositivos versáteis e fabricados dentro de fibras ópticas, e um dos seus usos é a fabricação de sensores ópticos. Tais sensores têm ganhado atenção significativa nos últimos anos devido às suas capacidades únicas de detecção e facilidade de fabricação. No entanto, sua adoção generalizada tem sido dificultada pela complexidade e custo dos métodos tradicionais de interpretação (interrogação) dos seus dados, que muitas vezes dependem de equipamentos volumosos e caros. Nesta tese, uma nova abordagem para a interrogação de LPGs é apresentada. Ela usa um banco de filtros ópticos esparsos e algoritmos de aprendizado de máquina para alcançar medições econômicas e confiáveis. A abordagem proposta é investigada através de três métodos distintos, cada um construído sobre o anterior, culminando em uma rede neural totalmente conectada baseada em autoatenção. Essa abordagem permite o uso de FBGs com posições arbitrárias em uma configuração multissensor, melhorando a relação custo-benefício do sistema e incorporando recursos de detecção multiponto. Os resultados demonstram a eficácia da abordagem proposta, mostrando sua alta precisão, robustez ao ruído e capacidade de generalização para uma ampla gama de sensores LPG e configurações de sensores FBG. Foi possível obter resoluções na ordem de nanometros com a abordagem proposta. Com o uso de sistemas fuzzy e FBGs estáticas, foi possível estimar a posição do sensor LPG com incerteza de 0.481 nm com baixa sensibilidade ao ruído com relação sinal-ruído de 20 a 12 dB, sem impacto na resolução do sistema. Em topologias mais complexas, em que as FBGs atuam como sensores, a incerteza foi de 0.687 nm usando um modelo de auto-atenção treinado com dados sintéticos. O uso de dados sintéticos para treinamento supera as limitações de aquisição de grandes conjuntos de dados, permitindo o desenvolvimento de modelos mais robustos e complexos. Para avaliar a efetividade da técnica proposta, um sensor de índice de refração foi construído e interrogado pelo sistema proposto com erro menor que 0.2%. Esta tese deve contribuir significativamente para o campo da interrogação de sensores LPG, oferecendo uma solução promissora para várias aplicações, principalmente no monitoramento de saúde estrutural, sensoriamento ambiental e controle de processos industriais. A abordagem proposta abre caminho para avanços adicionais na tecnologia de sensoriamento LPG e sua ampla adoção em campo.

Palavras-chave: sensores a fibra óptica; demodulação de comprimento de onda; aprendizado de máquinas; sensoriamento quasi-distribuído.

ABSTRACT

Long-period fiber gratings (LPGs) are versatile optical fiber devices, and one of their uses is the manufacture of optical sensors. These sensors have gained significant attention in recent years due to their unique detection capabilities and ease of manufacturing. However, their widespread adoption has been hindered by the complexity and cost of traditional interrogation methods, which often rely on bulky and expensive equipment. This thesis presents a novel approach to LPG interrogation that leverages a sparse optical filter bank and machine learning algorithms to achieve cost-effective and reliable measurements. The proposed approach is investigated through three distinct methods, each building upon the previous one, culminating in a fully connected neural network based on self-attention. This approach enables the use of FBGs with arbitrary positions in a multi-sensor configuration, enhancing system cost-effectiveness by sensor multiplexing and incorporating multi-point sensing capabilities. The results demonstrate the effectiveness of the proposed approach by demonstrating its high accuracy, robustness to noise, and ability to generalize to a wide range of LPG sensors and FBG array configurations. The use of synthetic data for training overcomes the limitations of acquiring large datasets, allowing for the development of more robust and complex models. To assess the effectiveness of the proposed technique, a refractive index sensor was built and interrogated by the proposed system with an error less than 0.2%. This thesis should contribute significantly to the field of LPG sensor interrogation, offering a promising solution for various applications, mainly in structural health monitoring, environmental sensing, and industrial process control. The proposed approach paves the way for further advances in LPG sensing technology and its widespread adoption in the field.

Keywords: optical fiber sensors; wavelength demodulation; machine learning; quasi-distributed sensing.

LIST OF ILLUSTRATIONS

LIST OF TABLES

LIST OF ABBREVIATIONS

OSA	Optical spectrum analyser
FBG	Fiber Bragg Grating
LPG	Long-period fiber grating
SRI	Surrounding refractive index
RIU	Refractive index unit
FWHM	Full width at half maximum
ML	Machine learning
AI	Artificial intelligence
ANN	Artificial neural network
MLP	Multilayer perceptron
ReLU	Rectified linear unit
SA-FCN	Self-attention fully connected network
FIS	Fuzzy inference system
GA	Genetic algorithm
AWGN	Additive white gaussian noise
MAE	Mean absolute error
MAPE	Mean absolute percentage error
MSE	Mean squared error
RMSE	Root mean squared error
SNR	Signal-to-noise ratio
GUM	Guide for uncertainty in measurement

SUMMARY

1 INTRODUCTION

This thesis presents a study on the use of machine learning to estimate the spectral position of a long-period fiber grating sensor using a set of sparse optical filters. The long-period fiber grating sensor is a promising technology in the field of optical fiber sensing due to its ease of manufacturing, sensitivity, and flexible application. However current signal demodulation techniques for these devices lack practical and cost-effective approaches. The following sections of this chapter, respectively, presents the research problem, this document outline, and the papers published during the doctorate period at the Programa de Pós-graduação em Engenharia Elétrica.

1.1 THE RESEARCH PROBLEM

Optical fiber sensors have emerged as a versatile and powerful technology, offering numerous advantages over traditional sensing methods. Some advantages are immunity to electromagnetic interference, resilience in harsh environments, and the ability to transmit signals over long distances with low loss [1]. This technology has experienced significant growth due to its ability to measure a wide range of parameters, with applications in diverse fields such as structural health monitoring [2–4], environmental sensing [5, 6], various industrial process control applications [7–9], and biomedicine [10–12].

Among the various types of optical fiber sensors, particularly point sensors, diffraction-based sensors such as Fiber Bragg Gratings (FBGs) and Long Period Fiber Gratings (LPGs) have attracted significant attention due to their simplicity, compactness, and ease of implementation [13]. While FBGs have been extensively researched and have made significant strides toward industrial application, LPGs have gained prominence in recent years due to their unique sensing capabilities, high sensitivity, simple manufacturing, and ability to measure a wide range of physical parameters, including temperature, strain, and refractive index [14, 15], but still mainly limited to research-level solutions and lab-use.

The intrinsic refractive index sensitivity of LPGs is crucial for enabling a wide range of indirect measurements and is a desirable attribute for their use in sensing applications. Indeed, this sensitivity has been leveraged in LPG sensors for food quality monitoring [16, 17], label-free biochemical detection [10, 18], and environmental wear assessment of structures [19, 20]. Although such sensitivity might introduce cross-sensitivity errors, the a multi-parameter or multi-sensor system solves such errors. Additionally, the complex spectral nature of LPGs presents sufficient information to enable single-device multi-parameter sensing that could provide self-compensation and multi-dimensional sensing [21–24].

Besides these advantages related to the instrumentation and measurement aspects of LPG technology, there is a crucial practical advantage: LPGs are relatively easy and

inexpensive to manufacture compared to FBGs. Direct-write techniques, such as arc-discharge [25–27], laser irradiation [28–30], and laser scanning [31, 32], can be readily employed to fabricate high-quality devices. Dynamic LPGs have also been reported using mechanical deformations [33, 34]. These factors contribute to the growing promise of LPG technology as a versatile and cost-effective sensing platform.

However, LPGs have not experienced the leap that FBGs have in the recent past. The FBG sensing technology holds far more use cases outside a research lab. The technology has matured enough, so one can find several industrial grade FBG sensing systems readily available. For LPGs the main problem lies in the optical signal interpretation and overall cost-effectiveness. The LPG spectrum makes the acquisition system complex and often limited to a single sensor. For FBGs, on the other hand, the signal is easily interpretable and a multi-point system is easily accomplished. A compact optical spectrum analyzer, optimized for FBG interrogation, can efficiently interrogate up to tens of FBG sensors in parallel through wavelength multiplexing. In contrast, LPGs, due to their spectral complexity, typically require individual interrogation, limiting the number of sensors that can be monitored simultaneously. This fundamental difference leads to a significantly lower cost per sensor for FBG-based systems..

In this work, a novel machine learning methodology is presented as a promising solution to help the LPG technology shift towards broader in-field applications. The solution is to use several FBGs as filters to extract power spectral features of the LPG sensor and estimate the LPG resonant wavelength, the most important LPG feature for sensing. Furthermore, given the sensing capability of FBGs, this work culminates in a multi-sensor scheme whereas the filters also act as sensing elements, further improving the cost-effectiveness of the system by sensor multiplexing.

1.2 OUTLINE OF THE THESIS

The thesis comprises seven chapters, with the current chapter serving as an introduction to the research topic and the overall structure of the work. The subsequent chapters are designed to be self-contained, allowing readers to focus on specific aspects of interest without relying heavily on other chapters.

Chapter 2 provides an overview of the LPG interrogation problem, presenting a general outline of LPG technology and the current state-of-the-art in interrogation techniques. The chapter begins with a brief theoretical foundation on fiber grating devices and their use as sensors. It then discusses common techniques for LPG interrogation, as well as the latest research developments in this area.

Chapters 3, 4, 5, and 6 explore the application of machine learning to LPG interrogation. Each chapter is derived from a paper published by the author and details the methodology and results of the given application.

Chapter 3 presents the use of a static FBG array to estimate the resonant wavelength of LPGs using a neural network. Chapter 4 refines this implementation by updating the preprocessing methodology and employing a fuzzy inference system for estimation. Chapter 5 proposes the utilization of the Monte Carlo method to address uncertainty propagation through the previously reported models.

Chapter 6 introduces the use of non-static FBGs, forming a comprehensive multi-sensor network. To develop this system, a more complex model was needed and a novel training perspective is proposed, using synthetic LPG spectra to train such model. The model incorporated self-attention and embedded uncertainty estimation using layers. This approach holds significant promise for LPG sensors, as it leverages field-proven, commercially available devices to interrogate both LPG and FBG sensors, thereby establishing a complex and robust multi-point, and multi-parameter, sensing network.

Finally, in Chapter 7 the conclusion of this thesis are presented.

1.3 PUBLISHED PAPERS

In this section the papers published in peer-reviewed journals during the PhD research is presented. The papers were separated into those regarding the LPG interrogation problem and those regarding other aspects of the optical fiber sensing.

1.3.1 LPG interrogation

Below a list of the papers published in the field of LPG interrogation, note that the older research paper was the motivation for this PhD research.

- BARINO, F. O.; D. SANTOS, A. B.; DOS SANTOS, A. B. LPG interrogator based on FBG array and artificial neural network. *IEEE Sensors Journal*, v. 20, p. 14187–14194, 12 2020
- SAMPAIO, G.; BARINO, F. O.; DOS SANTOS, A. B. Long-period fiber grating sensor interrogation with single strain modulated FBG and harmonic analysis. *Optical Fiber Technology*, v. 71, p. 102940, 7 2022
- BARINO, F. O.; AGUIAR, E. P. D.; HONóRIO, L. D. M.; SILVA, V. N. H.; LóPEZ-BARBERO, A. P.; SANTOS, A. B. D. A fuzzy approach to LPFG-based optical sensor processing and interrogation. *IEEE Transactions on Instrumentation and Measurement*, v. 71, 2022
- BARINO, F. O.; DOS SANTOS, A. B. Addressing uncertainty on machine learning models for long-period fiber grating signal conditioning using monte carlo method. *IEEE Transactions on Instrumentation and Measurement*, v. 73, p. 1–9, 2024

1.3.2 Other research on optical fiber sensing

Some contributions were regarding applications of optical fiber sensors, mostly LPGs.

- BARINO, F. O.; FARACO-FILHO, R. L.; CAMPOS, D.; DOS SANTOS, A. B. 3d-printed force sensitive structure using embedded long-period fiber grating. *Optics & Laser Technology*, v. 148, p. 107697, 4 2022
- FILHO, R. L. F.; BARINO, F. O.; CALDERANO, J.; ÍTALO FERNANDO VALLE ALVARENGA; CAMPOS, D.; DOS SANTOS, A. B. In-fiber mach–zehnder interferometer as a promising tool for optical nose and odor prediction during the fermentation process. *Optics Letters*, v. 48, p. 3905, 8 2023
- FARACO-FILHO, R.; CASTRO, J. V. D.; BARINO, F. O.; CAMPOS, D. E.; SANTOS, A. B. D. Monitoring and characterization technology for coffee fermentation aromas: A data-driven approach. *IEEE Sensors Journal*, v. 24, p. 8371–8378, 3 2024
- FILHO, R. L. F.; DE CASTRO, J. V.; BARINO, F. O.; CAMPOS, D.; DOS SANTOS, A. B. Enhanced aroma prediction in coffee fermentation through optical fiber sensor data fusion. *Sensors and Actuators A: Physical*, v. 369, p. 115223, 4 2024
- FARACO, R. L.; BARINO, F.; CAMPOS, D.; SAMPAIO, G.; HONóRIO, L.; MARCATO, A.; DOS SANTOS, A. B.; DOS SANTOS, C. C.; HAMAJI, F. Hydroelectric plant safety: Real-time monitoring utilizing fiber-optic sensors. *Sensors 2024, Vol. 24, Page 4601*, v. 24, p. 4601, 7 2024

2 THE LPG INTERROGATION PROBLEM

This chapter introduces the research problem addressed in this work. It describes the technology of the optical fiber grating sensors, the state-of-the-art LPG interrogation, and the use of sparse filter coupled to machine learning for LPG interrogation.

2.1 FIBER GRATING SENSORS

This work focuses on optical fiber sensors based on diffraction gratings. A fiber diffraction grating is formed by a modification in the properties of an optical fiber, typically periodic and affecting the refractive index of its core [43]. However, it can also involve changes in its geometry, such as wavegu ide tapering [44–46]. To perform such periodic alteration on the waveguide and thus to inscribe the fiber grating several techniques were described. Typical methodologies are the phase-mask UV radiation [47], femtosecond laser radiation [48, 49], CO2 laser radiation [50, 51], arc-induced [27, 52], and mechanical deformation [53–55].

This periodic waveguide modification, also known as modulation, causes a partial exchange of energy between propagating modes, a phenomenon described by mode coupling theory [43]. This exchange occurs when a phase-matching condition between such modes is met. Let β_1 and β_2 be the propagation constants of the modes and Λ the grating modulation period. The phase-matching condition for the m-th diffraction order occurs at a wavelength λ following the condition [56]:

$$\beta_2 = \beta_1 - m\frac{2\pi}{\Lambda} \tag{2.1}$$

Note that the phase-matching condition described in (2.1) depends on the grating modulation period. Therefore, it is natural to classify diffraction gratings based on their period, leading to two main subdivisions: Fiber Bragg Gratings (FBGs) for short-period gratings and Long Period Fiber Gratings (LPGs) for long-period gratings. The first has typical period of the sub-micrometer scale while the latter period is on the order of hundreds of micrometers.

Bragg gratings couple light between the fundamental core mode and a counter-propagating core mode. This coupling occurs at the phase-matching condition, causing the FBG to act as a selective mirror. As a result, the light transmitted by an FBG "loses" a specific color, and the reflected light is, ideally, monochromatic. However, coupling efficiency is not perfect, and a narrow notch-filter-like characteristic is observed in transmission with an equivalent passband in reflection, as illustrated in Figure 1. Let $\beta_1 = \beta_{01}$ and $\beta_2 = -\beta_{01}$, so the fundamental linearly polarized mode is coupled to its counter-propagating part. The propagation constant is related to the light's wavelength

Figure 1 – Schematic of the light-FBG interaction.

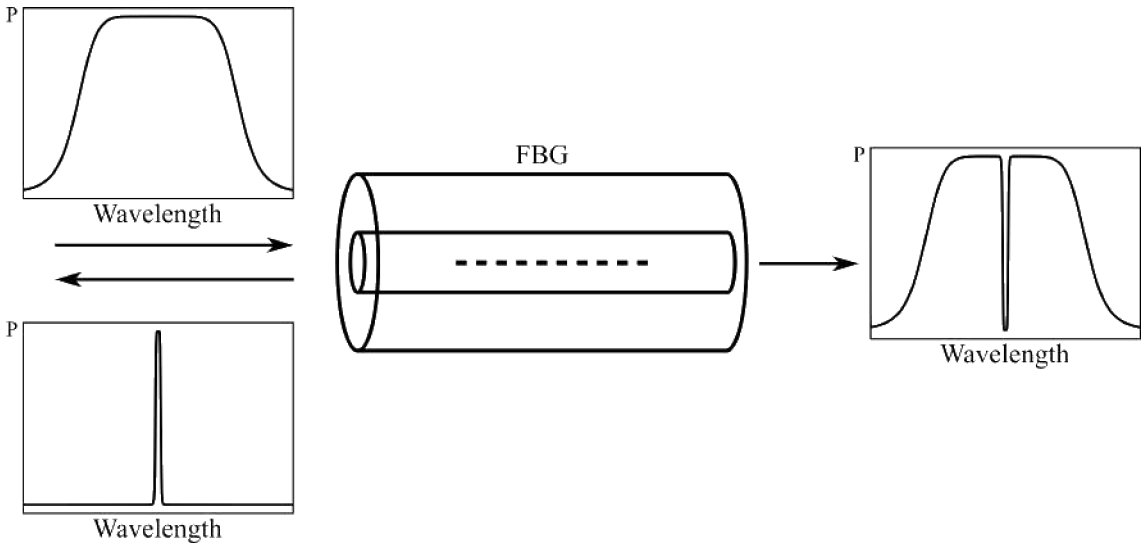

Source: Adapted from [57].

(λ) and mode's effective index (n_{eff}) through $\beta = (2\pi/\lambda)n_{eff}$. Hence, applying β_1 and β_2 to (2.1), one can calculate the wavelength which FBG reflects light (λ_{Bragg}) by:

$$\lambda_{bragg} = 2n_{eff}\Lambda \tag{2.2}$$

For a single mode optical fiber with 8.2/125 μm core/cladding diameter and 1.45213/1.44692 core/cladding RI, the FBG period to couple those modes at 1550 nm is 534 nm. An FBG can be used as strain and temperature sensor due to λ_{bragg} sensitivity to these parameters, causing the reflection center to shift. This sensitivity arises from changes in both n_{eff} and Λ. The former is influenced by elasto-optic and thermo-optic effects, while the latter is affected by fiber elongation and thermal expansion. The temperature and strain sensitivities can be expressed by $\partial\lambda_{res}/\partial T$ and $\partial\lambda_{res}/\partial\varepsilon$ [58]:

$$\frac{\partial\lambda_{bragg}}{\partial T} = \lambda_{bragg} \cdot (1 + \xi) \tag{2.3}$$

$$\frac{\partial\lambda_{bragg}}{\partial\varepsilon} = \lambda_{bragg} \cdot (1 + \rho_\alpha) \tag{2.4}$$

where ξ is the optical fiber's thermo-optic coefficient and ρ_α is the fiber's photo-elastic coefficient. The typical value for $\partial\lambda_{res}/\partial T$ is $\sim$13 pm/°C and for $\partial\lambda_{res}/\partial\varepsilon$ is $\sim$1.2 pm/$\mu\varepsilon$ [59].

Conversely, LPGs couple light from the LP_{01} to a higher order cladding mode, LP_{ab}. Since each cladding mode has a distinct propagation constant, the phase-matching

condition occurs multiple (m) times. Let β_m be the m-th order cladding mode propagation constant, the resonant wavelength for the m-th order coupling is given by:

$$\lambda_{res}^{m} = \left(n_{eff,co} - n_{eff,clad}^{m}\right)\Lambda \tag{2.5}$$

Considering the same optical fiber as above, a period of 571 μm is needed so that the fourth cladding mode is coupled at 1550 nm. So, the grating period for LPGs are roughly a thousand times bigger than the FBG counter part. Note, however, that this depends on the cladding order and the period for coupling to the sixth cladding mode at 1550 nm is 436 μm.

The mode coupled to the cladding undergoes severe attenuation, hence the resonance dip of LPGs. Indeed, light scatters at the cladding-surrounding interface and the light coupled to the cladding is lost. This effect causes the notch-like features in the LPG transmission spectra, as shown in Figure 2. This evanescent field is also responsible for the LPG's sensitivity to the surrounding refractive index (SRI). Note that the $n_{eff,clad}^{m}$ depends on the core, cladding and external refractive index. The temperature, strain, and SRI sensitivities can be expressed by $\partial\lambda_{res}/\partial T$, $\partial\lambda_{res}/\partial\varepsilon$, and $\partial\lambda_{res}/\partial n_{sur}$ [15]:

$$\frac{\partial\lambda_{res}}{\partial T} = \lambda_{res}\cdot\gamma_{res}\cdot(\alpha + \Gamma_{temp}) \tag{2.6}$$

$$\frac{\partial\lambda_{res}}{\partial\varepsilon} = \lambda_{res}\cdot\gamma_{res}\cdot(1 + \Gamma_{strain}) \tag{2.7}$$

$$\frac{\partial\lambda_{res}}{\partial n_{sur}} = \lambda_{res}\cdot\gamma_{res}\cdot\Gamma_{sur} \tag{2.8}$$

where α is the optical fiber's thermal expansion coefficient and γ_{res} is the material dispersion coefficient ate the coupled wavelength. Γ_{temp}, Γ_{strain}, and Γ_{sur}, on the other hand, describe

Figure 2 – Schematic of the light-LPG interaction.

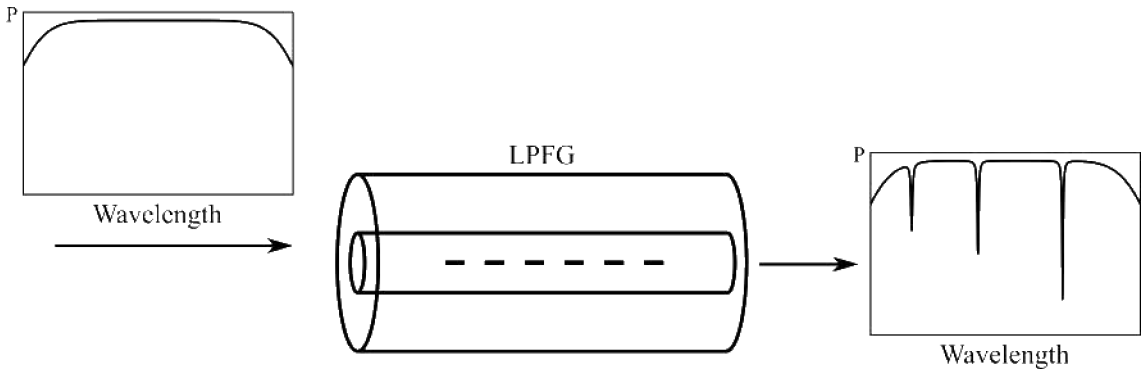

Source: Adapted from [57].

the dispersion regarding temperature, strain, and SRI, respectively. The numerical values for these sensitivities vary greatly regarding the mode order, for a fourth order mode operating at 1492.4 nm on a 550 μm device the typical values for $\partial\lambda_{res}/\partial T$, $\partial\lambda_{res}/\partial\varepsilon$, and $\partial\lambda_{res}/\partial n_{sur}$ are, respectively, -0.369 μ/°C, 0.57 pm/$\mu\varepsilon$, and -19 nm/RIU [15]. Recent works present superb sensitivity using special LPG design strategies, such as devices near the phase-matching turning point, an example is the 525 pm/$\mu\varepsilon$ strain sensor reported in [60] and 5602 nm/RIU SRI sensor reported in [61], illustrating how far the sensitivity of LPGs can be enhanced.

As discussed in the introductory chapter of this thesis, FBG sensing systems are readily available, and FBG sensors for temperature and strain can be easily purchased. Therefore, one advantage of LPGs lies in their SRI sensitivity. Although such characteristic could introduce errors due to cross-sensitivity in temperature and strain measurements, it is the basis of several novelties in optical sensing. One example is a label-free hemoglobin sensor utilizing a micro-tapered LPG coated with graphene oxide (GO) and polydopamine [62]. SRI sensitivity also underpins pH measurement using a phase-shifted LPG coated with GO and polyvinyl alcohol [63], label-free detection of pepsin also employing GO [64], *H. pylori* detection using a double resonance LPG and surface plasmon resonance sensors [65], and relative humidity measurement using a microtapered LPG coated with polyvinyl alcohol nanofibers [66]. Evidently, as proposed in [67], the application of a third layer on the fiber, a coating layer, expands the possibilities for measurands through the interaction between this layer and the measurand.

Being such a sensitive device, however, strain and temperature compensation is often need to effectively measure SRI in practical scenarios. This could be implemented through multi-sensor schemes, where other sensors such as FBGs [68–70] are used to measure temperature and strain, or using multiple resonant dips of the same LPG [71, 72].

2.2 STATE-OF-THE-ART LPG INTERROGATION

From equations 2.3, 2.4, 2.6, 2.7, and 2.8, one could note that the measurand obtained by grating-based optical fiber sensors is encoded as a wavelength. For example, for a LPG-based temperature sensor, the temperature would be monitored by the resonant wavelength. Hence, to retrieve the temperature and effectively use the device as sensor, there is a need to obtain λ_{res} through optical signal acquisition and processing. This acquisition might be a spectral measurement and the processing could be a dip finding algorithm (for LPG), to this procedure the optical instrumentation community has given the name of sensor interrogation. In the case of FBGs, the Bragg wavelength is extracted and to do so there is a wide range of industrial-grade devices readily available to perform the FBG interrogation [73–77]. Moreover, as FBGs operate in reflection, the optical cable does not need to return, and due to the narrow bandwidth, multiple sensors can be added

to this same cable by wavelength division multiplexing [59]. One could attribute these characteristics to the wide use of FBGs in the industry.

Unlike FBGs, the LPG spectrum is only obtained through transmission. Additionally, coupling efficiency is not as high; hence, the resonant dips are not as sharp. Indeed, the resonant dips of LPGs can span several nanometers, necessitating a wide spectral range for precise detection of their resonant wavelengths. As consequence, broadband spectral measurements are needed to accurately characterize and calibrate these sensors. As a result, current LPG interrogation methods often rely on bulky and costly equipment, typically designed to interpret only a single sensor. This increases system complexity and further hinders the cost-effectiveness of large-scale deployments. Furthermore, the broad spectral width of LPGs poses challenges for quasi-distributed sensing applications. Unlike FBGs, which can be readily multiplexed in the wavelength domain, allowing numerous sensing points along a single fiber to be monitored simultaneously using the same optoelectronics, the wider bandwidth of LPGs significantly limits the number of devices that can be effectively multiplexed [78, 79]. This limitation in multiplexing capacity directly impacts the scalability and economic viability of LPG-based sensor networks, especially in applications where a large number of sensing points are required.

To improve the cost-effectiveness of optical fiber sensors systems, some researchers have proposed the use of edge filtering techniques to extract portions of the optical spectrum and obtain the measurand. One method is based on the use of an arrayed waveguide grating (AWG) to filter the sensor spectrum and estimate the desired parameter. Due to the AWG's dense channel spacing, the FBG peak can be easily estimated by neighboring channels at the FBG vicinity [80], and the cost-effectiveness can be further improved by using a smart channel-selecting system assisted by deep learning [81]. As AWGs are high density filter banks, they can also be used to estimate the whole spectrum of an LPG [82].

Since FBGs are narrowband optical filters, they could also be used as edge filters for LPG demodulation [36, 83]. Similarly, the opposite is also possible and interesting to obtain fast FBG interrogation [84, 85], however due to LPG sensitivity, complex and careful LPG control might be needed [86]. For LPG demodulation, the classical approach for interrogating the LPG using FBGs is illustrated in Figure 3. Two FBGs are used at the sides of an LPG resonant dip, as the λ_{res} redshifts, the bluemost FBG increases power and the redmost FBG decreases power. Since the LPG spectrum slope is not linear, a differential approach to the filtered power is taken, where the relative difference over sum is used. A plot relating this differential power and the LPG position is shown in Figure 3(d).

However, the use of filters to measure the spectral characteristics of sensors requires a high degree of technical expertise, because a careful and well-designed experimental setup is necessary to obtain accurate and meaningful results. Once the filtered power

Figure 3 – Illustration on edge filtering of an LPG using two static FBG filters.

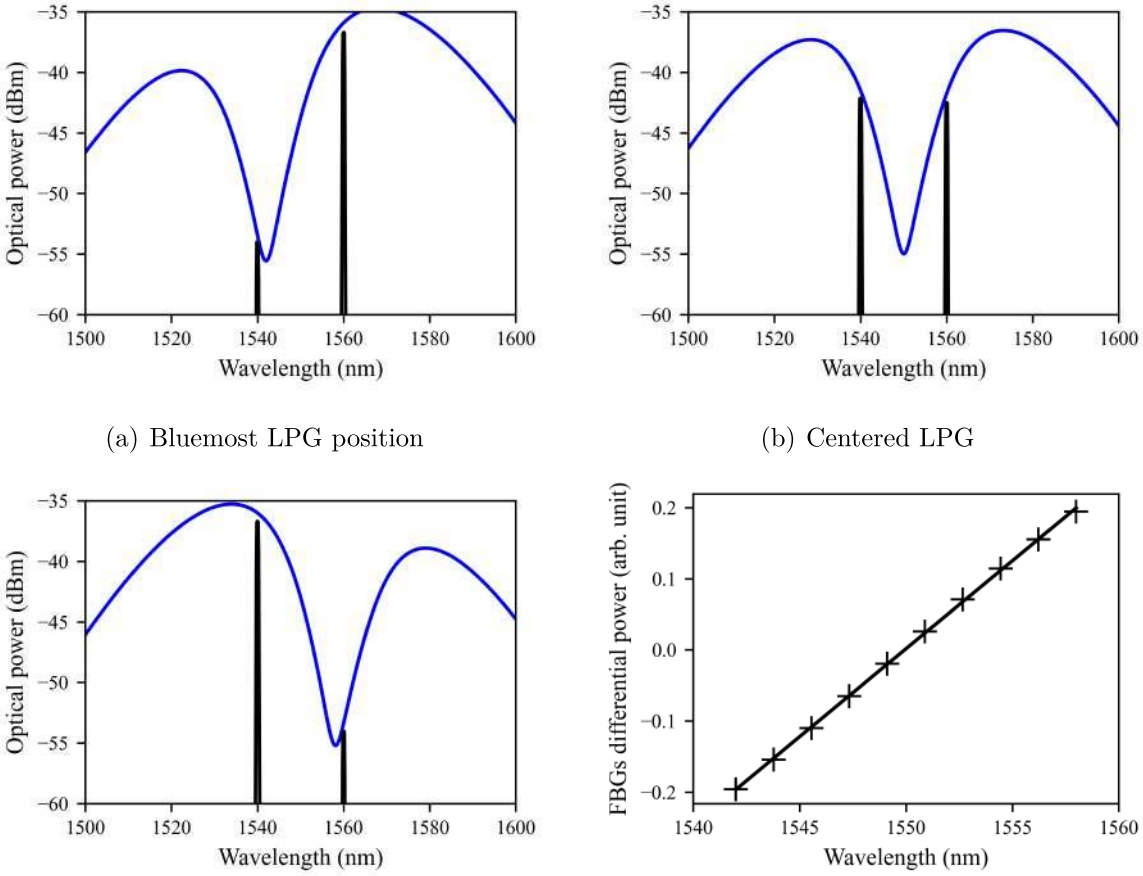

(a) Bluemost LPG position

(b) Centered LPG

(c) Redmost LPG position

(d) Calibration curve

Source: Plots elaborated by the author.

is highly dependent on LPG transmission characteristics, the results could be highly sensor-dependent, i.e., vary a lot for sensors with the same resonant wavelength, but different coupling efficiency, for example. Therefore, the interrogator is often tailored to a single sensor or to an extremely limited set of similar sensors.

A common problem occurs regarding the change of LPG sensor and is illustrated in Figure 4. The plot shown in Figure 4(a) describes three LPG spectra. The LPG0 and LPG1 are centred around the same resonant wavelength, but the coupling efficiency is quite different and the LPG1 has more prominent dip. The change from LPG0 to LPG1 using the same interrogating FBG pair would require a recalibration of the differential power curve, to properly retrieve the resonant wavelength, as illustrated in Figure 4(b). However, if the resonant wavelength of a new sensor is too close to one of the interrogating FBGs, the fitting curve loses linearity for the same dynamic range. This phenomenon can be seen when changing from LPG0 to LPG2.

Figure 4 – Illustration of the edge filtering limitations.

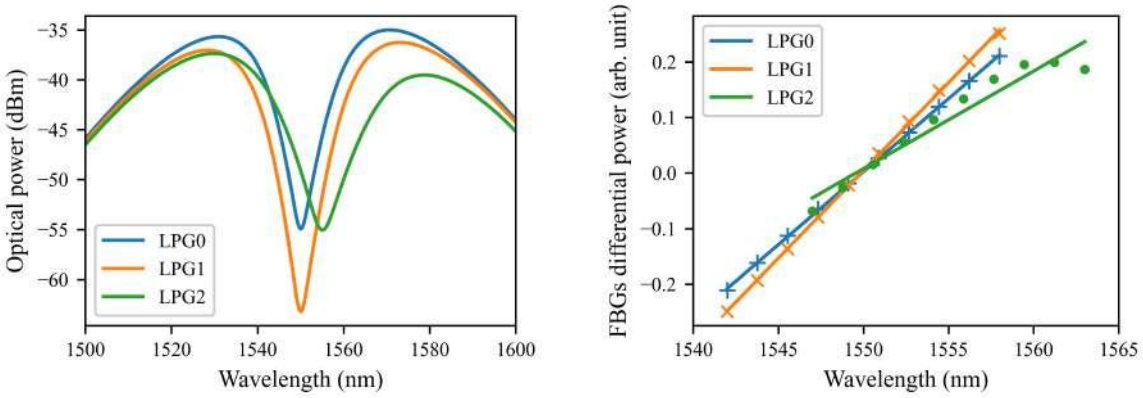

(a) Three LPG sensor spectra

(b) Respective calibration curves

Source: Plots elaborated by the author.

This illustrated how the edge filtering approach is highly sensor-dependent and have small dynamic range. I.e., the edge filtering interrogator must be optimized for a particular LPG sensor characteristic and it can only interrogate one LPG at a time.

This technique was called derivative spectroscopy and it was presented in [87], where the author proposed its use for LPG-based curvature sensing. In [88], a hybrid FBG-LPG configuration was employed to achieve intensity modulation for interrogating wavelength shifts in LPGs. This system demonstrated the ability to resolve strain and temperature variations, demonstrating the advantages of double-cladding LPGs in terms of stability and suitability for embedded applications. The interrogation system utilized the edge filtering effect of LPGs, where the resonant dip shifts in response to the measurand, modulating the intensity of transmitted light. This modulation, measured by an InGaAs photodetector, reflects the changes in the measurand.

The aforementioned interrogation approaches indeed exhibit a high degree of sensor dependence, with the LPG interrogators being intrinsically integrated into the sensing system alongside the sensors themselves. Recent research has focused on alternative LPG interrogation techniques, focusing on the interrogator development, transparent to any LPG sensor. In [89, 90], thermally modulated distributed feedback lasers were used to acquire power readings at different wavelengths, with curve-fitting then employed to extrapolate the LPG spectrum. This involved sweeping the central wavelength of three laser diodes and measuring the transmitted light intensity through the LPG. By fitting the acquired data to curve models, the sensor's transmission spectrum was reconstructed, enabling temperature and refractive index measurements. This system is affordable and suitable for real-time monitoring and data logging for in-field applications.

Similarly, in [91], an LPG interrogation system based on the temperature response of a multimode laser diode was developed. This system utilized the laser diode's spectral sweep to create a discrete attenuation spectrum, reconstructed using curve fitting. The system demonstrated high accuracy in interrogating LPGs within a 10 nm window, showing potential for slow-changing field applications.

Despite these advances, temperature modulation can be unreliable due to the difficulty in accurately characterizing the temperature-dependent transfer function and controlling the system. Additionally, the temperature change can be slow, resulting in slow spectrum measurements. This limits the application, as the LPG sensor must remain static throughout the temperature sweep. For instance, the temperature sweep in the multimode laser approach takes 50 minutes [91], and 15 minutes for the DFB method [89].

A more practical approach for full LPG spectrum measurement was proposed in [92], where a microelectromechanical system Fabry-Perot Interferometer (MEMS-FPI) is used to measure spectra at 100 Hz rate. The authors describe a low-cost wideband interrogation system for fiber optic sensors using a MEMS-FPI tunable filter. This low-cost, wideband interrogation system was validated by interrogating LPGs as temperature, refractive index, and relative humidity sensors. The system achieved accuracy comparable to commercial devices while being significantly more affordable and portable. Deconvolution techniques further enhanced measurement accuracy by mitigating the effect of the tunable filter's broadband response.

2.3 THE USE OF SPARSE FILTER AND MACHINE LEARNING

All these recent development in LPG interrogation present some interesting perspectives towards its in-field implementation, however, most of the works focus on full spectrum measurement or estimation. However it is not always necessary for LPG interrogation, hence simpler and more cost-effective solutions could be developed. Note that in most cases, only the resonant wavelength is required, because LPG sensors are calibrated based on the resonant wavelength shift. Edge filtering techniques focus on this premise and, in this work, a methodology to extract only the resonant wavelength of any given LPG is proposed. The proposal uses a sparse filter bank and a machine learning model to process the filtered information and retrieve the LPG position. The combination of a filter bank and machine learning aims to solve the challenges in edge filtering.

Machine learning has undoubtedly experienced significant growth in applications over the past decade. From OpenAI's first report on GPT-1 in 2018 [93] to the public release of ChatGPT in late 2022, large language models (LLMs) have found use in diverse fields like medicine [94] and chemistry [95]. The potential of artificial intelligence (AI) models to improve various fields seems promising, with results often appearing remarkable. Complex models can be used for early disease diagnosis [96, 97], enhancing reliability and

risk assessment [98], and even attempting stock forecasting [99, 100].

Nevertheless, caution is warranted when dealing with such abstract forms of data processing. Deep learning and other complex AI models are often considered "black boxes", meaning their internal workings are not transparent. Note that while they provide useful information, the reasoning behind their conclusions remains hidden. This lack of transparency can lead to serious societal issues impacting health, freedom, racial bias, and safety due to the potential for incorrect predictions based on flawed logic [101]. Consequently, the excessive use of AI for evaluation and knowledge extraction can be dangerous, fostering illusions of understanding and scientific monocultures [102].

Therefore, careful consideration is crucial when employing machine learning models, particularly in the instrumentation field. The measurements systems are the interface for knowledge acquisition and experimentation, so the results should be reliable and well characterized. So, with proper care, machine learning can be applied to measuring instruments, one solution is to develop application-specific models and rigorously test them. In this context, uncertainty quantification and expression are vital, adhering to best practices in instrumentation and measurement.

In this work, machine learning models were employed for LPG sensor interpretation, specifically as curve-fitting tools, tailored to this application. The proposed methodology combines a machine learning model and a sparse optical filter array to address challenges encountered in dual FBG edge filtering, using the hardware illustrated in Figure 5. Hence, the basis of the hardware needed is the optical filters and a photodetection unit per filter. Considering the use of FBG filters, a filtering channel would be made of: an FBG, optical circulator, photodiode, and transimpedance amplifier.

Figure 5 – Hardware for the FBG sparse filter used in the LPG interrogation system.

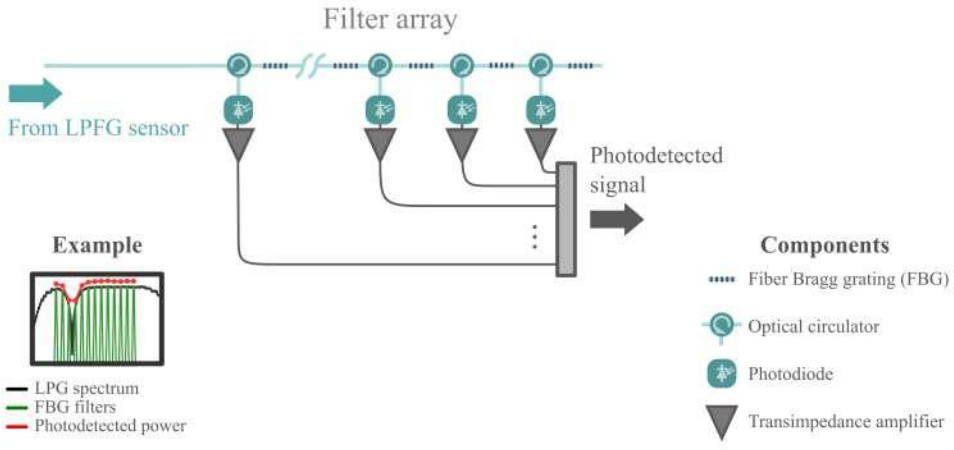

Source: Figure elaborated by the author.

The hardware design involves strategically spacing an FBG filter array to ensure that at least two FBGs fall within the LPG resonant dip (one blueshifted and another redshifted regarding the LPG), to solve dynamic range issues of edge filtering techniques. Additionally, the machine learning model serves as an adaptive and LPG-independent calibration model, effectively solving the recalibration issues. This approach is anticipated to be cost-effective due to its potential for extension to a full-sensor scheme, where the filters themselves function as sensors. This concept is explored in detail in Chapter 6.

3 ANN ESTIMATION OF THE RESONANT WAVELENGTH

In this chapter the use of a neural network to interrogate a long-period fiber grating sensor is demonstrated. The proposed interrogator uses an FBG filter bank to acquire spectral features of the LPG and feed a neural network with them, to provide a resonant wavelength estimation. In the next sections an introductory overview on neural networks is presented, followed by the methodology for developing the interrogator, and the results obtained.

3.1 INTRODUCTION TO NEURAL NETWORKS

Neural networks are a category of machine learning algorithms roughly inspired by animals' neural system. One of the first and most important contribution to the develpment of artificial neural networks (ANNs) was the McCulloch and Pitts neuron in 1943 [103]. At this time the researchers were trying to understand the complex patterns generated by the brain's basic unit cells and they proposed a simplified model for these cells. The next major development was the perceptron, introduced in 1958 [104], a perceptron is basically a McCulloch-Pitts neuron with weighted inputs. Hence, the perceptron is a neuron-inspired linear model that can "learn" through weight optimization.

The percepton, however, is limited to a set of linear classification tasks. To expand its complexity, several of this neuron units can be added, forming a proper network. By stacking layered groups of perceptrons, one obtain the multilayer perceptron (MLP). Such topology is also called fully-conected network, because there is a connection between each adjacent neuron, it is one of the most popular form of neural network and is part of several more complex models. The popularity and importance of the MLP is due to its ability to approximate any function with a finite number of discontinuities with only one abstraction layer [105–107].

As the name suggest, the MLP is organized in layers, the first is the input data and the last is the output layer. All layers in between are called hidden layers, or abstraction layers. Each layer is formed by a set of nodes and all nodes of a layer are connected to the nodes of the previous layer. The nodes of hidden and output layers are artificial neurons. Figure 6, shows the structure of a three-layered MLP, this MLP has N inputs, H hidden neurons and one output. It is the typical topology for function approximation, i.e., regression.

Each connection between two nodes has a weight associated with it. The processing inside a neuron starts by the dot product between all of its inputs and their weights, plus a bias. This result is then passed through a function before connecting to the next layer. Hence, for the MLP illustrated in Figure 6, the i-th hidden neuron's output is given by:

$$h_i = f\left(b_i + \sum_{k=0}^{N-1} x_k w_{i,k}\right) \tag{3.1}$$

where b_i is the i-th neuron's bias, $w_{i,k}$ is the weight connecting the k-th input to this neuron and $f(\cdot)$ the neuron activation function. Given the H neurons outputs, one can calculate the neural network output by:

$$y = b_y + \sum_{i=0}^{H-1} h_i w_{y,i} \tag{3.2}$$

where b_y is the output bias and $w_{y,i}$ is the weight between each hidden neuron and the output neuron.

Note that relationship between the inputs and output depends on the weights values. Hence, the output y shown in (3.2) is only meaningful to a given task, if the weights were properly set. The weight adjustment process is called training, or fitting. During the training the model is adjusted using optimization algorithms and known data.

This type of model optimization is called supervised training and it is usually made by a form of back-propagation algorithm [108]. First the weights are randomly initiated, then the known inputs are propagated through the network, obtaining an estimation. The estimation error is then calculated and propagated backwards, updating the weights so that the final error is minimized.

The premise of using neural networks is simple, one needs to acquire data that is well representative of the model's use case and apply this data to model development and evaluation. To do so, this dataset needs to be split at least into three subgroups:

Figure 6 – Schematic of a three-layered MLP

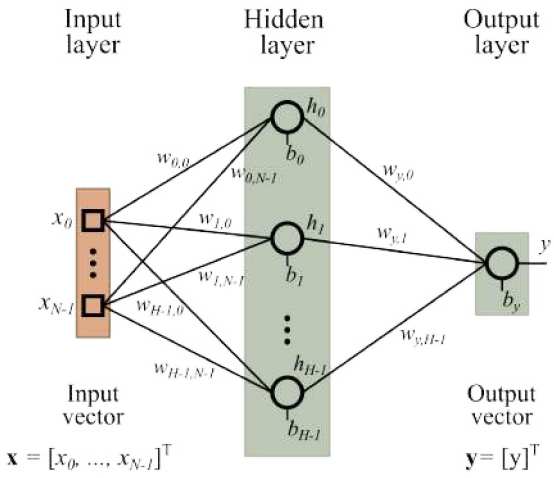

Source: Figure elaborated by the author.

training, validation, and testing. Each group should be used in the step relative to its name. The training group is used to adjust the neural network weights. The validation is used to validate the topology and perform early stopping during training, finally, the testing group is used to evaluate the model error and uncertainty. Early stopping is a training strategy used to improve model's ability to deal with data similar to the training data, but unknown. It is used to avoid overfitting and smooth the model's output, reducing its variance [109–111].

In most cases, training data is used to develop some feature selection and feature engineering techniques, so the raw collected data can be preprocessed before the input layer. Feature selection involves identifying and selecting the most relevant features that contribute significantly to the target variable, reducing noise and dimensionality, thus improving model efficiency and generalization. Feature engineering, on the other hand, focuses on creating new features or transforming existing ones to enhance their predictive power, often through domain knowledge or statistical techniques. This can involve scaling, normalization, encoding categorical variables, or deriving new features from interactions or combinations of existing ones. Preprocessing steps, such as handling missing values, outliers, and ensuring data consistency, are essential to prepare the data for effective training of the neural network. In the context of MLPs, these techniques are vital due to their sensitivity to input data characteristics. Careful feature selection, engineering, and preprocessing can significantly enhance the model's ability to learn meaningful patterns, leading to improved accuracy and robustness in predictions.

3.2 METHODS FOR ANN DESIGN AND CHARACTERIZATION

This section presents the methodology used to develop the interrogation method based on a multilayer perceptron (MLP) neural network. The dataset, feature engineering, and MLP design are, respectively, discussed.

3.2.1 The dataset

Figure 5 illustrates the system used to acquire power readings from LPG spectra. To design and evaluate the interrogator, 83 different arc-induced LPGs were considered, with different transmission spectrum features and characteristics, such as attenuation, full width at half maximum (FWHM), resonant wavelength, and different attenuation dip asymmetries. The LPGs were manufactured using an in-house modified Fiber Fox Mini3s fusion splicer, coupled to a Thorlabs MTS50/M-Z8 linear translation stage and a KDC101 controller, this manufacturing setup can be seen in Figure 7. To increase the spectra count, each LPG was strained and heated, obtained a total of 528 transmission spectra. The LPG spectra were recorded using an Anritsu MS9740B.

Figure 7 – Setup for arc-induced LPG manufacturing.

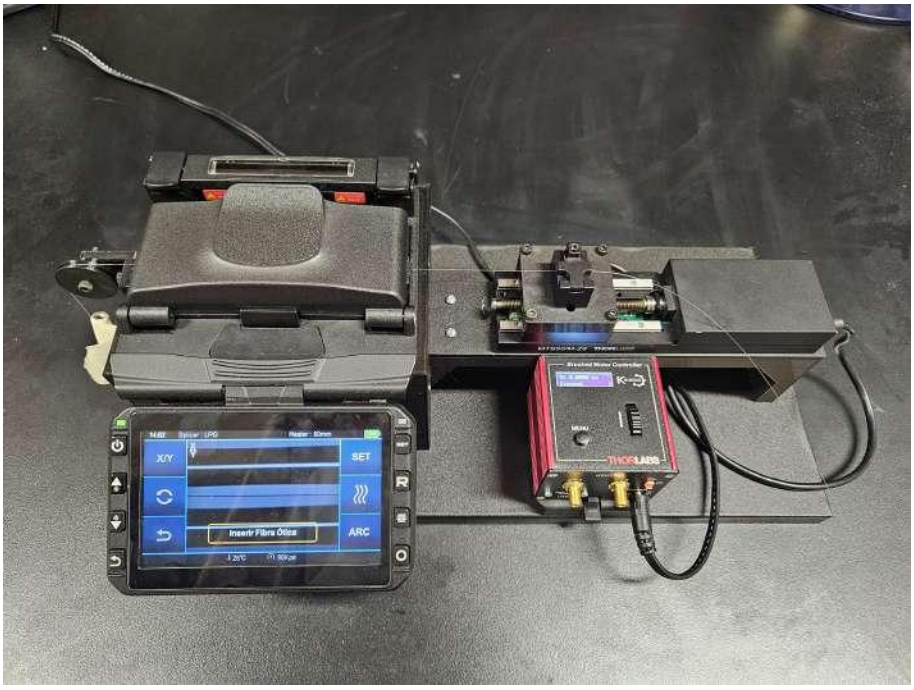

Source: Photography taken by the author.

Some LPG transmission spectra can be seen in Figure 8. To visualize the whole dataset, the resonant wavelength, FWHM, and attenuation intensity for these 528 spectra are summarized in Figure 9, where the LPG period (Λ) is represented by different symbols. Note that for each grating period several LPGs were manufactured using different electric arc intensities, which are represented by the different colors. Hence, one can see the great variability presented by the spectra used that could provide the trained ANN with good

Figure 8 – Eight randomly chosen LPGs transmissivity spectra from the database.

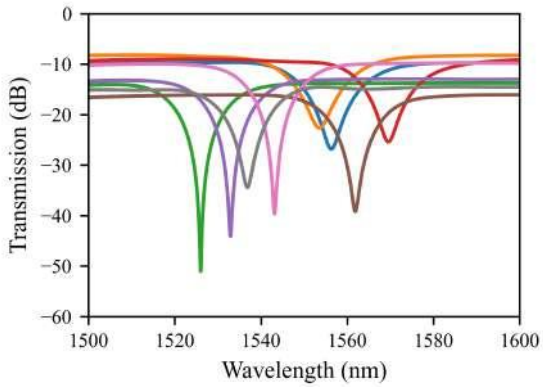

Source: Adapted from [35].

Figure 9 – Spectral features of spectra considered.

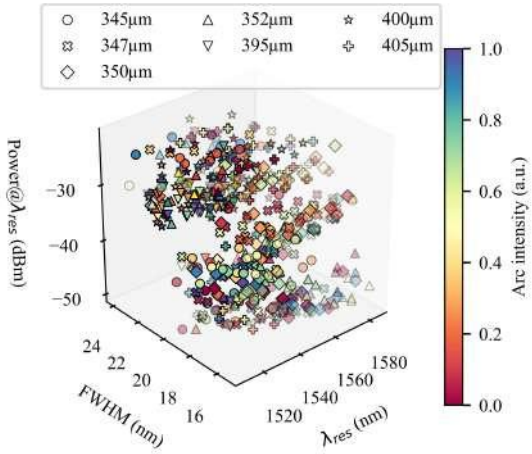

Source: [35] © 2020 IEEE.

generalization.

The dataset was randomly partitioned into three subsets: training (60%), testing (20%), and validation (20%). The training set was used to train MLP models under various scenarios (different hidden layer configurations), while the validation set was used to evaluate these trained models and select the best one as the final MLP for the LPG interrogator. The testing set was reserved for evaluating the performance of the finalized interrogator.

3.2.2 Design of FBG filters

To design the interrogator's neural network, feature selection is primarily associated with designing the FBG filter bank, as the power readings from these filters serve as inputs to the MLP. Therefore, the number of FBGs and their spacing in the wavelength domain were central considerations in this design process. By analyzing the spectral characteristics using the test and validation data, and reserving the test data solely for evaluating the final design. The main statistics considered for FGB array design were the minimum and maximum resonant wavelengths, as well as the mean and minimum full width at half maximum (FWHM).

While the resonant wavelength information was used to establish the maximum and minimum detectable λ_{res}, the FWHM provided insights into appropriate FBG spacing. The correct density of the FBG array is crucial for accurate resonant wavelength detection. By selecting an appropriate FBG spacing, one could ensure that at least one filter resides within the LPG's dip region. In the worst-case scenario, where two FBGs are positioned at the -3 dB points of the LPG transmission spectrum, a third filter placed at the mean of these two would fall within the LPG rejection band, with a spacing of half the FWHM.

If the LPG's resonant wavelength shifts, two FBGs would then be within the rejection band. Moreover, increasing the number of FBGs within this range would yield more information about the LPG rejection band, potentially leading to improved resonant wavelength estimation.

3.2.3 MLP design

Following the filter array design, the optical power for each spectrum was obtained using the designed FBG array and normalized to the [0,1] interval. This yielded input/output pairs for subsequent MLP development. The size of the MLP hidden layer was determined through an iterative trial-and-error process, exploring various configurations. In all cases, the Rectified Linear Unit (ReLU) activation function was employed for the hidden layer neurons, and weights were optimized using the Limited-memory Broyden–Fletcher–Goldfarb–Shanno (LBFGS) method to minimize the mean squared error (MSE), this solver was chosen due to its better performance on sample-limited datasets. Early stopping with a patience of 12 iterations was implemented to prevent over-fitting. To accommodate this early stopping mechanism, the maximum iteration parameter was set to 10,000. The entire process was executed in Python using the scikit-learn library v1.2.2 [112], with all remaining parameters not explicitly mentioned maintained at their default library values.

The model selection process involved training and evaluating the same model topology 20 times, varying the number of hidden layer neurons from 3 to 8. The selection criterion was to choose the smallest network that achieved a reasonable validation MSE, while also taking into account the variance across the 20 trials. After selecting the model, its performance was assessed using the test set data. The metrics considered were by the MSE in λ_{res} estimation, the mean absolute error (MAE), and residual analysis. Furthermore, interrogator's output was visualized by a curve relating the observed λ_{res} to the estimated λ_{res}.

3.3 RESULTS OF ANN-BASED INTERROGATOR

LPG spectra were recorded using an Anritsu MS9740B OSA and the spectral analysis revealed that the resonant wavelengths available within the dataset ranged from 1510 nm to 1585 nm, with a mean FWHM of 18.64 nm and a minimum value of 15.30 nm. Based on this, an FBG array spanning 1500 nm to 1596 nm, with 8 nm spacing between filters, was evaluated. This array encompassed all resonant wavelengths in the dataset and ensured at least one FBG filter overlapped with the LPG dip for most of the sensors used.

The FBG array was assessed by examining the relationship between the LPG resonant wavelength and the filtered data for each FBG. LPG resonant wavelengths were divided into 20 equally spaced regions, akin to histogram bins. For each region, the mean

Figure 10 – FBG filtered power as a function of the LPG sensor and it's own position.

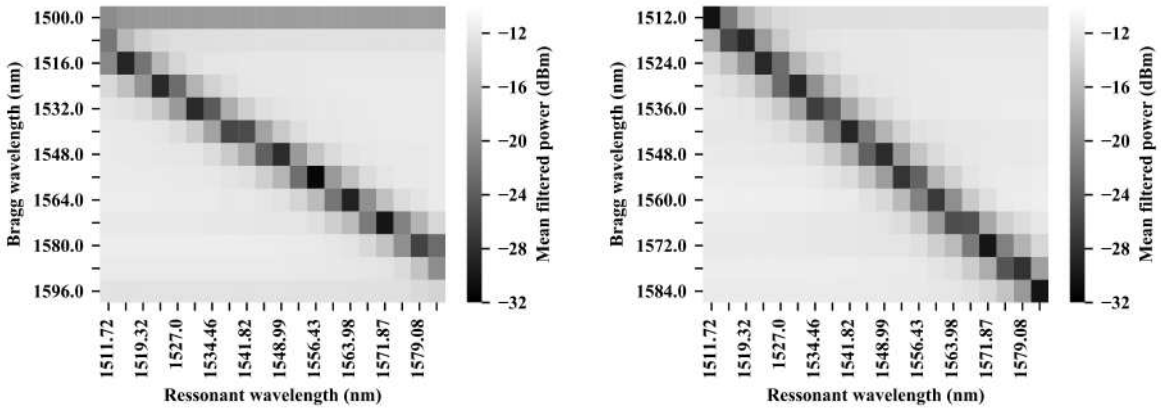

(a) 1500 nm – 1596 nm FBG array

(b) 1512 nm – 1584 nm FBG array

Source: [35] © 2020 IEEE.

filtered power of each FBG was calculated and plotted in a color map (Figure 10), with the x-axis representing the LPG resonant wavelength section and the y-axis representing the Bragg wavelength of each FBG. Color intensity denoted the mean filtered power by the FBG at each resonant wavelength section.

Figure 10(a) reveals that for the 1500 nm – 1596 nm array, the optical power filtered by FBGs at 1500 nm, 1508 nm, 1588 nm, and 1596 nm exhibited minimal variation with respect to λ_{res}. These FBGs captured little to no information about the LPG resonant wavelength and were thus deemed redundant or requiring adjustment. Consequently, the FBG array was refined to 1512 nm – 1584 nm, with a reduced spacing of 6 nm. This narrower window aimed to maximize power variation within the FBG array relative to the LPG resonant wavelength.

The refined array, shown in Figure 10(b), demonstrates a more even distribution of filtered power across the resonant wavelength, evident in the distinct diagonal formed by lower mean filtered power values. This diagonal suggests that each FBG contributed equally to the extraction of LPG resonant wavelength information. Additionally, the darker and thicker diagonal in Figure 10(b) indicates that more FBGs are positioned within the LPG dips, resulting in increased spectral information retrieval compared to the initial array.

The 20 tests conducted for each hidden layer configuration are summarized in the boxplot of Figure 11. It was observed that five neurons were sufficient for estimating the LPG resonant wavelength. The mean MSE across the 20 tests remained relatively consistent for all tested configurations, but the maximum and minimum MSE values fluctuated significantly for hidden layer sizes of 3 and 4 neurons. Therefore, the smallest

Figure 11 – Validation mean squared error as a function of hidden layer size (number of neurons).

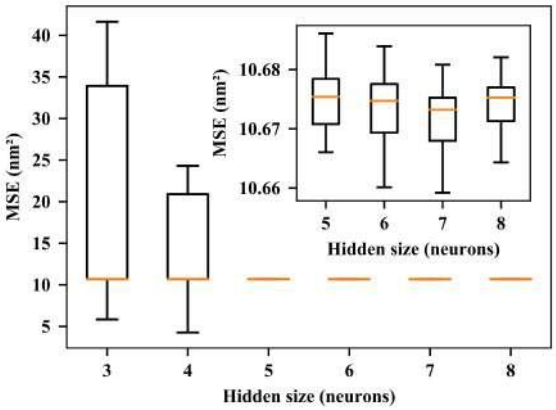

Source: [35] © 2020 IEEE.

hidden layer without such high fluctuation was chosen, resulting in a final MLP with five neurons in its hidden layer.

Using the test data, the interrogator MSE was estimated to be 1.98 nm², and the MAE was 1.00 nm. A visual representation of the proposed interrogator's performance is provided in Figure 12. The ideal interrogator is depicted by the solid black line, while the red dots represent the results obtained with the proposed technique. The close alignment of the red dots with the solid line indicates a reasonable approximation of λ_{res}. This is further supported by an R^2 value of 0.993, suggesting that the MLP model effectively explains the observed data.

Figure 12 – Observed vs estimated resonant wavelength.

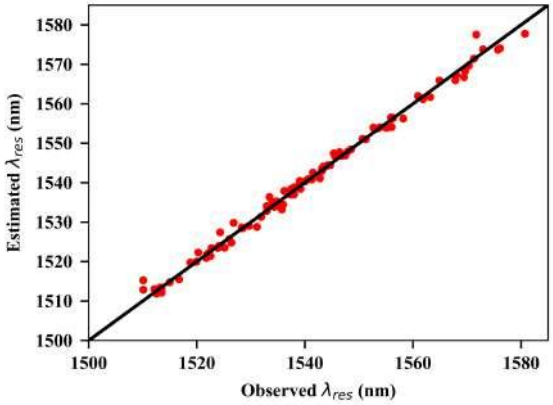

Source: [35] © 2020 IEEE.

Figure 13 – Residuals histogram (left y-axis) and its parametric fit to a normal distribution (right y-axis).

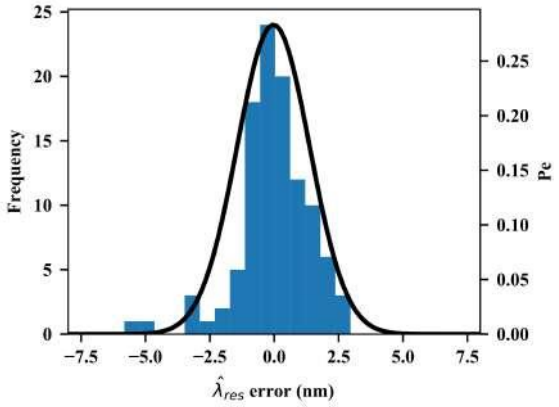

Source: [35] © 2020 IEEE.

The residuals, representing the differences between the red data points and the black line, are illustrated in Figure 13. A Gaussian distribution was fitted to the residuals histogram to derive the error probability function (Pe), shown on the right y-axis of Figure 13.

The mean value for this normal distribution is $\mu = 0.0330$ nm, and its standard deviation is $\sigma = 1.41$ nm. Consequently, the proposed interrogator can estimate an LPG resonant wavelength with a -33.0 pm bias and 2.82 nm uncertainty, considering a 95% confidence interval.

In contrast, previous work [89] utilized three thermally modulated fiber-coupled laser diodes to scan and reconstruct the LPG spectrum using fitting functions, achieving a resonant wavelength estimation within 1.12 nm error for the 1530 nm – 1570 nm region. However, the approximation function required refitting for each LPG used.

The current study demonstrates that incorporating machine learning into a similar but simpler setup enhances interrogator generalization. The proposed interrogator achieved a 1.00 nm MAE without LPG-dependent refitting or filter modulation. Furthermore, it yielded an error distribution with $\mu = 0.0330$ nm nm and $\sigma = 1.41$ nm for 106 spectra from different LPGs across the 1510 nm – 1585 nm range, nearly doubling the dynamic range reported in [89], which employed a far more complex setup.

3.4 CONSIDERATIONS REGARDING THE ANN ESTIMATION

This chapter showed the possible use of a static FBG array and an artificial neural network (ANN) to estimate the resonant wavelength of LPGs, thus performing the LPG demodulation using a sparse filter bank. The proposed ANN-based interrogator exhibited

promising performance, achieving a mean absolute error (MAE) of 1.00 nm and a root mean squared error (RMSE) of 1.41 nm. The system's ability to accurately estimate the resonant wavelength across a range of LPGs highlights its potential as a cost-effective and efficient interrogation method.

However, the current system presents some limitations. Utilizing an FBG array as a filtering element can be challenging, as FBGs are inherently sensitive to temperature and vibration the filters tend to fluctuate. These fluctuations may cause power variations that deviate from the intended power-to-wavelength mapping used during training. Additionally, the relevance of individual FBGs for LPG position estimation varies upon sensor location; those filters closer to the LPG provide more positional information, as the filters are more affected by the sensor. Consequently, optoelectronic noise affects all inputs equally, potentially hindering the interrogator's accuracy. To enhance noise suppression, the machine learning model could be improved by incorporating an intelligent input-selection mechanism that prioritizes relevant FBGs for each given case and minimizes the impact of noise on less informative inputs.

4 FIS ESTIMATION OF THE RESONANT WAVELENGTH

In this chapter, the previously reported interrogator is further improved. An improvement on the FBG-filtered LPG features preprocessing is presented and a fuzzy approach to the resonant wavelength estimation is reported, where only the FBGs close to the LPG resonance is considered. In the next sections an introductory overview on fuzzy inference systems is presented, followed by the methodology for developing and characterizing the fuzzy systems, and the results obtained.

4.1 INTRODUCTION TO THE FUZZY INFERENCE SYSTEM

A Fuzzy Inference System (FIS) is a system that utilizes fuzzy variables and logic, coupled to a set of "IF-THEN" rules, to make predictions based on imprecise or uncertain data. It is a powerful method, with wide application, like disease diagnosis [113], electrical engineering [114], and agriculture [115], for example.

Beyond the robustness of the fuzzy sets, the FIS have the advantage of easy integration of multiple inputs, interpretability of the system, easy transfer learning from an expert to the system, and easy maintenance. Some applications in the field of instrumentation are the failure analysis [116], energy management in wireless sensor networks [117], soft sensing [118, 119], and sensor fusion [120, 121]. In the field of optical fiber sensing, fuzzy logic has already been used to estimate impact localization using FBGs [122], to monitor mechanical fingers using FBGs [123], to reconstruct dynamic deformations [124], and to process LPG data and estimate axial stress [125].

The fuzzy logic is an extension of boolean logic that allows for partial truths, i.e., a statement can range between fully false (0) and completely true (1). This is the principle that enables the high level of uncertainty abstraction. There are four key concepts in fuzzy logic and fuzzy systems: the fuzzy sets, linguistic variables, fuzzy rules , and fuzzy inference.

The fuzzy sets are an extension of the classical notion of a set, introduced by Zadeh in 1965 [126]. Let X be a reference space of points where a generic element is denoted by x. A fuzzy set $A \in X$ can be described by a pair (A, f_A), where $f_A : A \rightarrow [0, 1]$ is a membership function. The result $f_A(x)$ represents how much x belongs to A, i.e., a grade of membership.

As in all mathematical description, variables can take values a and describe quantities. In fuzzy logic the concept of variables is expanded to linguistic variables, as no particular value is taken to a variable, but a degree of membership to one (or more) fuzzy sets. The linguistic variable "Temperature", for example, can have a degree of membership to the fuzzy sets "hot", "warm", and/or "cold".

The fuzzy rules are instructions expressed in the form of "IF-THEN" statements, where the antecedent (IF part) and the consequent (THEN part) are used to analyse input relationships between input variables and their membership grade to fuzzy sets and map to an output set. For example, an air-conditioning system might have a rule such as "IF Temperature is HOT and Humidity is HIGH, THEN power is HIGH", so the system is at high power as the membership grade of Temperature and Humidity to the fuzzy sets HIGH.

Hence, the set of "IF-THEN" statements is called rule base and represents the knowledge about the problem, i.e., the relationship between input-output. Indeed, the fuzzy inference system use this rule base to map the input to a desired output. This process is called fuzzy inference and the main inference engines are the Mamdani [127] and Takagi-Sugeno [128]. Note that the inference systems operate in fuzzy logic and values, so the first step in a fuzzy system is to fuzzify the input variable of classic numeric value (called crispy value) using the input membership function. Similarly, the last step is to defuzzify the activated output sets to a crispy value. Consequently, the membership functions should be carefully determined so the inference system better express the desired application scenario.

Moreover, to perform the inference, one should compare and operate fuzzy sets. The generalization of the logical conjunction and disjunction operations in fuzzy logic are called triangular norms and conorms, t-norms and t-conorms for simplicity. A t-norm is an operation between grade of memberships that satisfies the commutativity, associativity, and monotonicity condition with a neural element of one. The minimum t-norm and product t-norm are popular examples. A t-conorm, on the other hand, have a neutral element of zero. Exemples include the maximum t-conorm and probabilistic sum.

Figure 14 shows an example of a fuzzy system with five inputs, so five linguistic variables $(X_1, X_2, \ldots X_5)$, each one with three possible sets (blue, green, and red curves indicating the sets membership functions).

The rule base must contain rules like "IF Variable X_1 is green AND Variable X_2 is

Figure 14 – Schematic of a fuzzy inference system.

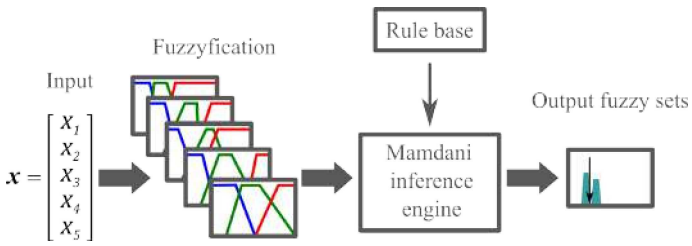

Source: [37] © 2022 IEEE.

red, THEN output is Y_5", for example. I.e., the rules relate the inputs and their interaction with an output set. Most of the cases the rule base activates several output sets to some degree. This results in a conjunction of fuzzy sets that should be defuzzyfied to obtain the crispy output.

4.2 METHODS FOR FIS DESIGN AND CHARACTERIZATION

This section presents the methodology used to develop the interrogation method based on a fuzzy inference system. The data preprocessing, FIS design, and evaluation metrics are, respectively, discussed.

4.2.1 Dataset and preprocessing

The interrogator hardware and dataset were the same as described in Chapter 3 because optimal spectral placement of FBGs were already obtained and the dataset had great representation of LPG's spectral variability. Therefore, the optical setup is exactly the same, the arc-induced LPGs and the same FBGs, as well as the 60%/20%/20% train/test/validation split. Consequently, the same 13 power readings were considered as input of the FIS. The FBG array power reading, however, were preprocessed in a more sophisticated manner. First assume, with no loss of generality, that the optical source used to illuminate the LPG sensor is known and that the interrogator could be used to acquire its power readings. This is a reasonable assumption because acquiring the power readings for the source could be performed by bypassing the LPG sensor, i.e., connecting the optical source directly to the interrogator.

Let $\mathbf{x}_{LPG}$ and $\mathbf{x}_{source}$ be vectors of power readings for an LPG sensor and for the optical source used to illuminate this LPG, respectively. To reduce the source interference on the power readings $\mathbf{x}_s = \mathbf{x}_{source} - \mathbf{x}_{LPG}$ was calculated for compensation. Nevertheless, instead of subtracting the source from the LPG, the LPG was subtracted from the source. Therefore, instead of a power dip around the resonant wavelength, one should see a power peak. Finally, $\mathbf{x}_s$ was scaled by its sum. Hence, the full preprocessing of $\mathbf{x}_{LPG}$ is given by:

$$\mathbf{x} = \frac{\mathbf{x}_{source} - \mathbf{x}_{LPG}}{\sum_{i=1}^{13} x_{i,source} - x_{i,LPG}} \tag{4.1}$$

This preprocessing is illustrated in Figure 15. Before the preprocessing, $\mathbf{x}_{LPG}$ represents the optical power of the LPG spectrum at the position of each FBG filter. After the procedure, $\mathbf{x}$ is obtained, which represents how close the LPG resonant wavelength is to each FBG filter, and it was called input strength. For example, if $x_i = 1$, λ_{res} would have the same position as $\lambda_{Bragg,i}$. Similarly, if $x_i = x_{i+1} = 0.5$, λ_{res} would be positioned at the mean between $\lambda_{Bragg,i}$ and $\lambda_{Bragg,i+1}$. Therefore, $\mathbf{x}$ provides a meaningful information about the LPG position, and more easily interpretable than the raw $\mathbf{x}_{LPG}$ data.

Figure 15 – Data preprocessing.

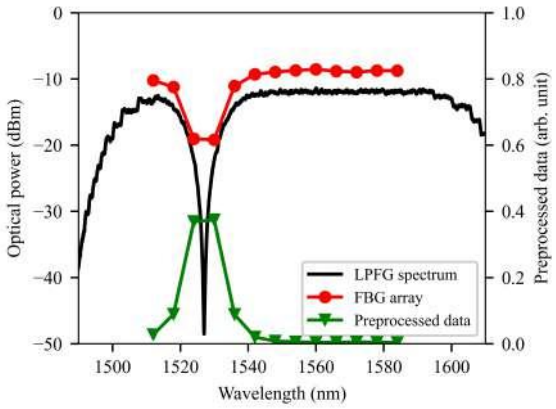

Source: [37] © 2022 IEEE.

However, these examples are unlikely to happen due to the relationship between LPG FWHM and FBGs spacing. Practical values, on the other hand, should appear as a superposition of these two examples. Note in Figure 15 that $x_3 \approx x_4 < 0.5$ but $x_2 \approx x_5$, with λ_{res} roughly between $\lambda_{Bragg,3}$ and $\lambda_{Bragg,4}$. Therefore, for the other case, if $\lambda_{res} \approx \lambda_{Bragg,i}$, one should see a high value for x_i and a smaller $x_{i-1} \approx x_{i+1}$.

A priori, this enhanced interpretability should lead to improved resonant wavelength demodulation. With knowledge of the FBGs' positions, represented by the vector containing each Bragg wavelength, $\lambda_{\mathbf{FBG}}$, a direct estimation of the LPG position is possible, as long as the FBG spacing remains constant and linear. The dot product $\mathbf{x} \cdot \lambda_{\mathbf{FBG}}$ functions as a weighted mean, which utilizes the fundamental principle of input strength to estimate the resonant wavelength. This concept will be presented later as a baseline model.

4.2.2 Design of the FIS system

The preprocessed data calculated by (4.1) serves as the input to the Fuzzy Inference System (FIS), with the values undergoing fuzzification. The proposed FIS had 13 inputs, corresponding to 13 linguistic variables X_i where $i \in \{1, 2, \ldots 13\}$. Each variable represents the input strength at each FBG, and all share the same fuzzy sets: FAR (F), NEAR (N), and CENTERED (C). These fuzzy sets indicate whether the LPG resonant wavelength is far from (F), near (N), or centered at (C) the i-th input filter. The output sets represent the LPG position and are positioned at each FBG location and between each filter element, resulting in 25 possible sets, denoted as $\mathbf{\Lambda}_k$ where $k \in \{0, 1, \ldots, 24\}$.

The membership functions for the input sets were described using a double-variance modified Gaussian function. Unlike the traditional Gaussian function, this approach employs a variance σ_1^2 for values below the mean μ, and σ_2^2 for values above the mean,

allowing for asymmetric input membership functions. In contrast, the output sets utilized trapezoidal membership functions, centered from 1512 nm to 1584 nm with 3 nm spacing. The top and base widths of each trapezium were 1.25 nm and 5.00 nm, respectively. For defuzzification of the output, a simple weighted average method was applied.

The input membership functions were designed by training data inspection: the relationship between input strength at each filter Bragg wavelength and LPG position. This analysis was facilitated by the heatmap presented in Figure 16, where the x-axis denotes the LPG position (spaced according to the output fuzzy sets) and the y-axis the FBG filter position. The intensity of the heatmap indicates the input strength, or preprocessed input value, for all LPG spectra within the binned values of the x-axis.

Upon examination of training data, it was observed that the input value x_i exceeded 0.5 when $\lambda_{res} \approx \lambda_{Bragg,i}$, while other inputs typically had values below 0.2. Additionally, it was noted that $x_i \approx x_{i+a}$ was greater than 0.3 when λ_{res} fell between $\lambda_{Bragg,i}$ and $\lambda_{Bragg,i+1}$. This understanding of the data enabled the determination of the membership functions depicted in Figure 17. Note that those values fluctuate regarding the LPG FWHM and those values were obtained by analysing the mean behaviour of the training set. Extreme cases such as narrower or wider LPG spectra would be presented as a combination of those cases. Consider two LPGs between two FBGs, one wide and another narrow, the wider LPG would have a greater membership to the fuzzy set N and close to none membership to F, however the narrower LPG might have lower membership to N and some to F. However, the rule base and the high noise resilience of FIS should tame such variations.

To fully define the FIS, only the rule-base was needed. Two primary situations arise in sparse filtering LPG interrogation: (i) when the resonant wavelength overlaps an

Figure 16 – Mean preprocessed values showing the relationship between the interrogator's input (y-axis) and desired output (x-axis).

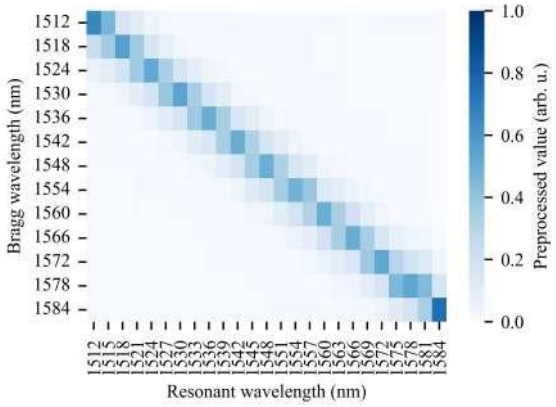

Source: [37] © 2022 IEEE.

Figure 17 – Fuzzy sets' membership functions.

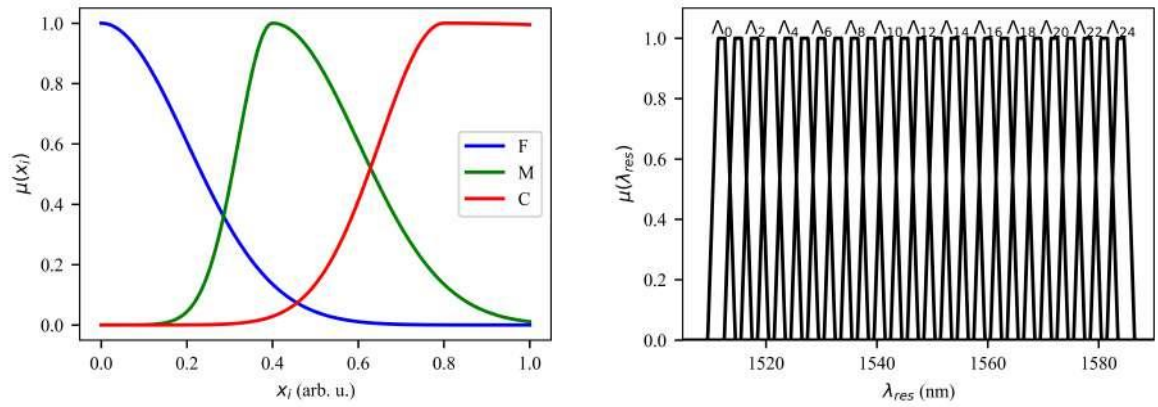

(a) Input sets

(b) Output sets

Source: [37] © 2022 IEEE.

input filter, and (ii) when the resonant wavelength falls between two input filters. While practical measurements are typically a superposition of these situations, two distinct rule groups were established accordingly. Hence, the grade of membership of the fuzzy set activated in each situation would allow the LPG resonance estimation by defuzzification. Group (i) rules are defined as:

IF (x_i is C and x_j is F, $\forall j \neq i$) THEN λ_{res} is $\mathbf{\Lambda}_{2i}$, $\forall i \in \{0, 1, ..., 12\}$

And group (ii) rules as:

IF (x_i is N and x_{i+1} is N) THEN λ_{res} is $\mathbf{\Lambda}_{2i+1}$, $\forall i \in \{0, 1, ..., 11\}$

The Mamdani inference system used the min and max operators for the t-norm and t-conorm, respectively. These definitions completed the FIS design. A key advantage of fuzzy inference systems lies in the seamless translation of human knowledge into the model. This "expert system" nomenclature stems from the ability of an expert to design the model based on prior knowledge, facilitated by the FIS's high interpretability and steps that mimic human reasoning.

However, the system's performance hinges on the membership function values, particularly the input ones. In many cases, decisions regarding these values can be somewhat arbitrary, as was the case here. Although guided by the inspection and analysis of Figure 16, determining optimal parameters for the membership functions using human reasoning alone is challenging. Therefore, the membership functions were also optimized using a genetic algorithm (GA) [129].

The GA optimization held certain parameters of the FAR set fixed, specifically $\sigma_1 = \mu = 0$. The search intervals for the remaining parameters were $\sigma_1, \sigma_2 \in [0, 0.5]$ and

$\mu \in [0.2, 0.8]$ for the NEAR set, while for the CENTERED set, the search space was $\sigma_1, \sigma_2 \in [0.1, 3]$ and $\mu \in [0.1, 1]$.

The GA was configured with 200 randomly initialized individuals, optimized over 100 epochs. Parameters were encoded into a numerical vector p, with a mutation frequency of 0.05. Half of the population was replaced by the 100 most fit children at the end of each epoch. The crossover function employed a random weighted mean:

$$p_{child} = \frac{a\ p_{parent\,1} + b\ p_{parent\,2}}{a + b} \tag{4.2}$$

where a and b were randomly chosen from $(0, 1]$.

The fitness function was defined as the mean squared error (MSE) of the resonant wavelength estimated by the fuzzy system using the population-based input membership functions during fuzzification. A stopping criterion halted optimization when the MSE improvement between the most fit individuals of two consecutive epochs fell below 0.0001 nm^2.

4.2.3 Evaluation of the FIS system

The fuzzy models, both expert-fitted and GA-fitted, were compared against the neural network model designed in Chapter 3 and against a linear model using the FBGs' position-to-intensity weighted mean. The latter used the linear model:

$$\hat{\lambda}_{res,\,\mathrm{linear}} = a(\mathbf{x} \cdot \lambda_{\mathbf{FBG}}) + b \tag{4.3}$$

where a and b were fitted using the least squares method on the training dataset.

The evaluation metrics were those used in Chapter 3: mean absolute error (MAE), mean squared error (MSE), mean of residues, and standard deviation of residues. Given the expectation that the FIS would be noise resilient, additive white Gaussian noise (AWGN) was added to the test set filter power, and the models were compared in terms of their resilience to noise.

4.3 RESULTS OF FIS-BASED INTERROGATOR

The genetic algorithm optimization of the input membership functions modified the expert-defined membership functions significantly. Figure 18 shows the difference between the expert-defined and GA-optimized memebership functions in dotted and solid lines, respectively. Note that there is a considerable difference between the membership functions of the sets F and C. An increase in the N membership function asymmetry was also observed, with a bigger σ_2 while μ remained similar to the value defined by the expert analysis of the data shown in Figure 16. This difference suggests the mean values shown

Figure 18 – Comparison between the expert defined and G.A. optimized input membership functions.

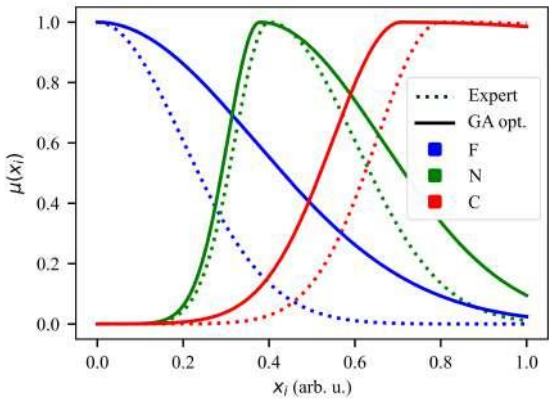

Source: [37] © 2022 IEEE.

in Figure 16 tended to underestimate the F behaviour and overestimate the C behaviour, whereas the N membership was underestimated for bigger input values.

The MLP presented in Chapter 3 was retrained using the preprocessing methodology of equation (4.1). So, the two FIS models (expert-defined and GA-optimized), the MLP model and the linear model of equation (4.3) were used to estimate the test set resonant wavelength. The results found in Chapter 3 and for all models considered in this chapter are summarized in Table 1.

Comparing the results found in Chapter 3 with the most simple baseline model using the input strength, a great improvement on the evaluation metrics could be seen. Note that the the proposed linear model's MAE, MSE, and uncertainty were greatly reduced using the novel preprocessing when compared to the MLP proposed in Chapter 3. This reduction implies the proposed preprocessing step improves the relationship between the FBG array data and the LPG resonant wavelength.

A visual comparison between the observed (target) and estimated residuals for

Table 1 – Metrics overview.

	Chapter 3	**Linear model**	**MLP**	**FIS expert**	**FIS GA opt.**
MAE (nm)	1.00	0.762	0.668	0.443	0.352
MSE (nm²)	1.98	0.979	0.737	0.317	0.242
μ **(nm)**	-0.033	-0.031	-0.083	-0.124	-0.101
σ **(nm)**	1.41	0.989	0.854	0.549	0.481

Source: Adapted from [37].

Figure 19 – Observed vs residual resonant wavelength.

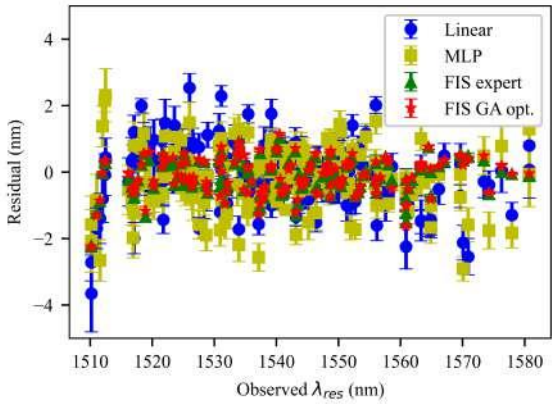

Source: [37] © 2022 IEEE.

λ_{res} is presented in Figure 19. The estimated resonant wavelength was obtained from ten measurements under noise (SNR = 10 dB). These results demonstrate strong agreement between the actual and estimated LPG resonant wavelengths across all models. Notably, the mean behaviour of the models closely aligns with zero residual. Indeed, an R^2 value exceeding 0.99 was also estimated for all models, indicating their effectiveness in explaining the LPG resonant wavelength. However, some models exhibit greater variance around their mean behaviour, with data points more dispersed, as reflected in the σ and MSE values shown in Table 1.

Finally, the relationship between MSE and SNR was analysed. The test set MSE was calculated under each SNR, with this experiment repeated 100 times for each SNR using resampled AWGN. The resulting mean and standard deviation of the estimated MSE are presented in Figure 20. This plot reveals that the FIS models exhibit lower sensitivity to input noise across all considered SNR values. One can see that both the expert-defined and the optimized FIS have similar noise suppression abilities, however, the optimized model presented less variance over the tests made at the most noisy scenario. This results corroborated the assumption that a proper fuzzyfied variable is capable of powerfull processing under noisy conditions.

These results underscore that the proposed preprocessing method yields information regarding the LPG resonant wavelength that is both easier to interpret and process. The improved performance of the simple linear model compared to that in Chapter 3 supports this assertion. The proposed fuzzy inference system outperformed other baseline models, including the retrained MLP with the same structure as in Chapter 3. Notably, the FIS with optimized membership functions demonstrated a nearly twofold (1.8x) improvement in uncertainty compared to the MLP, indicating the superiority of the fuzzy approach for this

Figure 20 – Models' sensitivity to noise.

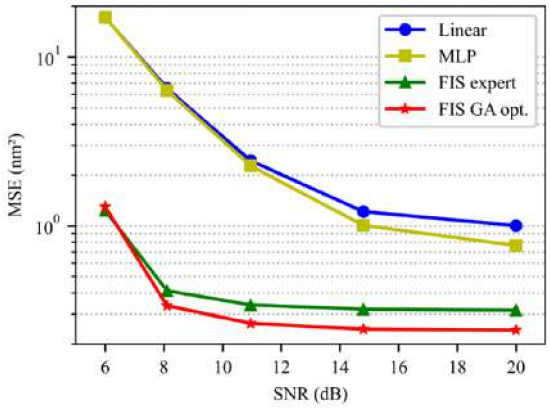

Source: [37] © 2022 IEEE.

problem. Importantly, the results under noise conditions highlight the FIS's remarkable noise resilience. However, it is crucial to consider that this noise insensitivity could potentially affect the detection of minor LPG fluctuations. Excessive noise suppression might inadvertently suppress small resonant wavelength changes that lead to subtle power fluctuations, thereby impacting the interrogator's resolution.

4.4 CONSIDERATIONS REGARDING THE FIS ESTIMATION

This chapter showed the use of a static sparse FBG array and a fuzzy inference system (FIS) to estimate the resonant wavelength of LPGs. The proposed FIS-based interrogator exhibited improved performance compared to the ANN-based approach, achieving a mean absolute error (MAE) of 0.352 nm and a root mean squared error (RMSE) of 0.481 nm. The system's ability to accurately estimate the resonant wavelength across a range of LPGs, coupled with its enhanced noise resilience, highlights its potential. The excellent noise suppression could be attributed to the fact that the rule base and pertinence functions are used to select the most influential inputs for each LPG sensor. Indeed, the noise suppression is a known and desirable feature of FISs.

However, the reliance on a static FBG array as a filtering element remains a limitation. The sensitivity of FBGs to temperature and vibration can introduce power fluctuations that affect the accuracy of the resonant wavelength estimation and makes the FIS output sets wrongly positioned. Additionally, the assumption of static FBGs restricts the system's applicability in scenarios where FBGs are used as sensors themselves, subject to dynamic changes in their reflected wavelengths.

Moreover, the high noise suppression of the FIS model raise concerns regarding the interrogation resolution. Is essential to consider that this noise insensitivity could

potentially affect the detection of minor LPG fluctuations. Excessive noise suppression might inadvertently suppress small resonant wavelength changes that lead to subtle power fluctuations, thereby impacting the interrogator's resolution as those could be interpreted as power noise. This concern underscores the importance of carefully balancing noise suppression and the preservation of subtle signal variations in the design of LPG interrogation systems.

The next chapter discusses the analysis and characterization of uncertainty in machine learning models, applied to the context of LPG interrogation. This will involve a detailed examination of the different types of uncertainty that can arise in the measurement process, as well as the development of methods to quantify and manage these uncertainties effectively. By addressing the issue of uncertainty, this study could further enhance the reliability and accuracy of the proposed LPG interrogation system and other machine learning applications in the field of sensing and metrology.

5 ADDRESSING UNCERTAINTY

In this chapter the uncertainty propagation through the machine learning models used for LPG interrogation is studied. The Monte Carlo method was proposed as a tool for determining how different uncertain scenarios impact the resonant wavelength estimation. In the next section the uncertainty characterization of machine learning models is discussed, followed by the methodology used for the Monte Carlo simulations, and the results obtained. Note that the main goal of this chapter is to present a metrological characterization of the ML-based LPG interrogator and to evaluate the noise suppression capabilities of ML models and the impact of such capabilities on the uncertainty propagation.

5.1 UNCERTAINTY IN MACHINE LEARNING MODELS

Uncertainty quantification is a critical aspect of machine learning, as it directly affects the credibility of models and the decisions based on their predictions. Machine learning models, especially complex ones, can often be overconfident in their predictions, even when faced with noisy, incorrect, or unfamiliar data. This overconfidence can have serious consequences after system deployment, particularly in high-stakes fields like healthcare [130–132] and autonomous driving [133–137].

While the concept of uncertainty in machine learning isn't new, the distinction between aleatoric and epistemic uncertainty has become increasingly important in recent years [138]. Aleatoric uncertainty, stemming from inherent noise or randomness in the data, is irreducible even with more data. Think of it like trying to predict a coin flip; no amount of information can eliminate the inherent randomness.

On the other hand, epistemic uncertainty arises from limitations in the model itself, such as insufficient data or an incomplete understanding of the underlying phenomenon. This type of uncertainty is reducible through improved models or more data. For instance, a medical diagnosis model might have high epistemic uncertainty if it's trained on a small patient sample or if the disease itself isn't fully understood. Another example would be that an industrial temperature control system trained with data from Germany would have high epistemic error when used in Mexico.

In the realm of instrumentation and measurement, these uncertainties are analogous to random and systematic errors. Aleatoric uncertainty, like random error, is unavoidable and must be well characterized and communicated. Epistemic uncertainty, like systematic error, can be reduced through better data collection or model refinement. Identifying and quantifying this type of uncertainty is key to improving a model's reliability and performance.

Various methods have been proposed to tackle uncertainty in machine learning and AI systems, often based on Bayesian frameworks [139], ensemble models [140], or evidential

reasoning [141]. A comprehensive review by Abdar et al. [142] delves into these methodologies for deep learning, highlighting their pros and cons. However, these approaches are primarily model-focused and aim to provide outputs paired with uncertainty estimates, not focusing on broader model-independent techniques for uncertainty characterization.

As discussed in Section 3.1, proper training and evaluation of data-driven models require splitting the dataset into training and testing sets. This ensures the model is optimized (trained) on data separated from that used for evaluation [143], mimicking the model use after implementation, with unknown data. Hence, model evaluation is performed by estimating metrics like MSE and MAE using a test set. However, lab-based evaluation may not fully reflect field performance due to the unpredictable nature of in-field scenarios. It's therefore important to anticipate potential challenges in model deployment [144], distinguishing between physical problems (e.g., data acquisition) and model errors [145].

One challenge is the need for large, representative datasets to minimize epistemic uncertainty. Transfer learning [146] has emerged as a way to address this, especially when obtaining measured data is difficult. Synthetic data has also been used for training deep learning models [147–149], and should allow for better model characterization, since more realistic data can be used for model evaluation instead of training.

In the context of LPG signal conditioning, effective training requires diverse data from multiple sensors, covering the full spectral window and a wide range of spectral characteristics. This ensures the interrogator can accurately estimate the resonant wavelength of any LPG sensor with similar characteristics to the training set, minimizing systematic error.

However, there's a tradeoff between spectral variability and single-sensor evaluation. Achieving high variability in practice can be tough, so one might prioritize training with fewer sensors but more measurements per sensor. Conversely, using multiple sensors might limit single-sensor variability due to time and resource constraints. The former approach improves model resolution and aleatoric uncertainty analysis using the test set but lacks variability. such approach potentially hinders model performance with unknown sensors, so the uncertainty characterization would be limited and representative of a limited set of sensor characteristics. The latter prioritizes model extrapolation (reducing epistemic uncertainty) at the cost of less accurate aleatoric uncertainty estimation.

Ideally, an interrogator should have minimal epistemic uncertainty and well-characterized aleatoric uncertainty. The approach in previous chapters favored extrapolation and lacked discussion on measurement uncertainty, specifically how the interrogator handles fluctuations in single-sensor measurements. While model bias and variance were estimated from test set residuals, the analysis didn't address single-sensor wavelength fluctuations.

Given the relative simplicity of the ML models used for LPG interrogation, compared to state-of-the-art, low epistemic uncertainty is a reasonable assumption. The limited parameter space compared to training samples further supports this. Therefore, this chapter focuses on characterizing aleatoric uncertainty. Note that machine learning offers robustness and noise suppression, as shown in Chapter 4. However, this can affect instrument resolution due to over-filtering of input fluctuations. This chapter investigates this effect by analyzing LPG uncertainty propagation through the ML model, ideally aiming for all fluctuations to be reflected in the output, thus preserving resolution.

5.2 METHODS FOR UNCERTAINTY CHARACTERIZATION

All the models presented in Chapters 3 and 4 were studied to characterize the uncertainty propagation through them. Since different models were considered, the methodology should be model-independent. Hence, the models were not modified, thus kept as developed in Chapters 3 and 4, but the test-set inputs were modified to add uncertainty. For such, the Monte Carlo Method was used to estimate the output uncertainty given an uncertain input. The equivalence between the Monte Carlo method for uncertainty calculation and the guide for uncertainty in measurement (GUM) methodology has been previously shown for a wide range of applications [150–152] and thus a similar approach was considered in this work.

Given that aleatoric uncertainty stems from the process and input uncertainties, our analysis focused solely on the latter. For LPG interrogation, the input varies due to both interrogator optoelectronics and LPG position fluctuations. To assess the model's performance under these conditions, semi-synthetic data was utilized. Such data was generated by modifying the test set samples through simulations. These modifications involved adding noise to the FBG filtered power, representing optoelectronic noise, and shifting the LPG resonant dip to simulate changes in LPG position.

Figure 21 outlines the step-by-step procedure used to simulate a single uncertain measurement. These steps were repeated 200 times for each test-set spectrum, considering both types of modifications (optoelectronic noise and LPG fluctuation). The optoelectronic noise was considered to evaluate the machine learning model's ability to filter noise introduced to the system during the FBG reflected power measurement. This type of noise is inherent to any electronic circuitry, although it can be reduced with proper circuit design and measurement conditions. One example of improvement by good measurement practice is to acquire several measurements and considering the mean value as the final value. Simulating a measurement with noisy power measurements involved using a test set spectrum to obtain the optical power filtered by each filter element, mimicking the interrogator hardware. Additive white Gaussian noise (AWGN) was then introduced to the input, as detailed in Chapter 4. The resulting array was processed by the ML algorithm

Figure 21 – Flowchart for generating a single uncertain measuremnt.

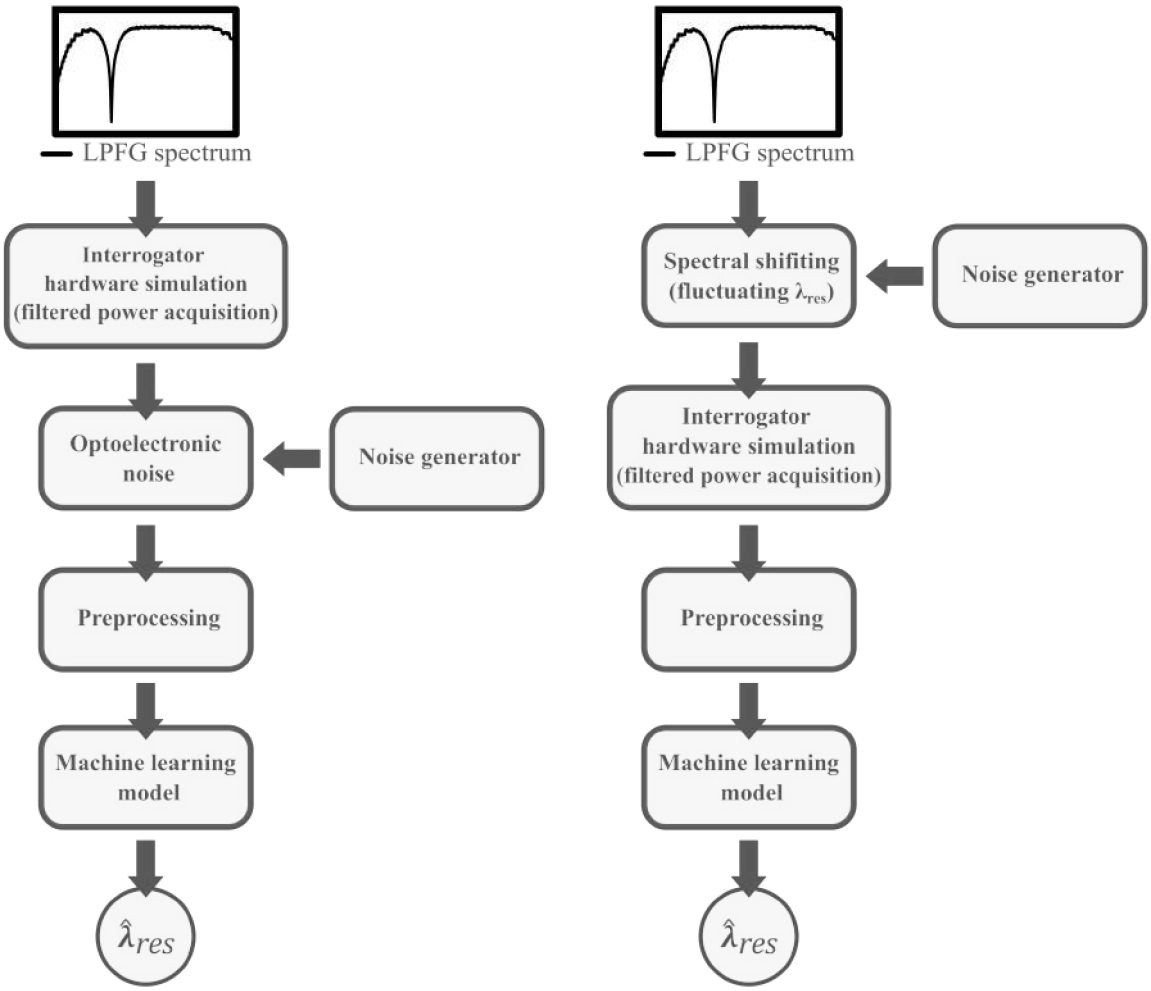

(a) Uncertainty due to optoelectronic noise

(b) Uncertainty due to LPG fluctuation

Source: [38] © 2024 IEEE.

to estimate the LPG resonant wavelength (Figure 21(a)).

The LPG fluctuation was considered to evaluate the measurand variability, i.e. the fluctuation induced to the LPG sensor by the environment. Such analysis is helpful to evaluate the measurand uncertainty propagation through the machine learning model. Ideally, the model should transmit every sensor fluctuation to its output. For simulating a measurement with noise from the LPG sensor itself, a test set spectrum was shifted, simulating a change in the resonant wavelength. The filtered power was then obtained by simulating the hardware, and the resulting array was processed by the ML model to estimate the resonant wavelength (Figure 21(b)). To accomplish such task in a practical sense, one could attach an LPG to a piezoelectric transducer and vary the voltage across it, obtaining a localized spectral shift with precision.

Figure 22 illustrates the effects of these steps on an LPG spectrum. Black parameters represent the static (ground truth) values, while red values indicate the noise added during the Monte Carlo simulations. Each case was simulated 20 times, representing 20 measurements.

While the impact of AWGN on the inputs was explored in Chapter 4 to assess hardware effects, the influence of slight deviations in the LPG position remained uninvestigated. To generate noise, the "numpy.random.randn" function was employed. These values were used to introduce hardware noise proportional to the input filtered power (given the SNR) and to shift LPG spectra, resulting in new optical power values at each filtering element. The hardware was then simulated, and the filtered data array was preprocessed according to the method described in Chapter 4.

Figure 23 visualizes the ML model input for the 20 noise simulations depicted in Figure 22, with color intensity representing input strength. This figure effectively illustrates the input uncertainty due to both optoelectronic noise (a) and fiber sensor fluctuations (b). In this and subsequent sections, these uncertainties will be denoted as u_a and u_b, respectively, and are associated with an input SNR and random LPG noise with a standard deviation of $\sigma_{\lambda_{res}}$.

This process of acquiring 20 samples for each test-set spectrum was repeated 10 times across various input uncertainties, yielding 200 simulations per test set spectrum. These simulations represented 20 measurements over 10 experiments, each experiment with a new random seed. The values used for u_a were 6, 8, 11, 15, and 20 dB, while the values for u_b were 0.10, 0.15, 0.24, 0.37, 0.57, 0.88, 1.36, 2.10, 3.24, and 5.00 nm.

Figure 22 – Example of uncertainties at the interrogator input.

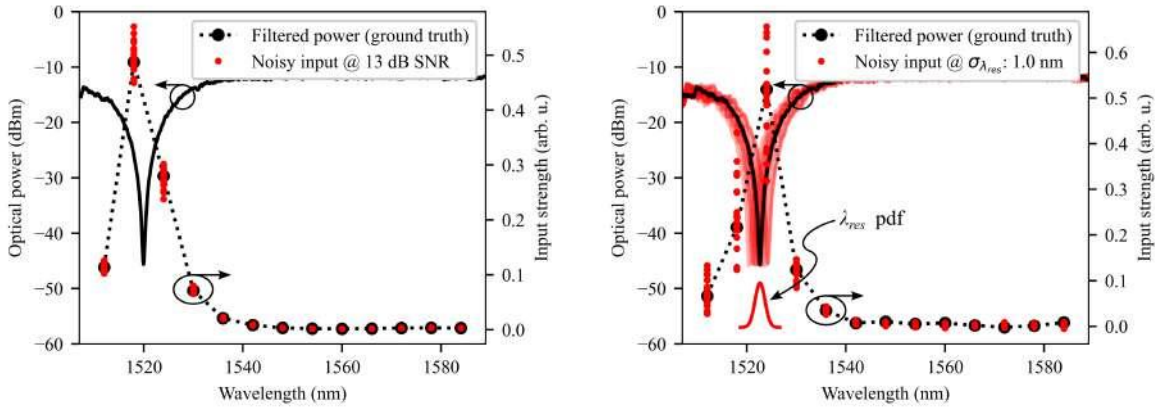

(a) Uncertainty due to optoelectronic noise

(b) Uncertainty due to LPG sensor fluctuation

Source: [38] © 2024 IEEE.

Figure 23 – Time series of the input values shown in Figure 22.

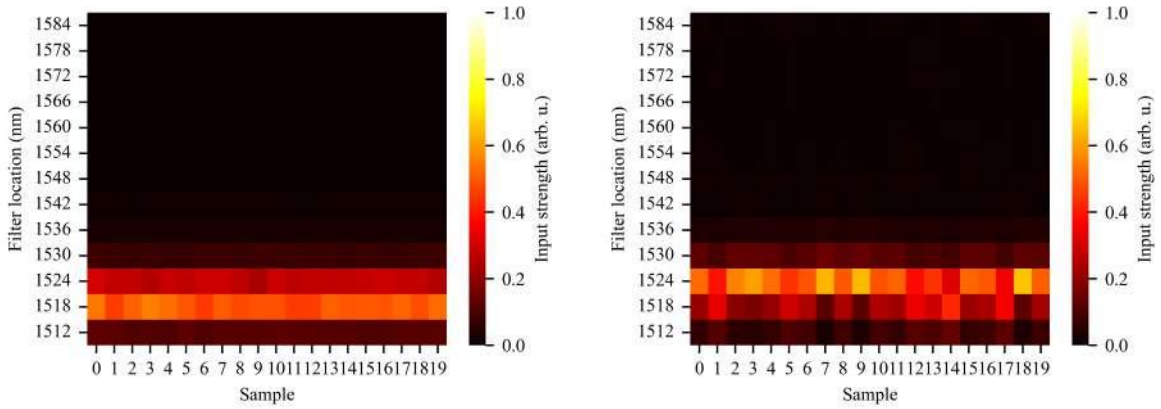

(a) Optoelectronic noise

(b) LPG sensor fluctuation

Source: [38] © 2024 IEEE.

The resulted resonant wavelength estimation for each Monte Carlo simulation was compared to the real resonant wavelength, resulting in a residual $r = \lambda_{res} - \hat{\lambda}_{res}$. The residue statistics for each noisy measurement scenario was considered. Hence, the residue bias and standard deviation was studied regarding the input noise and its variance over the 10 experiments.

5.3 RESULTS OF UNCERTAINTY PROPAGATION

The following sections discuss the results obtained through the Monte Carlo simulations, the propagation of optoelectronic noise and the propagation of LPG noise are presented.

5.3.1 Uncertainty due to optoelectronic noise

To assess the impact of optoelectronic noise on the LPG interrogator's performance, varying levels of additive white Gaussian noise (AWGN) was introduced into the simulated FBG filter power readings. This simulated noise represents the inherent variability and uncertainty introduced by the optoelectronics in a field sensing system. Analysing the resulting deviations in the estimated resonant wavelength, allows to evaluate model's robustness in the presence of this type of noise.

Figure 24 illustrates the interrogator's bias as a function of u_a (optoelectronic noise) for each model. The results showed the bias does not exhibit a clear trend with respect to SNR, except for the linear model under high noise, which showed substantial variability across experiments. Conversely, the standard deviation demonstrates a clear

increasing trend correlated with the input noise (Figure 25). These results align with the MSE findings in Chapter 4, highlighting the lower noise susceptibility of the ML models, especially the FIS models.

Based on these results, one can infer that input noise does not significantly affect the bias of the more robust models (MLP and FIS) tested in this work. The typical bias range (with a 95% confidence interval) for the considered u_a values was calculated to characterize each models' polarization. The linear model's bias ranged from 0.240 nm to 0.028 nm, the MLP's from 0.074 nm to 0.093 nm, the FIS-ex's from 0.123 nm to 0.124 nm, and the FIS-ga's from 0.101 nm to 0.102 nm. These findings, consistent with previous results, provide valuable insights for characterizing potential models for the interrogator's processing.

The high noise insensitivity of the FIS-based models can be attributed to their focus on FBGs near the LPG's resonant wavelength. These models primarily utilize data from these nearby FBGs. Therefore, after fuzzification, minor fluctuations in FBGs far from λ_{res} do not significantly impact the resonant wavelength estimation, as these changes are not substantial enough to be considered part of the NEAR or CENTERED fuzzy sets (see Chapter 4.2 for details).

Despite using all input data to estimate the resonant wavelength, like the linear model, the MLP model displayed much lower noise sensitivity, consistent with MLPs' known noise immunity [153]. In contrast, the linear model's input is a function of the input strength and its inner product with the FBG position. This makes it highly susceptible to small noisy variations in FBGs far from the LPG dip (low input strength). These distant wavelengths can introduce substantial errors in estimation. Moreover, as noise increases, bias estimation becomes increasingly difficult due to the heightened impact of these distant

Figure 24 – Bias due to input power SNR.

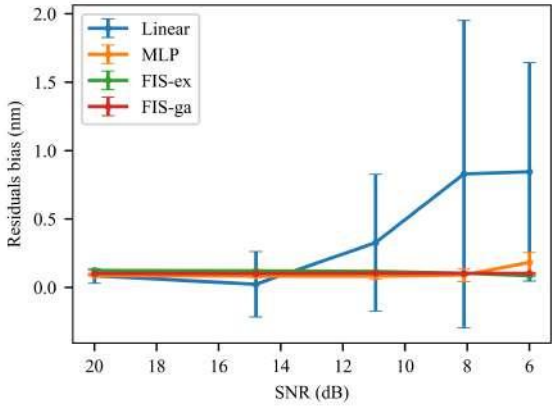

Source: [38] © 2024 IEEE.

Figure 25 – Standard deviation due to input power SNR..

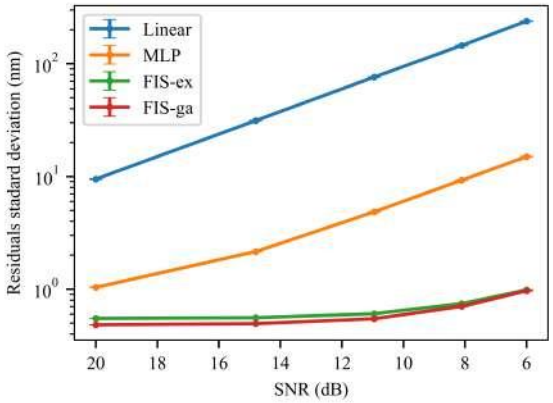

Source: [38] © 2024 IEEE.

inputs. In extreme cases, the bias variability could span the entire interrogator's full scale, as noise in distant filters becomes pronounced.

This effect might indicated that the tested ML models have a primitive form of attention. This can be attributed because the observed low deviation for these models is likely due to the minimal influence of input strengths from FBGs far from the resonant wavelength on the final estimation.

Notably, the variance of the metrics remained low across the 200 simulations (20 measurements over 10 experiments), indicating a sufficient number of Monte Carlo iterations in most cases. The exception is the linear model's residuals' bias under high noise, which, as discussed, is an inherent characteristic of the model itself.

5.3.2 Uncertainty due to the LPG fluctuations

While the noise resilience of fuzzy-based models is advantageous, it's important to investigate whether this insensitivity to high noise levels might compromise the interrogator's resolution. This concern arises because as the models dampen variations in the FBG's filtered power, they might not fully translate all LPG fluctuations to the estimated resonant wavelength. In essence, noise robustness could potentially lead to a loss of interrogator resolution.

To examine this effect, the impact of minor fluctuations in the LPG resonant wavelength (u_b) on the estimated value should be studied. Hence, the effect on the bias and standard deviation of the residuals, similar to our previous analysis, was considered. Figure 26 shows the bias as a function of u_b. The results indicate that the bias does not correlate with the input fluctuation. Therefore, the typical bias range for fluctuating LPGs was estimated. The range calculated was 0.028 nm to 0.030 nm for the linear model, 0.081

nm to 0.083 nm for the MLP, 0.120 nm to 0.122 nm for the FIS-ex, and 0.099 nm to 0.101 nm for the FIS-ga. These values demonstrate the stability of the proposed interrogator, as they align with previous findings, and offer insights into the models' epistemic uncertainty.

Unlike optoelectronic noise, which affects all inputs, LPG fluctuations occur primarily near the resonant wavelength. Consequently, results did not show as significant variations as before, particularly for the linear model. This suggests that the ML models noise suppression, or attention, is less critical for LPG variations, indicating that the sensor's uncertainty propagates effectively through the model.

For the residuals' standard deviation, it is desirable for all input fluctuations (representing the resonant wavelength standard deviation) to be passed through the model to the estimated resonant wavelength. Ideally, a 1:1 ratio between u_b and the residual standard deviation is desired. However, measuring instruments have inherent resolution limits, so not all minor fluctuations can be transferred to the interrogator's output. Indeed, the results in Figure 27 demonstrate that the residuals' standard deviation plateaus at a certain value.

The concern that the more noise-robust models (fuzzy-based) might dampen LPG fluctuations was dispelled, as the estimated standard deviation of the residuals was never smaller than u_b. In fact, for smaller LPG fluctuations, the estimation was worse, as expected for any measuring instrument. Additionally, for fluctuations above the interrogator's estimated resolution (twice the standard deviation shown in Table 1), the ratio between input and output fluctuations approached 1:1. This suggests that under normal circumstances, all input fluctuations (u_b) should be transmitted through the model to the estimated resonant wavelength. The estimated resolution for each model is illustrated in Figure 27 as dotted lines. As noted previously, the low variance of the

Figure 26 – Bias due to LPG sensor fluctuation.

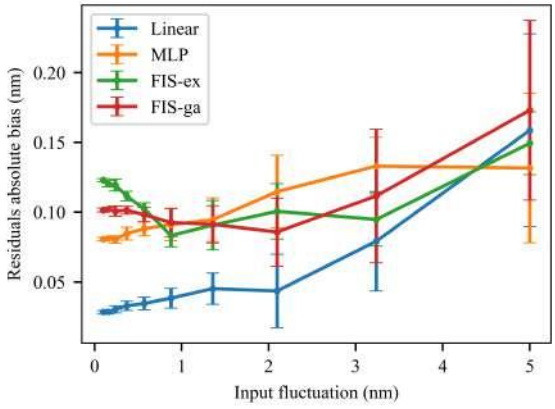

Source: [38] © 2024 IEEE.

Figure 27 – Standard deviation due to input power LPG sensor fluctuation.

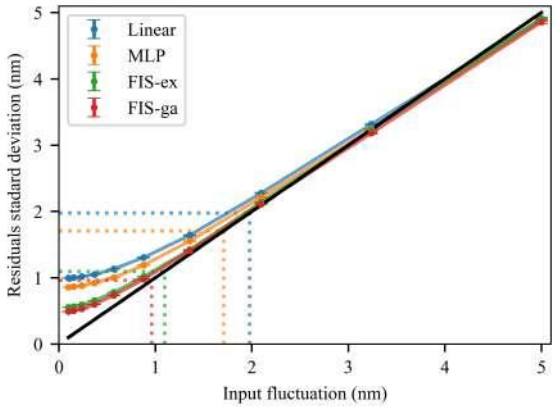

Source: [38] © 2024 IEEE.

metrics reaffirms the sufficiency of the number of iterations used in this study.

5.4 CONSIDERATIONS REGARDING THE UNCERTAINTY PROPAGATION

This chapter explored the impact of uncertainty on the performance of the proposed LPG interrogation system. By employing the Monte Carlo method, the propagation of uncertainties originating from both optoelectronic noise and LPG fluctuations was successfully characterized. The analysis revealed that while all models demonstrated a certain degree of resilience to noise, the fuzzy inference system (FIS) exhibited superior performance, particularly in suppressing the impact of optoelectronic noise. This highlights the potential of FIS-based models for accurate and reliable LPG interrogation in noisy environments.

The investigation of uncertainty propagation through the models revealed an interesting trend. The analysis of LPG fluctuations showed that the noise suppression capability of the models did not impact LPG fluctuations that were greater than the estimated interrogator's resolution. This finding indicates that the models effectively filter out noise while preserving significant LPG fluctuations, ensuring accurate and reliable measurements.

Although the finding presented in this chapter does not add any performance upgrade on the machine learning models, it encourages further development, as it showed the models are indeed focused on extracting information relevant to the LPG demodulation problem, while filtering undesired features. The developed methodology for uncertainty characterization, based on the Monte Carlo method, offers a valuable tool for evaluating the performance of different interrogation models and guiding the design of more robust and reliable systems.

6 SYNTHETIC DATA AND THE MULTI-SENSOR APPROACH

This chapter presents significant advancements in LPG demodulation using an FBG array, with focus on a more practical implementation. A key limitation of previously reported systems is the requirement for static FBGs, despite their inherent temperature and strain sensitivity. To address this limitation and align the system more closely with practical fiber optic sensor networks, a promising solution is proposed that allows FBGs to function as both sensing elements and filters. This approach culminates in a multi-sensor network, although it still not solves the LPG multiplexing challenges, it improves the overall sensing system cost-effectiveness by introducing non-static FBGs.

Indeed, the use of FBGs as sensing elements the system's cost-effectiveness can be enhanced due to its multi-point sensing capabilities. This allows FBGs to be used for strain and temperature sensing, while the LPG serves as a versatile sensor for various measurands, derived from its SRI sensitivity, that are not accessible by FBGs alone. Furthermore, a combination of two FBGs can compensate for the LPG's cross-sensitivity to strain and temperature, paving the way for a fully quasi-distributed sensing system that leverages the strengths of both technologies. In this way, commercially available FBG interrogators could be adapted to acquire the reflection spectra of the FBG array, with the reflection intensity modulated by the LPG sensor.

The following sections delve into this approach, which utilizes a conventional FBG sensing system with a cascaded LPG sensor. This configuration leverages the high fidelity of commercially available FBG interrogators to acquire the reflection spectrum of the FBG array, where the intensity of the reflection peaks is modulated by the LPG sensor. Subsequently, the LPG position is demodulated using a machine learning model. Given that the FBGs are now acting as sensors and are subject to movement, the model complexity is increased, necessitating more data for training. However, the problem is well-understood and can be readily simulated. Therefore, synthetic data was employed for model design and training, while real data was used for model evaluation.

6.1 SYNTHETIC DATA GENERATION

The optoelectronic system employed in this chapter diverges from the setups described in previous chapters, opting for a simpler and readily available configuration based on a commercial FBG interrogator. Figure 28 illustrates the considered setup, where the LPG sensor and FBG sensor array are cascaded in series. This setup comprises thirteen FBGs with center wavelengths spanning from 1510 to 1590 nm, approximately, alongside the LPG sensor. A commercial-grade FBG interrogator was used, FS22DI BraggMeter from HBM, with the LPG sensor connected to a channel, followed by the FBG array.

It's crucial to highlight that simply cascading the LPG and FBGs would result

Figure 28 – Schematic of the optical setup considered in this chapter.

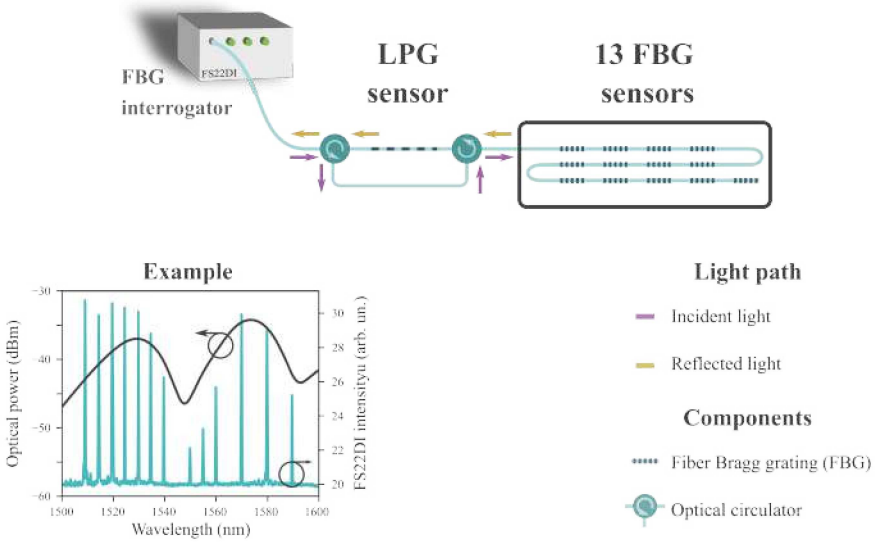

Source: Figure elaborated by the author.

in light traversing the LPG sensor twice, leading to substantial optical attenuation. To mitigate this, a pair of optical circulators was implemented to ensure that only light reflected by the FBG array interacts with the LPG sensor.

With this FBG array, the ability to demodulate LPGs within the 1515 to 1585 nm range should be guaranteed. It's worth noting that alterations in the FBG array distribution could impact the LPG demodulation capability. However, the system can be tailored to specific FBG arrays, as the proposed model is designed to be agnostic to FBG positioning. The machine learning model requires FBG location and intensity as input, enabling the use of any interrogator capable of retrieving this information.

Training a robust machine learning model necessitates a large, diverse dataset encompassing a wide range of LPG characteristics and FBG array configurations. Acquiring such a dataset solely through measurements is impractical due to time and resource constraints. However, synthetic data could enable the use of big machine learning model. In [154] the authors propose a ML-based Fabry-Perot interferometer (FPI) sensor interrogator. The authors highlight the challenge of obtaining sufficient measurements for training and utilize a Wasserstein Generative Adversarial Network (WGAN) to generate synthetic data that accurately mimics the distribution of real sensor data. Nevertheless, the use of generative model might be unnecessary. For most optical fiber sensors, the sensor spectrum can be mathematically modelled or at least approximated with ease. For an LPG, for example, its transfer function can be effectively approximated by mathematical functions like modified Gaussian and Lorentzian functions.

Capitalizing on this principle, synthetic LPG spectra was generated with diverse parameters, including coupling efficiency (LPG attenuation intensity), resonant wavelength (central wavelength of the LPG's dip in the transmission spectrum), spectral width (sharpness of the LPG's spectral dip), secondary dips (to mimic real spectral ripples), and out-of-range dips (to enhance model generalization by simulating scenarios where dips fall outside the FBG array's range).

FBG simulation followed a similar approach, with random Bragg wavelengths. In total 400,000 data samples were generated for model selection, and an additional 1,000,000 were generated to fine-tune the selected model. The foundation of a synthetic spectrum is a Lorentzian-shaped LPG transmission:

$$T_{\text{Lorentzian}}(\lambda) = -a\left(1 + \left(\frac{\lambda - \lambda_{res}}{\frac{w}{2\sqrt{\left|\frac{a}{3}-1\right|}}}\right)^2\right)^{-1} - b \tag{6.1}$$

where b represents the device's insertion loss, and the resonant dip's parameters are depth (a), center (λ_{res}), and width (w).

Additionally, a Gaussian-shaped LPG transmission was also used:

$$T_{\text{Gaussian}}(\lambda) = -a\exp\left(-\frac{(\lambda - \lambda_{res})^2}{4s^2}\right) - b, \quad s = 2\sqrt{\left|4\ln\left(\frac{a}{3.01}\right)\right|} \tag{6.2}$$

where, similarly, b is the insertion loss, and the resonant dip's parameters are depth (a), center (λ_{res}), and width (w).

The synthetic LPG spectra were generated using a combination of these functions:

$$T_{\text{LG}}(\lambda) = kT_{\text{Lorentzian}}(\lambda) + (1-k)\,T_{\text{Gaussian}}(\lambda) \tag{6.3}$$

with $k \in [0, 1]$. Examples of synthetic resonant dips created using the parameters listed in Table 2, applied to equation (6.3), are shown in Figure 29. Figure 29(a) displays resonant dips, while Figure 29(b) shows the same dips with added ripples and dips outside the interrogator's range, enhancing spectral variability. The final T_{Synth} was obtained by summing T_{LG} with random noisy dips generated using the same function, as shown in Figure 29b, effectively creating a random linear combination of T_{LG}.

FBG reflection peaks were simulated by generating a 13-element random array, which served as input for generating the LPG spectrum. Only the points at each FBG sensor were calculated, optimizing speed and memory usage. For each simulated example, the FBG position and $T_{\text{Synth}}(\lambda_{Bragg,i})$, $\forall i \in \{1, ..., 13\}$, were recorded.

All the synthetic spectra considered in this work was randomly generated using uniform probability distribution function with the following ranges: $a \in [10, 40]$ dB,

Figure 29 – Example of generated synthetic spectra.

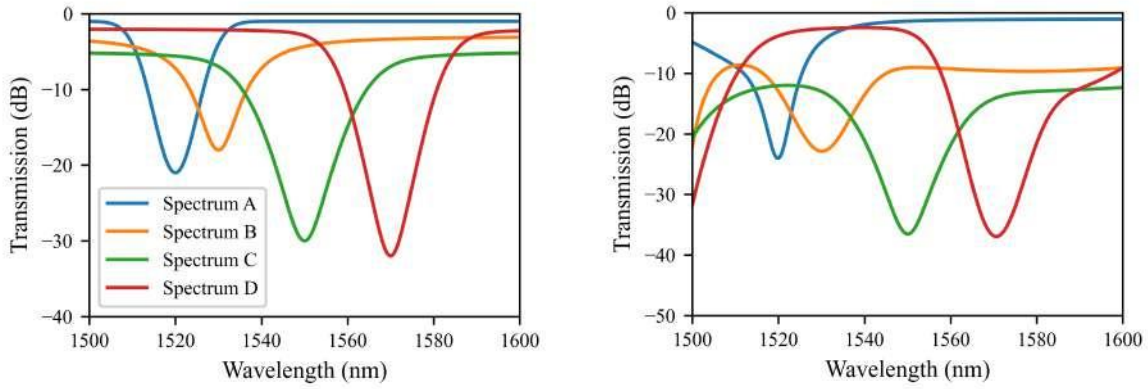

(a) Single dip synthetic spectra, T_{LG}.

(b) After random ripples and dips, T_{Synth}.

Source: Plots elaborated by the author.

Table 2 – Parameters of synthetic spectra shown in Figure 29.

	a **(dB)**	λ_{res} **(nm)**	w **(nm)**	b **(dB)**	k
Spectrum A	20	1520	20	1	0.0
Spectrum B	15	1530	25	3	1.0
Spectrum C	25	1550	35	5	0.5
Spectrum D	30	1570	30	2	0.3

Source: Author.

$\lambda_{res} \in [1515, 1585]$ nm, $w \in [15, 40]$ nm, $b \in [0, 10]$ dB, $k \in [0, 1]$. The FBGs' Bragg wavelengths were also shifted considering a uniform distribution up to half the array spacing.

6.2 METHODS FOR SA-FCN MODEL DESIGN AND CHARACTERIZATION

This section presents the methodology used to develop the interrogation method based on a self-attention model. The model, preprocessing, evaluation techniques, and methods for practical evaluation are presented.

6.2.1 The SA-FCN model

The proposed model for LPG demodulation in this scenario is a self-attention-based fully connected neural network (SA-FCN), designed to be independent of FBG positions within the array. This aligns with the concept of "input strength," which indicates the

relative proximity of the LPG to each FBG sensor. Hence, the inner product of the input strength vector and the Bragg wavelength vector should directly yield the LPG position.

However, the raw input strength alone lacks information about the absolute FBG positions and the LPG spectrum itself. To overcome this, the self-attention model uses the FBGs position alongside the input strength. The model then refines the input data by generating a "filtered input strength" vector. This filtered vector, when used in an inner product with the Bragg wavelengths, is expected to accurately estimate the LPG position.

Figure 30 shows the model architecture, which includes two hidden layers, "hidden 1" and "hidden features," both for feature extraction and representation in a higher-dimensional space. However, not all extracted features are necessarily relevant, potentially including noise, spectral fluctuations, or out-of-range dips.

To filter out irrelevant elements, the model employs a self-attention mechanism, known for its effectiveness in sequential problems and complex data abstraction [155, 156]. The attention map, generated similarly to the hidden features but with a softmax activation, modulates the hidden features through point-wise multiplication. The attention map's dynamic nature is key, as it's generated on-the-fly for each input. This allows adaptive focus on the most relevant features for robust and generalizable filtering in LPG demodulation.

The model outputs a 13-element vector whose inner product with the Bragg wavelength vector should accurately estimate the LPG position. The model was implemented

Figure 30 – Self-attention fully conected neural network.

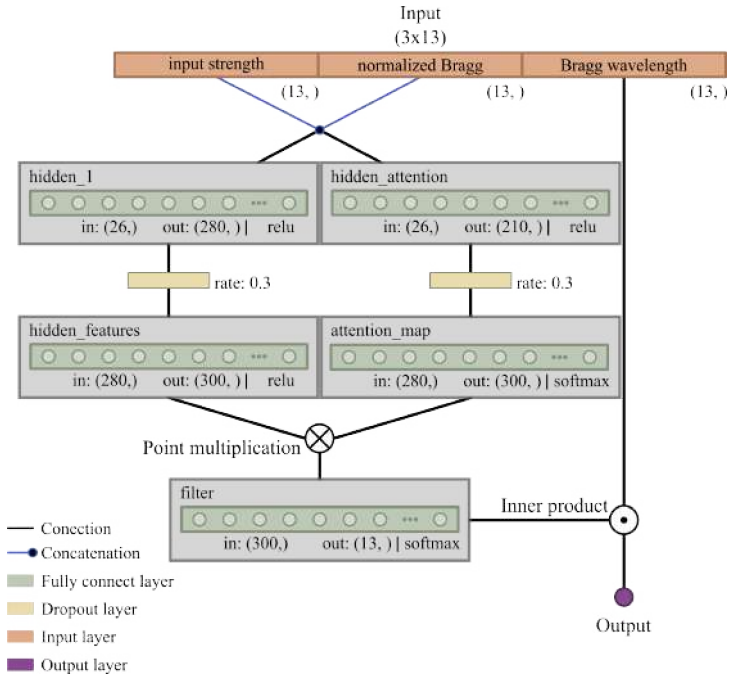

Source: Figure elaborated by the author.

using the Keras (v2.15) [157] functional API with tensorflow backend (v2.15).

Hyperparameter optimization involved 200 trials of Bayesian optimization, exploring layer sizes from 100 to 300, dropout rates from 0.1 to 0.3, and different activation functions (ReLU, tanh, sigmoid). The model was trained using the Adam [158], due to its superior performance for large datasets and models, with a learning rate of 0.001. The optimization aimed to fit to both the target resonant wavelength and filter output. The target filter output was calculated based on the relative FBG-LPG distances, ensuring the inner product with the Bragg wavelength vector yields the target LPG resonant wavelength.

6.2.2 Spectral analysis and data preprocessing

The model's input is derived from the reflection spectra obtained by the FS22DI interrogator. The spectra are processed to extract each Bragg wavelength and reflected intensity using a Gaussian approximation of each reflection peak. Note that this is a highly robust approach, with relative demanding execution time; for faster execution, peaks and resonant wavelengths can be obtained directly by the interrogator.

This 2x13 data array (reflection peaks' intensity and position) undergoes four preprocessing steps before being fed into the machine learning model:

- **Baseline Removal:** Raw peak intensities are subtracted from a baseline measurement acquired without the LPG. This compensates for variations in individual FBG reflectivities.
- **Normalized Input Strength:** The resulting peaks are divided by their total intensity, yielding an "input strength" array ranging from 0 to 1. Each value represents the relative contribution of a specific FBG, indicating its proximity to the LPG sensor.
- **Normalized Bragg Wavelength:** A copy of the Bragg wavelength array (extracted from the reflection peaks) is normalized between 0 and 1, using the minimum and maximum possible operating wavelengths (e.g., 1500 nm and 1600 nm).
- **Feature Concatenation:** The normalized Bragg wavelength array is merged with the initial data array (containing normalized input strength).

This process results in a 3x13 feature matrix, where each row represents the input strength (relative FBG contribution), normalized Bragg wavelength, and absolute Bragg wavelength. This preprocessed matrix serves as the input for the machine learning model, comprehensively representing the sensor array response for LPG demodulation. Figure 31 summarizes these preprocessing steps, with the FBG reflection in solid red and the LPG representation in dotted blue. The point plot illustrates the preprocessed data: the input.

Figure 31 – Preprocessing example.

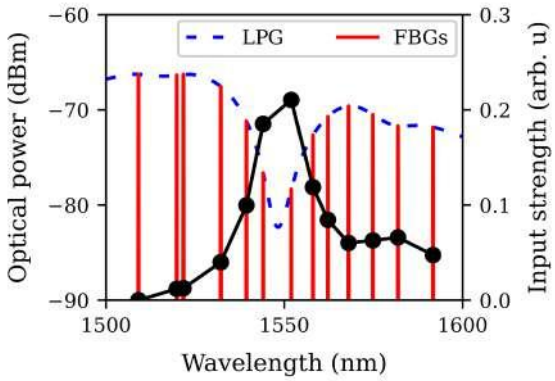

Source: Plot elaborated by the author.

6.2.3 Evaluation on measured spectra

The proposed model was evaluated using 73 LPG transmission characteristics, measured by an Anritsu MS9740B optical spectrum analyzer. All from LPGs manufactured by the setup shown in Figure 7 and five LPG transmission characteristics can be seen in Figure 32. For each LPG, 100 different FBG configurations were considered, resulting in a total of 7,300 test data samples. The performance of the proposed model was compared against a robust fitting method that adjusted the FBGs' reflection to a Lorentzian function. The robustness of this method was achieved by employing several parameter restrictions based on the FBG array, thereby optimizing the fitting results. The evaluation metrics

Figure 32 – Spectra of five randomly selected LPGs used to evaluate the synthetic training.

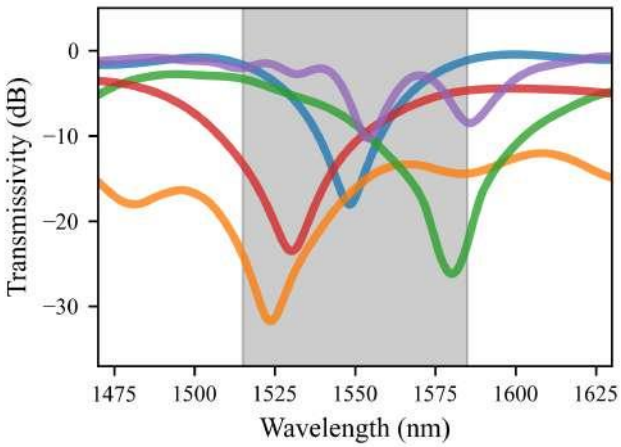

Source: Plot elaborated by the author.

included R^2, root mean squared error (RMSE), and mean absolute percentage error (MAPE).

6.2.4 A practical measurement: SRI sensor

Additionally, to showcase the practical applicability of the proposed SA-FCN model for LPG demodulation, an experiment was conducted using an LPG refractive index (RI) sensor in conjunction to an FBG array. The inclusion of an RI LPG sensor is consistent with the multi-point sensing scheme of our proposal, as FBGs inherently measure strain and temperature. Furthermore, changes in the surrounding refractive index affect the LPG's coupling efficiency, making this an excellent opportunity to assess the interrogation capabilities when both resonant wavelength and attenuation vary.

To enhance the mechanical stability of the LPG sensor and facilitate its application, it was embedded within a custom-designed microfluidic chip. Figure 33 provides a visual overview of the fabrication process. First, a micro tapered LPG was inscribed in a standard single-mode fiber (SMF-28) using the electric arc discharge technique (using the equipment shown in Figure 7). Next, a 3D-printed microfluidic chip was fabricated using a Phrozen Sonic Mini 8k resin 3D printer and Standard Clear resin from 3Dlab. The chip design

Figure 33 – Steps for the refractive index manufacturing.

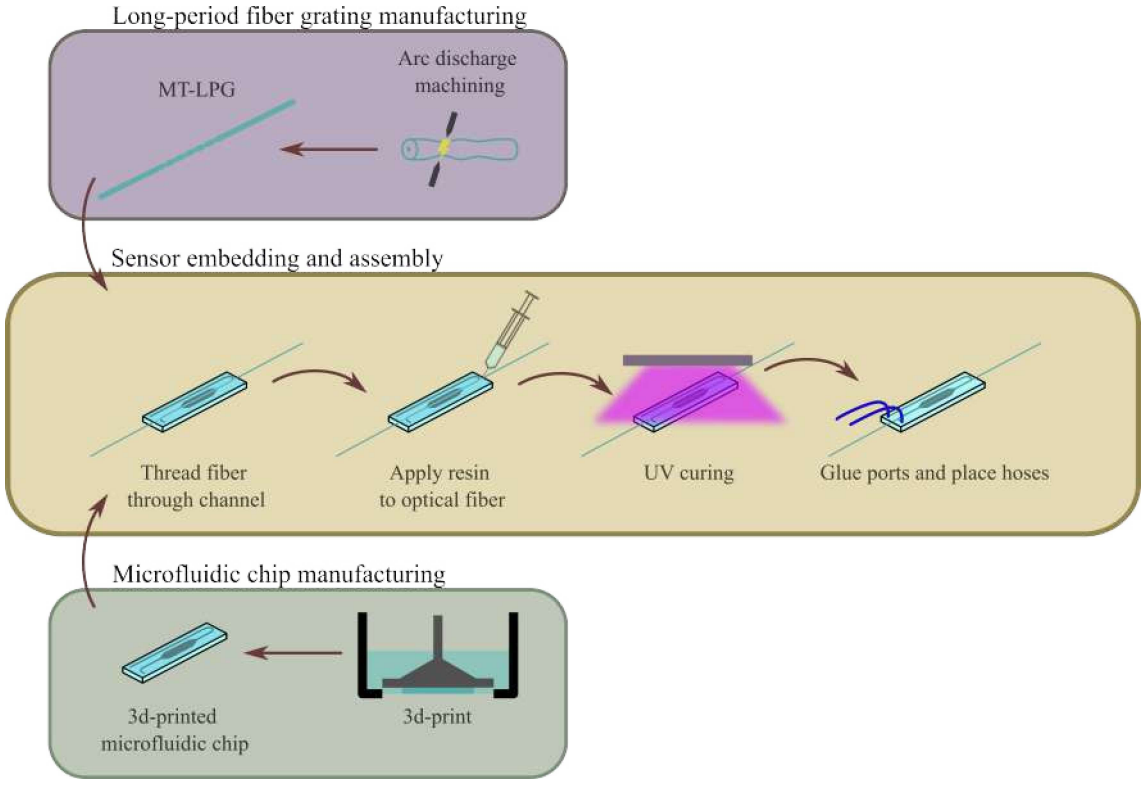

Source: Figure elaborated by the author.

incorporated two distinct channels: one to accommodate the flow of the sample and another specifically designed to house the fiber optic sensor.

The assembly process involved carefully threading the fiber with the inscribed LPG through the designated channel in the chip, ensuring its proper alignment and positioning within the sample channel. To secure the fiber in place and seal the channel, UV-curable resin was applied. Upon exposure to UV light, the resin solidified, effectively fixing the sensor within the chip. Finally, inlet and outlet ports were glued to the chip, enabling the connection of tubing for sample introduction and removal.

The microfluidic chip with LPG sensor was first characterized using an Anritsu MS9740B and calibrated for RI from 1.34751 $\pm$ 0.00018 to 1.3928 $\pm$ 0.0004 RIU. The RI samples were prepared with water and glycerol at 10% to 50% water/glycerol volume concentration. After sample preparation, the refractive index (RI) of each mixture was measured using an Abbe refractometer, those values outside the instrument were extrapolated based on the water/glycerol concentration to RI curve. Note that visible range RI was considered, which is standard for applications such as sugar content measurement.

6.3 RESULTS OF MULTI-SENSOR APPROACH

The results obtained for the self-attention model are presented as follows: first the system characterization using synthetic and measured LPG spectrum, and then the system evaluation in a practical measurement.

6.3.1 System characterization

First, let's evaluate the attention mechanism. Synthetic data was used to ensure complete control over the inputs, allowing for a detailed analysis of how the hidden feature map and attention map adapt to various scenarios. These scenarios, illustrated in Figure 34, include: (a) LPG shifting, (b) LPG spectrum distortion, and (c) FBG shifting. This investigation focused on the model's response to changes in the LPG's position within the sensor array, its ability to handle spectrum distortions, and its robustness to shifts in the FBG array position.

The results yielded several key observations. When the LPG's resonant wavelength (central dip) shifts, the attention map undergoes notable changes. This indicates that the model effectively focuses on relevant features within the hidden features based on the LPG's spectral position. Interestingly, the hidden feature maps themselves show minimal variation in this scenario.

In contrast, when the resonant wavelength remains constant but the spectrum is distorted (e.g., through the introduction of ripples or additional dips), the attention map exhibits only minor modifications. This suggests the model's capability to filter out such

Figure 34 – Evaluating the attention mechanism with input change.

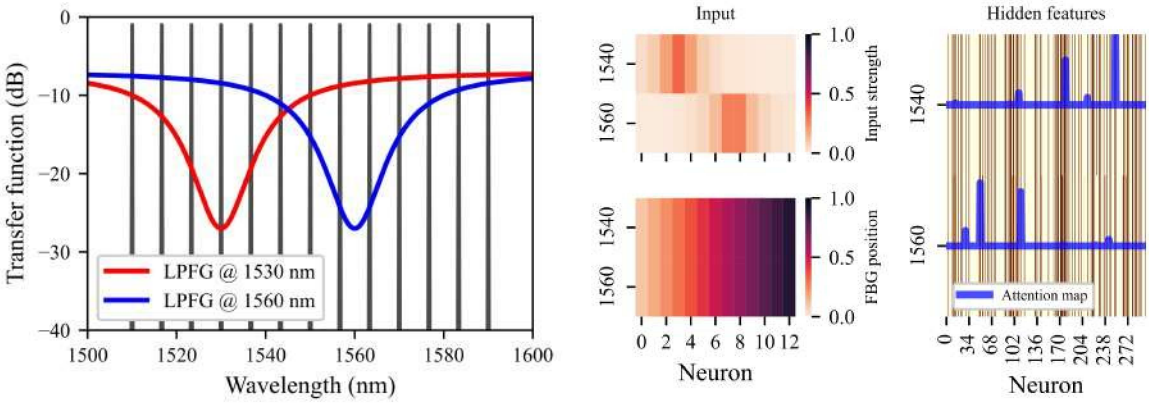

(a) Shifted LPG

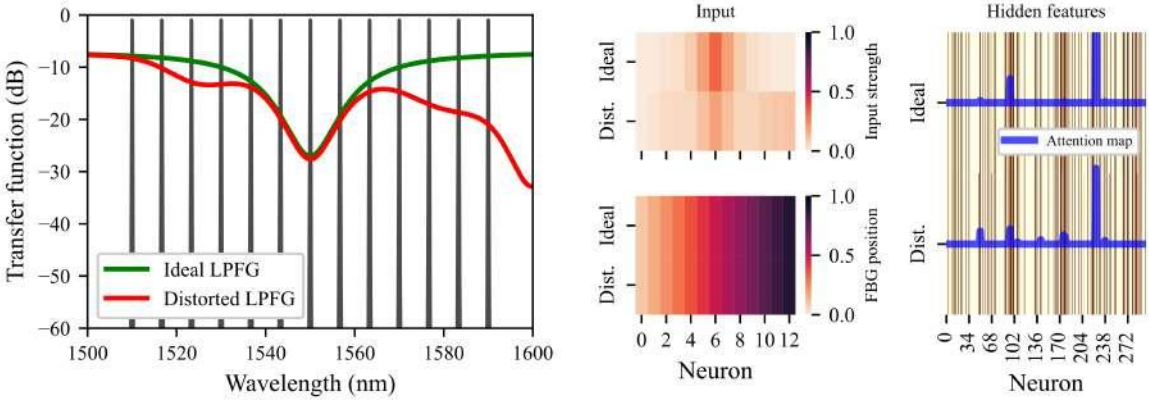

(b) Distorted LPG

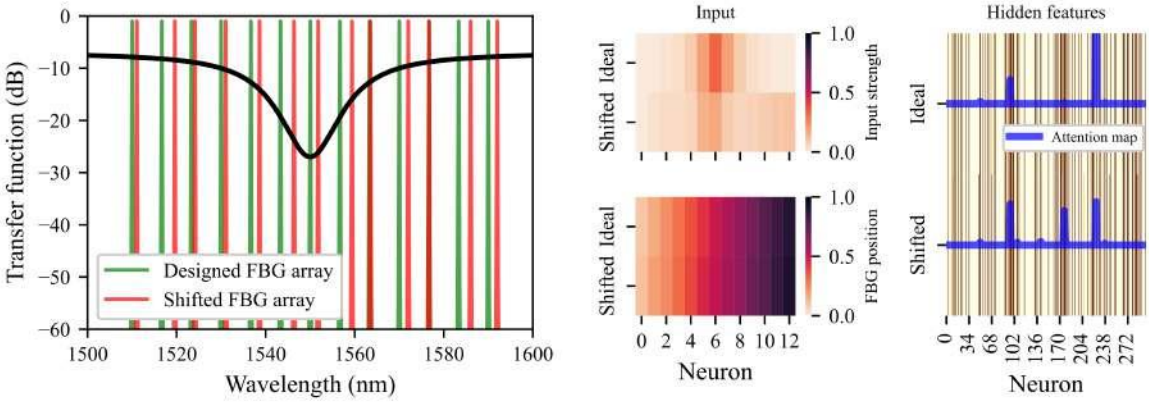

(c) FBG shift

Source: Plot elaborated by the author.

spectral distortions, concentrating on the core features essential for LPG demodulation.

When the FBG sensor array is shifted, the attention map displays a slight spread. However, the crucial features of interest remain prominent, demonstrating the model's

adaptability to minor variations in the FBG array position while maintaining accurate LPG demodulation.

While this initial analysis provided valuable insights into the model's filtering behaviour, it relied on a limited set of examples. To better address the model's behaviour for different LPG inputs, each layer output was analysed using 5000 random samples with one controlled parameter at a time. An LPG wavelength sweep was performed, and the remaining parameters (depth, FWHM, insertion loss, FBG positioning) were uniformly sorted. This process was repeated for each LPG parameter to evaluate if the model's attention is indeed focused on the LPG resonant wavelength. Figure 35 shows the output value of each layer's neurons; clear values represent more neuron activation.

The results showed the neuron activation is highly sensitive to the LPFG resonant wavelength in all layers. Hence, the weights encode the resonant wavelength, with a singular neuron combination for each spectral region. For the dip depth and width, there was no clear correlation with the neuron activation. These results showed the model effectively focuses on the resonant wavelength information because the mean neuron behavior was only regarding the resonant wavelength. Note in Figure 35(a) that the neuron activation for the four layers considered was greatly affected by the LPG resonant wavelength. Hence, the neurons capture the sensor's position, and the model successfully demodulates the LPG sensor. Also, the coupling efficiency, resonance width, and FBG position randomly varied, and the mean value is presented, so the wavelength encoding is indeed strong.

On the other hand, the results for resonance dip depth and width showed the model does not clearly respond to these variables. Although some neurons might be activated regarding these spectral features, the mean behavior for the neurons remained constant when those varied, as shown in the horizontal lines of Figure 35(b) and Figure 35(c).

However, the true test of the model's effectiveness lies in its ability to deal with in-field scenarios. In this section, the high-resolution and stability capabilities of an OSA were crucial to characterize an actual LPG spectra. By feeding these real spectra into the self-attention model for LPG demodulation, the efficacy of the proposed approach could be evaluated. This evaluation is crucial for demonstrating model's potential. Indeed, it assess how well the model, trained on synthetic data, can handle the complexities and imperfections present in actual LPG measurements. Here, the real LPG spectra might contain noise, spectral variations not captured perfectly by the simulations, and other deviations from the ideal conditions assumed during synthetic data generation. Evaluating the model's performance with these practical challenges will solidify the promise of synthetic training and transfer learning for LPG demodulation using FBG sensor arrays.

As previously stated, in this evaluation, 73 LPG spectra from various arc-induced sensors were tested. Each spectrum was evaluated using 100 FBG array configurations to comprehensively assess the model's generalizability. Alongside each estimated value,

Figure 35 – Neuron activation by LPG parameter.

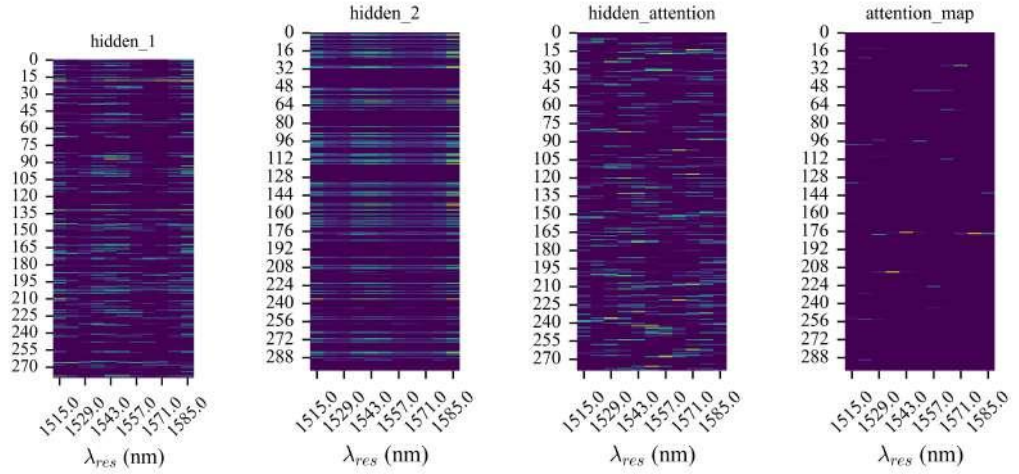

(a) LPG resonant wavelength

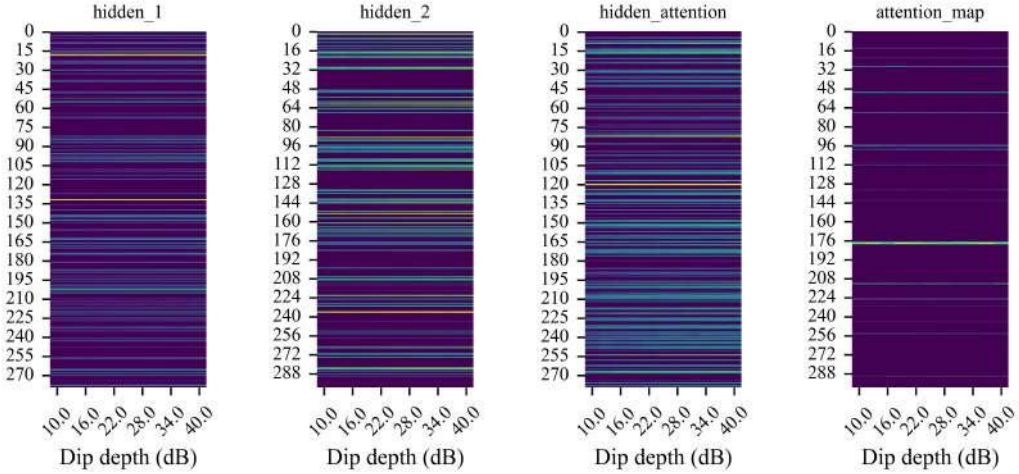

(b) LPG coupling efficiency (resonant dip depth)

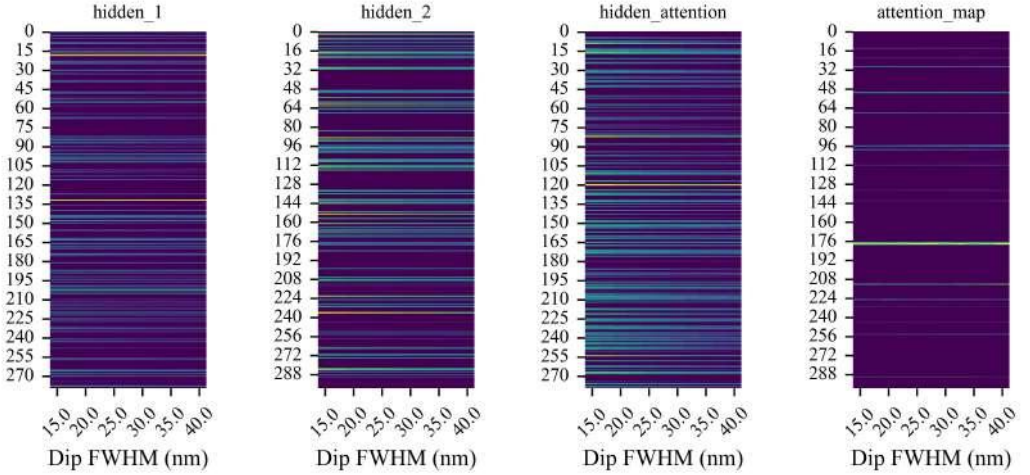

(c) LPG full width at half maximum

Source: Plot elaborated by the author.

Figure 36 – Regression evaluation plot showing the target LPG position vs estimated LPG position.

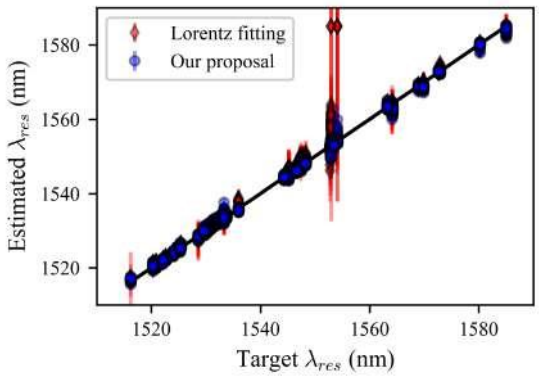

Source: Plot elaborated by the author.

the model's dropout layers were used to quantify model uncertainty [138, 142, 159]. Additionally, each data point was processed using a Lorentzian fit, and uncertainty was estimated based on the fitted parameter's covariance matrix. Figure 36 compares the performance of the proposed model with the baseline Lorentzian fitting approach.

The findings demonstrated that the baseline model performs well for relatively simple spectra. However, for sensors with an additional resonant dip falling outside the FBG array's range (but potentially detectable by some FBGs), the baseline model's estimation suffers (evident in the outliers near 1555 nm). This is likely due to the high variability of actual LPGs compared to the ideal Lorentzian function, leading to high parameter uncertainty in these cases. Figure 37 shows the LPG spectra which the Loretzian

Figure 37 – LPG spectra which the Lorentz fitting baseline underperforms.

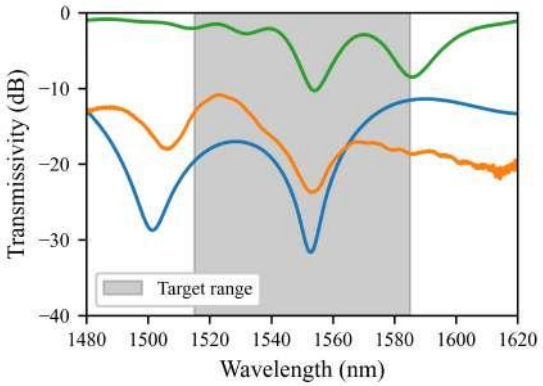

Source: Plot elaborated by the author.

Table 3 – Resulting performance metrics.

		R^2	RMSE (nm)	MAPE (%)
Proposed	*All data*	0.9977 ± 0.0002	0.75 ± 0.02	0.0335 ± 0.0001
model	*Without outliers*	0.9980 ± 0.0001	0.70 ± 0.02	0.0321 ± 0.0001
Lorentzian	*All data*	0.982 ± 0.006	2.13 ± 0.35	0.050 ± 0.002
fitting	*Without outliers*	0.9973 ± 0.0003	0.83 ± 0.04	0.039 ± 0.002

Source: Author.

fit error was greater than 5 nm, note that those had lots of ripples, at least a secondary resonance, or a very distorted resonant dip.

The proposed model with the attention mechanism addresses these limitations. The attention layer effectively filters out irrelevant features, including those associated with resonant dips outside the FBG array range. This targeted filtering significantly improves the model's accuracy compared to the baseline approach. Table 3 summarizes the performance metrics calculated using the measured LPG spectra. The models were compared using the entire dataset and a subset excluding poorly fitted spectra by the Lorentzian model. In all aspects, the proposed model outperforms the baseline model, for both the complete and filtered datasets. These results are comparable to previous findings for neural networks trained with real LPG data and static FBGs. This reinforces the effectiveness of both the FBG sensor interrogation technique for LPG sensors and the proposed transfer learning approach using synthetic data.

Overall, the evaluation using real LPG spectra validates the effectiveness of synthetic data training with transfer learning for LPG demodulation. This approach offers a promising solution for practical scenarios where acquiring a large dataset of LPG measurements might be time-consuming or resource-intensive.

6.3.2 Results for the SRI sensor

To showcase the practical applicability of the proposed SA-FCN model for LPG demodulation, an experiment was conducted using an LPG refractive index (RI) sensor. The sensor utilized for practical application was an arc-induced micro-tapered grating (MT-LPG) with a resonant wavelength of approximately 1540 nm, a full width at half maximum of 53 nm, an insertion loss of 4.33 dB, and an attenuation dip of 15.45 dB (all parameter measured in air). The transmission spectrum of the device in air can be seen in Figure 38.

The FBG array of 13 sensors had the following spectral characteristics: Bragg wavelength: 1510.005, 1515.530, 1521.245, 1529.905, 1538.610, 1544.1, 1549.91, 1555.595, 1561.275, 1572.765, 1578.560, 1587.090, and 1590.160 nm. And FWHM of all devices was

Figure 38 – LPG refractive sensor in air.

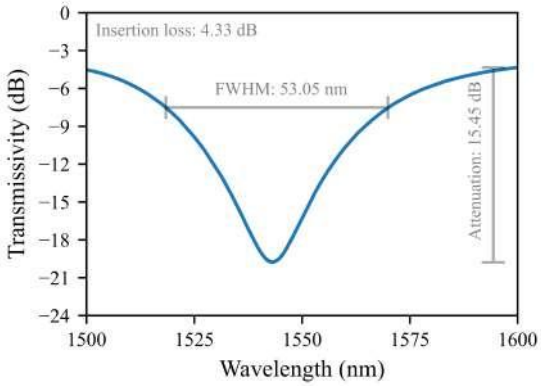

Source: Author.

within 0.226 ± 0.003 nm.

Hence, the setup showed in Figure 28 was assembled as shown in Figure 39(a). This photography focus on the sensors (LPG and FBG array) and samples, so the interrogator is not showed. Additionally, one can see in detail the microfluidic chip used as sensing element in Figure 39(b). Note that the MT-LPG was embedded into this 3D-printed microfluidic chip and glued using the same resin used for printing it.

Liquid samples with different refractive index were introduced into the microfluidic chip using a syringe and a hose. The microfluid port has a male Luer fitting so the female Luer fitting of the hose was used. The microfluid chip's output port was connected to an open discard reservoir with a similar hose.

Figure 39 – Setup for LPG demodulation tests.

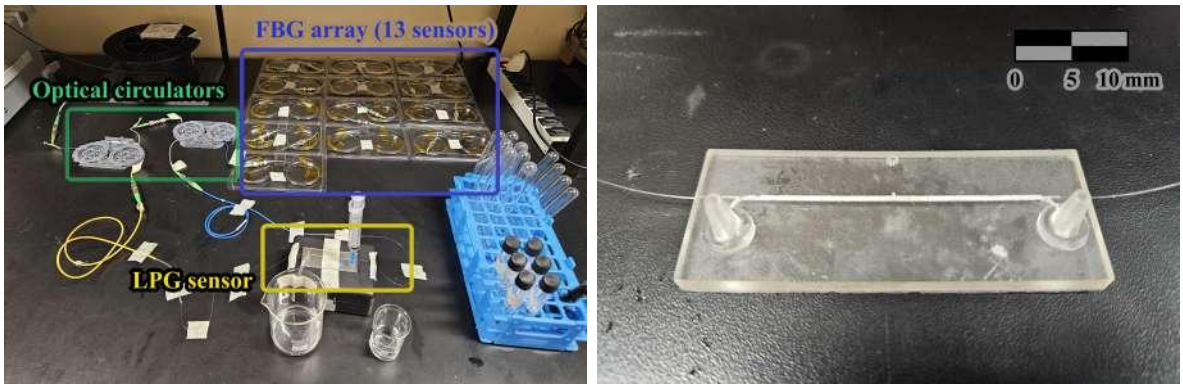

(a) Setup for SRI measurements (b) Microfluidic chip with MT-LPG

Source: Author.

Figure 40 – LPG sensor calibration.

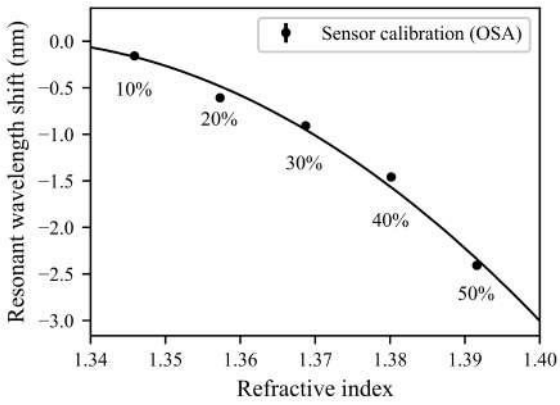

Source: Author.

Different concentrations of water/glycerol mixtures, ranging from 10% to 50%, were prepared as test samples. After every sample the sensor was rinsed with pure water to remove any leftover sample. Since the sensor was rinsed before every new sample, we considered the wavelength shift from water to water/glycerol mixture to calibrate the sensor. This makes the calibration procedure easy and effectively mitigates errors due to temperature and strain cross-sensitivity.

Figure 40 presents the calibration curve obtained using the Anritsu MS9740B OSA, while Figure 41 displays the measurements obtained using the proposed demodulation method with a 2-second sampling interval. During calibration, a blue shift of the resonant dip towards lower wavelengths was observed, accompanied by a reduction in resonance dip attenuation. Although the proposed system does not directly estimate dip attenuation,

Figure 41 – LPG demodulation by the proposed method.

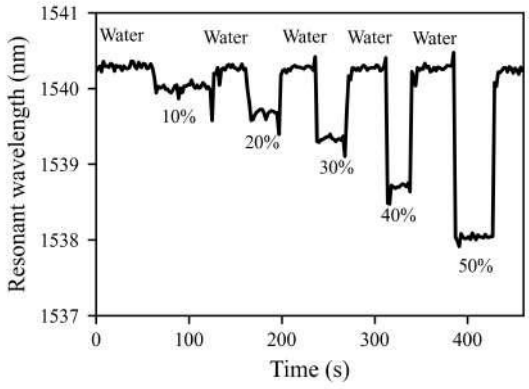

Source: Author.

Figure 42 – Comparisson between target and estimated RI.

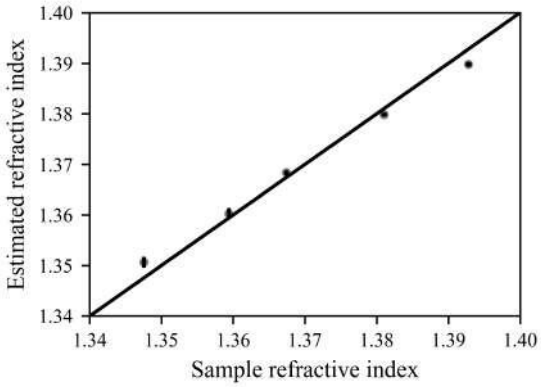

Source: Author.

the sensor's blue shift is clearly evident in Figure 41. This indicates that the proposed method successfully captured both sample variations and transitory states during sample changes.

The blue shift relative to the water sample was calculated and applied to the calibration curve to estimate the sample's refractive index. The resonant wavelength for each sample step and its refractive index (estimated and target) can be seen in Table 4. Figure 42 shows a comparison between the sample RI and the estimated value. The estimation was made considering the mean resonant wavelengths from each step in Figure 41 and the calibration curve from Figure 40. The residuals analysis showed a RI bias of 0.0001 RIU and a residual standard deviation of 0.001 RIU. Note in Figure 42 that most error occurs for lower RI, where the sensitivity is smaller (see Figure 40). This indicates that the error might not be due to wrong resonant wavelength estimation, but to poor sensor response. Indeed, wrong resonant wavelength estimation would introduce more RI error at the higher sensitivity part of the sensor response because little wavelength

Table 4 – Measurements performed by the RI sensor.

Sample	**Resonant wavelength (nm)**	**Estimated RI**	**Sample RI**
10%	1540.01 ± 0.02	1.350 ± 0.001	1.34751 ± 0.00018
20%	1539.67 ± 0.03	1.360 ± 0.001	1.35938 ± 0.00022
30%	1539.34 ± 0.01	1.3683 ± 0.0005	1.36740 ± 0.00026
40%	1538.71 ± 0.01	1.3799 ± 0.0003	1.38103 ± 0.00032
50%	1540.25 ± 0.01	1.3898 ± 0.0004	1.3928 ± 0.0004

Source: Author.

difference would imply great RI difference.

This practical experiment demonstrates the effectiveness of the proposed SA-FCN model for real-time LPG demodulation in a multi-sensor configuration. The system's ability to accurately track changes in the LPG's resonant wavelength, even with varying attenuation dips, underscores its potential for use in various sensing applications. The combination of a commercially available FBG interrogator, a 3D-printed microfluidic chip, and a robust machine learning model offers a promising pathway for developing cost-effective and reliable LPG sensing systems for in-field deployment.

6.4 CONSIDERATIONS REGARDING SYNTHETIC TRAINING AND THE SENSOR NETWORK

This chapter introduced a novel approach to LPG demodulation that utilizes a commercially available FBG interrogator and a self-attention fully connected neural network (SA-FCN). The proposed system leverages the strengths of both LPG and FBG technologies, enabling multi-point sensing and enhancing cost-effectiveness. By employing synthetic LPG spectra for model training, the SA-FCN effectively addresses the challenges of limited measured data and achieves accurate and robust LPG demodulation. The attention mechanism within the model allows for adaptive filtering of irrelevant features, further improving performance and creating a robust sensor network.

The evaluation of the proposed system using real LPG spectra validated its effectiveness, demonstrating high accuracy and generalization capabilities. The results highlight the potential of this approach for practical scenarios where acquiring large measured datasets is challenging. The simplicity, cost-effectiveness, and adaptability of the proposed system make it a promising tool for advancing LPG sensing technology and facilitating its widespread adoption in various applications.

However, it is important to acknowledge that the reliance on synthetic data for training might introduce limitations in capturing the full complexity and variability of actual LPG characteristics. Future research could explore the use of hybrid datasets, combining synthetic and measured data, to further enhance the model's robustness and generalizability. Transfer learning and fine-tuning the model on in-field data could also be promising, as well as domain adaptation techniques.

7 CONCLUSIONS

In this thesis, the problem of interrogating long-period fiber grating (LPG) sensors was addressed. The main goal was to develop a cost-effective and reliable LPG interrogation system that could be easily deployed in the field. The main design constraint was to develop an LPG-agnostic model, i.e., that could estimate the LPG sensor position without any prior knowledge of its transfer characteristic. To achieve this goal, a novel approach was proposed that combines a sparse optical filter bank and machine learning.

The proposed approach was thoroughly investigated through three distinct methods, each building upon the previous one, with a focus on the resulting practicability. The first method employed a static FBG array and a neural network to estimate the LPG resonant wavelength. The second method refined this approach by incorporating an improved preprocessing technique and a fuzzy inference system. Finally, the third method introduced a self-attention-based fully connected neural network and the use of a traditional FBG interrogator, enabling the use of FBG filters as sensing heads. A summary of the proposed methods can be seen in Table 5.

The results obtained throughout this thesis demonstrate the effectiveness and potential of machine learning in LPG sensor demodulation. The developed LPG interrogators exhibited high accuracy, robustness to noise, and the ability to generalize to a wide range of LPG sensors and FBG array configurations. The approach considered for the self-attention model considerably improves the current state of FBG-LPG sensor networks. The use of a well-established FBG interrogation unit coupled with the proposed self-attention method allowed for the adaptive filtering of irrelevant features, further enhancing the LPG demodulation. As a consequence, the method allowed the demodulation of any given LPG cascaded to any FBG array. This has a significant impact on the sensing system's cost-effectiveness, since the cost-per-sensor reduces when more sensors can be interrogated by the same optoelectronic device.

For developing and training such a complex machine learning model, the use

Table 5 – Features of machine learning methods for FBG-filter-based LPG demodulation.

Method	**LPG agnostic**	**Optoelectronic noise resilience**	**Robust to FBG position**	**Number of sensing heads**
Neural network	✓			1
Fuzzy inference	✓	✓		1
Self-attention	✓	✓	✓	14

Source: Author.

of synthetic data proved to be a valuable strategy. Training with synthetic data was crucial to overcome the limitations of acquiring large datasets containing diverse enough measured data. Hence, future model topologies should not be limited by the amount of data available for training, allowing the development of more robust and complex models for LPG demodulation.

The main limitations found for the neural network and fuzzy inference methods were regarding filter stability and cost. Note that the acquisition system needs a circulator and photodetector per FBG. However, the increasing adoption of integrated photonics might solve these two problems. Note that concentrating all filters into a small space eases temperature control or compensation, and integration also reduces cost due to scale manufacturing. The self-attention approach is mainly limited to a set of applications where multiple sensors are needed, to compensate for the FBG interrogation unit. However, the horizon for FBG demodulation systems is promising, with ever increasing number of suppliers and cost-effective solutions.

Even so, the proposed LPG interrogation system offers several advantages over existing methods, potentially addressing long-lasting challenges in the field. Its simplicity, cost-effectiveness, and adaptability to different FBG array configurations make it a promising tool for various applications, including structural health monitoring, environmental sensing, industrial process control, and biomedical detection. The use of machine learning algorithms not only improves the accuracy and robustness of the system but also opens up new possibilities for future research and development in this field.

Indeed, the perspectives for this research topic are promising. The continuous improvement of machine learning topologies, models, and training strategies would benefit the accuracy and reliability of the proposed demodulation paradigm. Such development should be facilitated by the use of synthetic data. The use of residual networks, encoders, adversarial generative networks, and in-field learning are promising approaches for future research. Regarding training, the use of transfer learning and domain adaptation should improve the performance over measured data substantially. So future research could focus on:

- **Model development:** investigate the performance of models such as convolutional neural networks (CNNs), recurrent neural networks (RNNs), and encoders, for LPG demodulation.
- **Knowledge transfer:** investigate the use of transfer learning and domain adaptation to further improve the performance of the models trained with synthetic LPG spectrum.
- **Sensor head:** investigate the use of other wavelength-encoded sensors, such as Mach-Zehnder and Fabry-Pérot interferometers.

- **Synthetic data generation:** use of generative models to develop the training dataset, physics-based simulators, or even physics-informed generative models.

In conclusion, this thesis has made significant contributions to the field of LPG sensor interrogation. Different machine learning models and architectures were presented and should provide a comprehensive guide to the development of others. The synthetic data approach overcomes the time-consuming task of acquiring measured data and improves the cost-benefit of machine learning for LPG demodulation. The results presented in this thesis pave the way for further advancements in LPG sensing technology and its widespread in-field adoption. By addressing the limitations of existing LPG interrogation methods, this work has opened up new possibilities for the development of cost-effective, reliable, and versatile sensing systems for a wide range of applications.

REFERENCES

1 LÓPEZ-HIGUERA, J. *Introduction to fibre optic sensing technology.* Wiley, 2004. p. 1–22.

2 ZHENG, S. Long-period fiber grating moisture sensor with nano-structured coatings for structural health monitoring. *Structural Health Monitoring: An International Journal*, v. 14, p. 148–157, 3 2015.

3 HUANG, Y.; TANG, F.; LIANG, X.; CHEN, G.; XIAO, H.; AZARMI, F. Steel bar corrosion monitoring with long-period fiber grating sensors coated with nano iron/silica particles and polyurethane. *Structural Health Monitoring: An International Journal*, v. 14, p. 178–189, 3 2015.

4 BARINO, F. O.; FARACO-FILHO, R.; CAMPOS, D.; SILVA, V. N. H.; LOPEZ-BARBERO, A. P.; DE MELLO HONORIO, L.; DOS SANTOS, A. B. Loading condition estimation using long-period fiber grating array. *IEEE Sensors Journal*, v. 21, p. 6202–6208, 3 2021.

5 KANG, X.; WANG, R.; JIANG, M.; LI, E.; LI, Y.; YAN, X.; WANG, T.; REN, Z. Polydopamine functionalized graphene oxide for high sensitivity micro-tapered long period fiber grating sensor and its application in detection CO2+ ions. *Optical Fiber Technology*, v. 68, p. 102807, 1 2022.

6 SINGH, M.; RAGHUWANSHI, S. K.; PRAKASH, O. Ultra-sensitive fiber optic gas sensor using graphene oxide coated long period gratings. *IEEE Photonics Technology Letters*, v. 31, p. 1473–1476, 9 2019.

7 FENG, Y.; PENG, J.; WU, T.; XING, F.; SUN, T. A real-time in situ wafer temperature measurement system based on fiber Bragg grating array. *IEEE Sensors Journal*, v. 24, p. 17733–17741, 6 2024.

8 NAYAK, D. R.; SHARMA, P.; MOHAPATRA, A. G.; NAYAK, N.; KESWANI, B.; KHANNA, A. IoT-driven predictive maintenance approach in industry 4.0. *Fog Computing for Intelligent Cloud IoT Systems*, p. 203–227, 6 2024.

9 MACEDO, L.; LOUZADA, P.; VILLANI, L. G.; FRIZERA, A.; MARQUES, C.; LEAL-JUNIOR, A. Machinery fault diagnosis in electric motors through mechanical vibration monitoring using fiber Bragg grating-based accelerometers. *IEEE Sensors Journal*, 7 2024.

10 HE, S.; WANG, J.; YANG, F.; CHANG, T.-L.; TANG, Z.; LIU, K.; LIU, S.; TIAN, F.; LIANG, J.-F.; DU, H.; LIU, Y. Bacterial detection and differentiation of staphylococcus aureus and escherichia coli utilizing long-period fiber gratings functionalized with nanoporous coated structures. *Coatings*, v. 13, p. 778, 4 2023.

11 JANCZUK-RICHTER, M.; DOMINIK, M.; ROźNIECKA, E.; KOBA, M.; MIKULIC, P.; BOCK, W. J.; ŁOś, M.; ŚMIETANA, M.; NIEDZIółKA-JöNSSON, J. Long-period fiber grating sensor for detection of viruses. *Sensors and Actuators B: Chemical*, v. 250, p. 32–38, 10 2017.

12 ESPOSITO, F.; SANSONE, L.; SRIVASTAVA, A.; BALDINI, F.; CAMPOPIANO, S.; CHIAVAIOLI, F. E.; GIORDANO, M.; GIANNETTI, A. E.; IADICICCO, A. Real time and label-free detection of c-reactive protein in serum by long period grating in double cladding fiber. In: . Editors LIEBERMAN, R. A.; BALDINI, F.; HOMOLA, J. SPIE, c2021. p. 23.

13 GANGWAR, R. K.; KUMARI, S.; PATHAK, A. K.; GUTLAPALLI, S. D.; MEENA, M. C. Optical fiber based temperature sensors: A review. *Optics 2023, Vol. 4, Pages 171-197*, v. 4, p. 171–197, 2 2023.

14 BHATIA, V.; VENGSARKAR, A. M. Optical fiber long-period grating sensors. *Optics Letters*, v. 21, p. 692, 5 1996.

15 SHU, X.; ZHANG, L.; BENNION, I.; SHU, X.; ZHANG, L.; BENNION, I.; SHU, X.; ZHANG, L.; BENNION, I. Sensitivity characteristics of long-period fiber gratings. *Journal of Lightwave Technology*, v. 20, p. 255–266, 2002.

16 COELHO, L.; VIEGAS, D.; SANTOS, J. L.; DE ALMEIDA, J. M. M. M. Detection of extra virgin olive oil thermal deterioration using a long period fibre grating sensor coated with titanium dioxide. *Food and Bioprocess Technology*, v. 8, p. 1211–1217, 6 2015.

17 FILHO, R. L. F.; BARINO, F. O.; CALDERANO, J.; ÍTALO FERNANDO VALLE ALVARENGA; CAMPOS, D.; DOS SANTOS, A. B. In-fiber mach–zehnder interferometer as a promising tool for optical nose and odor prediction during the fermentation process. *Optics Letters*, v. 48, p. 3905, 8 2023.

18 DELGADO-PINAR, M.; SHI, Q.; POVEDA-WONG, L.; DELGADO-PINAR, E.; XU, B.; ZHAO, J.; CRUZ, J. L.; ANDRES, M. V. Oligonucleotide-hybridization fiber-optic biosensor using a narrow bandwidth long period grating. *IEEE Sensors Journal*, v. 17, p. 5503–5509, 9 2017.

19 YAN, J.; FENG, J.; GE, J.; CHEN, J.; WANG, F.; XIANG, C.; WANG, D.; YU, Q.; ZENG, H. Highly sensitive humidity sensor based on a GO/Co-MOF-74 coated long period fiber grating. *IEEE Photonics Technology Letters*, v. 34, p. 77–80, 1 2022.

20 ZHOU, G.; TANG, F.; LI, G.; LIN, Z.; LI, H.-N. Long-period grating fiber optic sensors coated with gold film and pulse-electroplated iron–carbon layer for reinforcing steel corrosion monitoring. *IEEE Transactions on Instrumentation and Measurement*, v. 72, p. 1–11, 2023.

21 NG, M. N.; CHEN, Z.; CHIANG, K. S. Temperature compensation of long-period fiber grating for refractive-index sensing with bending effect. *IEEE Photonics Technology Letters*, 2002.

22 TRONO, C.; BALDINI, F.; BRENCI, M.; CHIAVAIOLI, F.; MUGNAINI, M. Flow cell for strain- and temperature-compensated refractive index measurements by means of cascaded optical fibre long period and Bragg gratings. *Measurement Science and Technology*, 2011.

23 HROMADKA, J.; HAZLAN, N. N. M.; HERNANDEZ, F. U.; CORREIA, R.; NORRIS, A.; MORGAN, S. P.; KORPOSH, S. Simultaneous in situ temperature and relative humidity monitoring in mechanical ventilators using an array of

functionalised optical fibre long period grating sensors. *Sensors and Actuators B: Chemical*, v. 286, p. 306–314, 5 2019.

24 BARINO, F.; DELGADO, F.; JUCá, M. M. A.; COELHO, T. T. V.; DOS SANTOS, A. B. Comparison of regression methods for transverse load sensor based on optical fiber long-period grating. *Measurement*, v. 146, p. 728–735, 11 2019.

25 COLACO, C.; CALDAS, P.; VILLAR, I. D.; CHIBANTE, R.; REGO, G. Arc-induced long-period fiber gratings in the dispersion turning points. *Journal of Lightwave Technology*, v. 34, p. 4584–4590, 10 2016.

26 DE SOUZA DELGADO, F.; DOS SANTOS, A. B. Reduction of intrinsic polarization dependence in arc-induced long-period fiber gratings. *Optical Engineering*, v. 57, p. 1, 6 2018.

27 ESPOSITO, F.; RANJAN, R.; CAMPOPIANO, S.; IADICICCO, A. Experimental study of the refractive index sensitivity in arc-induced long period gratings. *IEEE Photonics Journal*, v. 9, p. 1–10, 2 2017.

28 LING, Q.; GU, Z.; WU, W.; PANG, B. Simultaneous SRI and temperature measurement of FM-LPFG written by CO2 laser. *Optical Fiber Technology*, v. 58, p. 102264, 9 2020.

29 LAN, X.; HAN, Q.; HUANG, J.; WANG, H.; GAO, Z.; KAUR, A.; XIAO, H. Turn-around point long-period fiber grating fabricated by CO2 laser for refractive index sensing. *Sensors and Actuators B: Chemical*, v. 177, p. 1149–1155, 2 2013.

30 LI, D.; ZHOU, Z.; OU, J. Development and sensing properties study of frp–FBG smart stay cable for bridge health monitoring applications. *Measurement*, v. 44, p. 722–729, 5 2011.

31 RAO, Y.-J. Novel mechanical fiber optic sensors based on long-period fiber gratings written by high-frequency CO2 laser pulses. In: . Editors RAO, Y.-J.; JONES, J. D. C.; NARUSE, H.; CHEN, R. I. c2002. p. 43.

32 HU, Q.; ZHAO, X.; TIAN, X.; LI, H.; WANG, M.; WANG, Z.; XU, X. Raman suppression in 5 kw fiber amplifier using long period fiber grating fabricated by CO2 laser. *Optics & Laser Technology*, v. 145, p. 107484, 1 2022.

33 LEE, N.; SONG, J.; PARK, J. Mechanically induced long-period fiber grating array sensor. *Microwave and Optical Technology Letters*, v. 53, p. 2295–2298, 10 2011.

34 ZAHRA, S.; PALMA, P. D.; VITA, E. D.; ESPOSITO, F.; IADICICCO, A.; CAMPOPIANO, S. Investigation of mechanically induced long period grating by 3-d printed periodic grooved plates. *Optics & Laser Technology*, v. 167, p. 109752, 12 2023.

35 BARINO, F. O.; D. SANTOS, A. B.; DOS SANTOS, A. B. LPG interrogator based on FBG array and artificial neural network. *IEEE Sensors Journal*, v. 20, p. 14187–14194, 12 2020.

36 SAMPAIO, G.; BARINO, F. O.; DOS SANTOS, A. B. Long-period fiber grating sensor interrogation with single strain modulated FBG and harmonic analysis. *Optical Fiber Technology*, v. 71, p. 102940, 7 2022.

37 BARINO, F. O.; AGUIAR, E. P. D.; HONóRIO, L. D. M.; SILVA, V. N. H.; LóPEZ-BARBERO, A. P.; SANTOS, A. B. D. A fuzzy approach to LPFG-based optical sensor processing and interrogation. *IEEE Transactions on Instrumentation and Measurement*, v. 71, 2022.

38 BARINO, F. O.; DOS SANTOS, A. B. Addressing uncertainty on machine learning models for long-period fiber grating signal conditioning using monte carlo method. *IEEE Transactions on Instrumentation and Measurement*, v. 73, p. 1–9, 2024.

39 BARINO, F. O.; FARACO-FILHO, R. L.; CAMPOS, D.; DOS SANTOS, A. B. 3d-printed force sensitive structure using embedded long-period fiber grating. *Optics & Laser Technology*, v. 148, p. 107697, 4 2022.

40 FARACO-FILHO, R.; CASTRO, J. V. D.; BARINO, F. O.; CAMPOS, D. E.; SANTOS, A. B. D. Monitoring and characterization technology for coffee fermentation aromas: A data-driven approach. *IEEE Sensors Journal*, v. 24, p. 8371–8378, 3 2024.

41 FILHO, R. L. F.; DE CASTRO, J. V.; BARINO, F. O.; CAMPOS, D.; DOS SANTOS, A. B. Enhanced aroma prediction in coffee fermentation through optical fiber sensor data fusion. *Sensors and Actuators A: Physical*, v. 369, p. 115223, 4 2024.

42 FARACO, R. L.; BARINO, F.; CAMPOS, D.; SAMPAIO, G.; HONóRIO, L.; MARCATO, A.; DOS SANTOS, A. B.; DOS SANTOS, C. C.; HAMAJI, F. Hydroelectric plant safety: Real-time monitoring utilizing fiber-optic sensors. *Sensors 2024, Vol. 24, Page 4601*, v. 24, p. 4601, 7 2024.

43 HAUS, H.; HUANG, W. Coupled-mode theory. *Proceedings of the IEEE*, v. 79, p. 1505–1518, 1991.

44 YIN, G.; WANG, Y.; LIAO, C.; ZHOU, J.; ZHONG, X.; WANG, G.; SUN, B.; HE, J. Long period fiber gratings inscribed by periodically tapering a fiber. *IEEE Photonics Technology Letters*, v. 26, p. 698–701, 4 2014.

45 WONKO, R.; MARć, P.; JAROSZEWICZ, L. R. Fabrication of tapered long period fiber gratings for sensors application by filament heating. In: . Editors DOROSZ, J.; ROMANIUK, R. S. SPIE, c2017. v. 10325. p. 46–50.

46 NAVRUZ, I.; ARI, F.; BILSEL, M.; AL-MASHHADANI, Z. A. Enhancing refractive index sensitivity using micro-tapered long-period fiber grating inscribed in biconical tapered fiber. *Optical Fiber Technology*, v. 45, p. 201–207, 2018.

47 ASKINS, C. G. *Periodic UV-induced index modulations in doped-silica optical fibers: Formation and properties of the fiber Bragg grating*. Dordrecht: Springer Netherlands, 2000. p. 391–426.

48 AHMED, F.; JOE, H.-E.; MIN, B.-K.; JUN, M. B. Characterization of refractive index change and fabrication of long period gratings in pure silica fiber by femtosecond laser radiation. *Optics Laser Technology*, v. 74, p. 119–124, 11 2015.

49 LI, B.; JIANG, L.; WANG, S.; TSAI, H.-L.; XIAO, H. Femtosecond laser fabrication of long period fiber gratings and applications in refractive index sensing. *Optics & Laser Technology*, v. 43, p. 1420–1423, 11 2011.

50 LI, Y.; WEI, T.; MONTOYA, J. A.; SAINI, S. V.; LAN, X.; TANG, X.; DONG, J.; XIAO, H. Measurement of CO2-laser-irradiation-induced refractive index modulation in single-mode fiber toward long-period fiber grating design and fabrication. *Applied Optics*, Woodbury, v. 47, p. 5296, 10 2008.

51 ROCHA, A. M.; MACHADO, A. I.; ALMEIDA, T.; VIEIRA, J.; FACãO, M. Analysis of long period gratings inscribed by CO2 laser irradiation and estimation of the refractive index modulation. *Sensors*, v. 20, p. 6409, 11 2020.

52 MARTINEZ-RIOS, A.; MONZON-HERNANDEZ, D.; TORRES-GOMEZ, I. Highly sensitive cladding-etched arc-induced long-period fiber gratings for refractive index sensing. *Optics Communications*, Amsterdam, v. 283, p. 958–962, 3 2010.

53 SAVIN, S.; DIGONNET, M. J. F.; KINO, G. S.; SHAW, H. J. Tunable mechanically induced long-period fiber gratings. *Optics Letters*, v. 25, p. 710, 5 2000.

54 ZHOU, X.; SHI, S.; ZHANG, Z.; ZOU, J.; LIU, Y. Mechanically-induced -shifted long-period fiber gratings. *Optics Express*, v. 19, p. 6253, 3 2011.

55 RAN, J.; CHEN, Y.; WANG, G.; ZHONG, Z.; ZHANG, J.; XU, O.; HUANG, Q.; LEI, X. Mechanically induced long-period fiber gratings and applications. *Photonics*, v. 11, p. 223, 2 2024.

56 ERDOGAN, T. Fiber grating spectra. *Journal of lightwave technology*, v. 15, p. 1277–1294, 1997.

57 BARINO, F. O. *Sensores ópticos baseados em LPFGs para identificação de condições de carregamento em estruturas*. July 2021. Dissertation (Masters in Electrical Engineering)- Universidade Federal de Juiz de Fora, July 2021.

58 RAO, Y.-J. In-fibre Bragg grating sensors. *Measurement Science and Technology*, v. 8, n. 4, p. 355, apr 1997.

59 CHEN, J.; LIU, B.; ZHANG, H. Review of fiber Bragg grating sensor technology. *Frontiers of Optoelectronics in China*, v. 4, p. 204–212, 6 2011.

60 GUAN, T.; GU, Z.; LING, Q.; FENG, W. Tilted long-period fiber grating strain sensor based on dual-peak resonance near pmtp. *Optics Laser Technology*, v. 114, p. 20–27, 6 2019.

61 LING, Q.; GU, Z.; GAO, K. Smart design of a long-period fiber grating refractive index sensor based on dual-peak resonance near the phase-matching turning point. *Applied Optics*, Woodbury, v. 57, p. 2693, 4 2018.

62 LI, Y.; DU, M.; HE, S.; WANG, R.; ZHANG, Z.; WANG, Q. Sensitive label-free hemoglobin detection based on polydopamine functionalized graphene oxide coated micro-tapered long-period fiber grating. *Optik*, v. 275, p. 170626, 3 2023.

63 LIU, T.; LI, Y.; DAI, X.; GAN, W.; WANG, X.; DAI, S.; SONG, B.; XU, T.; ZHANG, P. Simultaneous detection of temperature, strain, refractive index, and ph based on a phase-shifted long-period fiber grating. *Journal of Lightwave Technology*, v. 41, p. 5169–5180, 8 2023.

64 KANG, X.; WANG, R.; JIANG, M.; LI, E.; LI, Y.; WANG, T.; REN, Z. A label-free biosensor for pepsin detection based on graphene oxide functionalized micro-tapered long period fiber grating. *Sensors and Actuators Reports*, v. 5, p. 100139, 6 2023.

65 DYANKOV, G.; EFTIMOV, T.; HIKOVA, E.; NAJDENSKI, H.; KUSSOVSKI, V.; GENOVA-KALOU, P.; MANKOV, V.; KISOV, H.; VESELINOV, P.; GHAFFARI, S. S.; KOVACHEVA-SLAVOVA, M.; VLADIMIROV, B.; MALINOWSKI, N. SPR and double resonance LPG biosensors for helicobacter pylori BabA antigen detection. *Sensors*, v. 24, p. 2118, 3 2024.

66 REN, K.; JIA, A.; HU, J.; LI, G.; WANG, W.; LI, M.; HAN, D.; ZHENG, Y.; LI, J.; LIANG, L. Polyvinyl alcohol nanofibers wrapped microtapered long-period fiber grating for high-linearity humidity and temperature sensing. *IEEE Sensors Journal*, v. 24, p. 6279–6285, 3 2024.

67 CUSANO, A.; IADICICCO, A.; PILLA, P.; CONTESSA, L.; CAMPOPIANO, S.; CUTOLO, A.; GIORDANO, M.; GUERRA, G. Coated long-period fiber gratings as high-sensitivity optochemical sensors. *Journal of Lightwave Technology*, v. 24, n. 4, p. 1776–1786, 2006.

68 WANG, J.-N.; TANG, J.-L. Feasibility of fiber Bragg grating and long-period fiber grating sensors under different environmental conditions. *Sensors*, v. 10, p. 10105–10127, 11 2010.

69 GUO, Z.; BAI, Y.; ZHANG, W.; LIU, S.; PAN, Y.; ZHANG, X.; ZHANG, J.; CHEN, H.; LI, X. Temperature compensated magnetic field sensor based on magnetic fluid infiltrated cascaded structure of micro-tapered long-period fiber grating and fiber Bragg grating. *Sensors and Actuators A: Physical*, v. 358, p. 114425, 8 2023.

70 DU, J.; GU, Z.; LING, Q.; WANG, Y.; NIE, W. Design of an anti-temperature interference liquid level sensor based on tilt long-period fiber grating. *Optics Laser Technology*, v. 177, p. 111229, 10 2024.

71 DELGADO, F. S.; DOS SANTOS, A. B. Multi-measurement scheme for a fiber-optic sensor based on a single long-period grating. *Journal of Modern Optics*, v. 64, p. 2428–2432, 11 2017.

72 ESPOSITO, F.; SRIVASTAVA, A.; IADICICCO, A.; CAMPOPIANO, S. Multi-parameter sensor based on single long period grating in panda fiber for the simultaneous measurement of SRI, temperature and strain. *Optics Laser Technology*, v. 113, p. 198–203, 5 2019.

73 Redondo Optics Inc. Fiber Bragg Grating Transceivers. `redondooptics.com/fbg-transceiver` [Accessed: December 18, 2024].

74 Luna Innovations. High-speed multipoint fiber optic sensing. `lunainc.com/product-category/sensing-and-non-destructive-test-products?family=78#category-14` [Accessed: December 18, 2024].

75 Ibsen photonics. Interrogation monitors. `ibsen.com/products/interrogation-monitors` [Accessed: December 18, 2024].

76 Smart Fibres Ltd. Our products. `smartfibres.com/products` [Accessed: December 18, 2024].

77 HBM Hottinger Brüel & Kjaer GmbH. Optical interrogators. `hbm.com/en/2322/optical-interrogators/` [Accessed: December 18, 2024].

78 ALLSOP, T.; GILLOOLY, A.; MEZENTSEV, V.; EARTHGROWL-GOULD, T.; NEAL, R.; WEBB, D.; BENNION, I. Bending and orientational characteristics of long period gratings written in D-shaped optical fiber. *IEEE Transactions on Instrumentation and Measurement*, v. 53, p. 130–135, 2 2004.

79 TORRES-GóMEZ, I.; MARTíNEZ-RIOS, A.; ANZUETO-SáNCHEZ, G.; CEBALLOS-HERRERA, D. E.; SALCEDA-DELGADO, G. Transverse load and temperature sensing using multiplexed long-period fiber gratings. *Photonics*, v. 8, p. 1, 12 2020.

80 WENG, S.; YUAN, P.; ZHUANG, W.; ZHANG, D.; LUO, F.; ZHU, L. SOI-based multi-channel AWG with fiber Bragg grating sensing interrogation system. *Photonics 2021, Vol. 8, Page 214*, v. 8, p. 214, 6 2021.

81 CHEN, S.; CHEN, S.; YAO, F.; YAO, F.; REN, S.; REN, S.; WANG, G.; WANG, G.; WANG, G.; HUANG, M.; HUANG, M.; HUANG, M. Cost-effective improvement of the performance of AWG-based FBG wavelength interrogation via a cascaded neural network. *Optics Express, Vol. 30, Issue 5, pp. 7647-7663*, v. 30, p. 7647–7663, 2 2022.

82 GUO, H.; XIAO, G.; YAO, J. Interrogation of a long period grating fiber sensor with an arrayed-waveguide-grating-based demultiplexer through curve fitting. *IEEE Sensors Journal*, v. 8, p. 1771–1775, 11 2008.

83 PATRICK, H.; WILLIAMS, G.; KERSEY, A.; PEDRAZZANI, J.; VENGSARKAR, A. Hybrid fiber Bragg grating/long period fiber grating sensor for strain/temperature discrimination. *IEEE Photonics Technology Letters*, v. 8, p. 1223–1225, 9 1996.

84 FALLON, R. W.; ZHANG, L.; EVERALL, L. A.; WILLIAMS, J. A. R.; BENNION, I. All-fibre optical sensing system: Bragg grating sensor interrogated by a long-period grating. *Measurement Science and Technology*, v. 9, n. 12, p. 1969, dec 1998.

85 RAN, Z.-L.; RAO, Y.-J. A FBG sensor system with cascaded LPFGs and music algorithm for dynamic strain measurement. *Sensors and Actuators A: Physical*, v. 135, n. 2, p. 415–419, 2007.

86 JIA, B.; DENG, X.; DU, C.; LU, H.; QIN, Z.; CUI, L.; ZHANG, L.; YANG, Y.; ZHANG, M. Wide wavelength range demodulation method of cascaded fbgs based on lpfg spectral control. *Journal of Lightwave Technology*, v. 42, n. 17, p. 6090–6098, 2024.

87 ALLSOP, T.; EARTHROWL, T.; REEVES, R.; WEBB, D. J.; BENNION, I. The interrogation and multiplexing of long period grating curvature sensors using a Bragg grating based, derivative spectroscopy technique. *Measurement Science and Technology*, v. 15, p. 44, 2003.

88 SHIN, C.-S.; CHIANG, C.-C.; LIAW, S.-K. Comparison of single and double cladding long period fiber grating sensor using an intensity modulation interrogation system. *Optics Communications*, Amsterdam, v. 258, p. 23–29, 2 2006.

89 DOS SANTOS, P.; JORGE, P.; DE ALMEIDA, J.; COELHO, L. Low-cost interrogation system for long-period fiber gratings applied to remote sensing. *Sensors*, v. 19, p. 1500, 3 2019.

90 DOS SANTOS, P. S. S.; JORGE, P. A. S.; DE ALMEIDA, J. M. M. M.; COELHO, L. A simple spectral interrogation system for optical fiber sensors. In: . MDPI, c2019. p. 6.

91 SILVA, L. H.; SANTOS, P.; COELHO, L. C. C.; JORGE, P.; BAPTISTA, J. M. Development of a long period fiber grating interrogation system using a multimode laser diode. *Sensors*, v. 21, p. 749, 1 2021.

92 ARAúJO, J. C. C.; DIAS, B.; DOS SANTOS, P. S. S.; DE ALMEIDA, J. M. M. M.; COELHO, L. C. C. Development of a low-cost interrogation system using a mems fabry-pérot tunable filter. *Journal of Physics: Conference Series*, v. 2407, p. 012008, 12 2022.

93 RADFORD, A.; NARASIMHAN, K.; SALIMANS, T.; SUTSKEVER, I. Improving language understanding with unsupervised learning. 2018.

94 THIRUNAVUKARASU, A. J.; TING, D. S. J.; ELANGOVAN, K.; GUTIERREZ, L.; TAN, T. F.; TING, D. S. W. Large language models in medicine. *Nature Medicine*, v. 29, p. 1930–1940, 8 2023.

95 JABLONKA, K. M.; SCHWALLER, P.; ORTEGA-GUERRERO, A.; SMIT, B. Leveraging large language models for predictive chemistry. *Nature Machine Intelligence 2024 6:2*, v. 6, p. 161–169, 2 2024.

96 CHAFAI, N.; BONIZZI, L.; BOTTI, S.; BADAOUI, B. Emerging applications of machine learning in genomic medicine and healthcare. *Critical Reviews in Clinical Laboratory Sciences*, v. 61, p. 140–163, 2024.

97 DEGROAT, W.; ABDELHALIM, H.; PATEL, K.; MENDHE, D.; ZEESHAN, S.; AHMED, Z. Discovering biomarkers associated and predicting cardiovascular disease with high accuracy using a novel nexus of machine learning techniques for precision medicine. *Scientific Reports 2024 14:1*, v. 14, p. 1–13, 1 2024.

98 GIUDICI, P.; CENTURELLI, M.; TURCHETTA, S. Artificial intelligence risk measurement. *Expert Systems with Applications*, v. 235, p. 121220, 1 2024.

99 SONKAVDE, G.; DHARRAO, D. S.; BONGALE, A. M.; DEOKATE, S. T.; DORESWAMY, D.; BHAT, S. K. Forecasting stock market prices using machine learning and deep learning models: A systematic review, performance analysis and discussion of implications. *International Journal of Financial Studies*, v. 11, p. 94, 7 2023.

100 WEBER, P.; CARL, K. V.; HINZ, O.; CARL, K. V.; HINZ, O.; WEBER, P. Applications of explainable artificial intelligence in finance—a systematic review of finance, information systems, and computer science literature. *Management Review Quarterly 2023 74:2*, v. 74, p. 867–907, 2 2023.

101 LIPTON, Z. C. The mythos of model interpretability. *Queue*, v. 16, p. 31–57, 6 2018.

102 MESSERI, L.; CROCKETT, M. J. Artificial intelligence and illusions of understanding in scientific research. *Nature*, London, v. 627, p. 49–58, 3 2024.

103 MCCULLOCH, W. S.; PITTS, W. A logical calculus of the ideas immanent in nervous activity. *The Bulletin of Mathematical Biophysics*, v. 5, p. 115–133, 12 1943.

104 ROSENBLATT, F. The perceptron: a probabilistic model for information storage and organization in the brain. *Psychological review*, v. 65 6, p. 386–408, 1958.

105 HORNIK, K.; STINCHCOMBE, M.; WHITE, H. et al. Multilayer feedforward networks are universal approximators. *Neural networks*, v. 2, p. 359–366, 1989.

106 ATTALI, J.-G.; PAGèS, G. Approximations of functions by a multilayer perceptron: a new approach. *Neural networks*, v. 10, p. 1069–1081, 1997.

107 CASTRO, J. L.; MANTAS, C. J.; BEN, J. M. Neural networks with a continuous squashing function in the output are universal approximators. *Neural Networks*, v. 13, p. 561–563, 2000.

108 HAYKIN, S. *Neural networks and learning machines*. Prentice Hall, 2008.

109 CARUANA, R.; LAWRENCE, S.; GILES, C. Overfitting in neural nets: Backpropagation, conjugate gradient, and early stopping. In: . Editors LEEN, T.; DIETTERICH, T.; TRESP, V. MIT Press, c2000. v. 13.

110 YAO, Y.; ROSASCO, L.; CAPONNETTO, A. On early stopping in gradient descent learning. *Constructive Approximation*, v. 26, p. 289–315, 8 2007.

111 YING, X. An overview of overfitting and its solutions. *Journal of Physics: Conference Series*, v. 1168, p. 022022, 2 2019.

112 PEDREGOSA, F.; VAROQUAUX, G.; GRAMFORT, A.; MICHEL, V.; THIRION, B.; GRISEL, O.; BLONDEL, M.; PRETTENHOFER, P.; WEISS, R.; DUBOURG, V.; VANDERPLAS, J.; PASSOS, A.; COURNAPEAU, D.; BRUCHER, M.; PERROT, M.; DUCHESNAY, E. Scikit-learn: Machine learning in Python. *Journal of Machine Learning Research*, v. 12, p. 2825–2830, 2011.

113 CAO, J.; ZHOU, T.; ZHI, S.; LAM, S.; REN, G.; ZHANG, Y.; WANG, Y.; DONG, Y.; CAI, J. Fuzzy inference system with interpretable fuzzy rules: Advancing explainable artificial intelligence for disease diagnosis—a comprehensive review. *Information Sciences*, v. 662, p. 120212, 3 2024.

114 GUERRA, M. I. S.; DE ARAúJO, F. M. U.; DE CARVALHO NETO, J. T.; VIEIRA, R. G. Survey on adaptative neural fuzzy inference system (anfis) architecture applied to photovoltaic systems. *Energy Systems*, v. 15, p. 505–541, 5 2024.

115 SHARMA, R. P.; DHARAVATH, R.; EDLA, D. R. Ioft-fis: Internet of farm things based prediction for crop pest infestation using optimized fuzzy inference system. *Internet of Things*, v. 21, p. 100658, 4 2023.

116 GERAMIAN, A.; ABRAHAM, A. Customer classification: A mamdani fuzzy inference system standpoint for modifying the failure mode and effect analysis based three dimensional approach. *Expert Systems with Applications*, v. 186, p. 115753, 12 2021.

117 NAYAK, P.; VATHASAVAI, B. Energy efficient clustering algorithm for multi-hop wireless sensor network using type-2 fuzzy logic. *IEEE Sensors Journal*, v. 17, p. 4492–4499, 7 2017.

118 ZHAO, T.; LI, P.; CAO, J. Soft sensor modeling of chemical process based on self-organizing recurrent interval type-2 fuzzy neural network. *ISA Transactions*, v. 84, p. 237–246, 1 2019.

119 WANG, J.; QIU, K.; WANG, R.; ZHOU, X.; GUO, Y. Development of soft sensor based on sequential kernel fuzzy partitioning and just-in-time relevance vector machine for multiphase batch processes. *IEEE Transactions on Instrumentation and Measurement*, v. 70, p. 1–10, 2021.

120 ÁNGEL LóPEZ MEDINA, M.; ESPINILLA, M.; PAGGETI, C.; QUERO, J. M. Activity recognition for iot devices using fuzzy spatio-temporal features as environmental sensor fusion. *Sensors*, v. 19, p. 3512, 8 2019.

121 ZHU, J.; TANG, Y.; SHAO, X.; XIE, Y. Multisensor fusion using fuzzy inference system for a visual-imu-wheel odometry. *IEEE Transactions on Instrumentation and Measurement*, v. 70, p. 1–16, 2021.

122 LI, H.; WANG, Z.; FORREST, J. Y.-L.; JIANG, W. Low-velocity impact localization on composites under sensor damage by interpolation reference database and fuzzy evidence theory. *IEEE Access*, v. 6, p. 31157–31168, 2018.

123 QIAN, M.; YU, Y.; REN, N.; WANG, J.; JIN, X. Sliding sensor using fiber Bragg grating for mechanical fingers. *Optics Express*, v. 26, p. 254, 1 2018.

124 FU, Z.; ZHAO, Y.; BAO, H.; ZHAO, F. Dynamic deformation reconstruction of variable section WING with fiber Bragg grating sensors. *Sensors*, v. 19, p. 3350, 7 2019.

125 HU, X.; SI, H.; SHEN, H.; YU, Z. A fuzzy neural network model to determine axial strain measured by a long-period fiber grating sensor. *Measurement and Control*, v. 53, p. 704–710, 3 2020.

126 ZADEH, L. Fuzzy sets. *Information and Control*, v. 8, p. 338–353, 6 1965.

127 MAMDANI, E.; ASSILIAN, S. An experiment in linguistic synthesis with a fuzzy logic controller. *International Journal of Man-Machine Studies*, v. 7, p. 1–13, 1 1975.

128 TAKAGI, T.; SUGENO, M. Fuzzy identification of systems and its applications to modeling and control. *IEEE Transactions on Systems, Man, and Cybernetics*, v. SMC-15, p. 116–132, 1 1985.

129 ARSLAN, A.; KAYA, M. Determination of fuzzy logic membership functions using genetic algorithms. *Fuzzy Sets and Systems*, v. 118, p. 297–306, 3 2001.

130 KOMPA, B.; SNOEK, J.; BEAM, A. L. Second opinion needed: communicating uncertainty in medical machine learning. *npj Digital Medicine 2021 4:1*, v. 4, p. 1–6, 1 2021.

131 CHUA, M.; KIM, D.; CHOI, J.; LEE, N. G.; DESHPANDE, V.; SCHWAB, J.; LEV, M. H.; GONZALEZ, R. G.; GEE, M. S.; DO, S. Tackling prediction uncertainty in machine learning for healthcare. *Nature Biomedical Engineering 2022 7:6*, v. 7, p. 711–718, 12 2022.

132 SEONI, S.; JAHMUNAH, V.; SALVI, M.; BARUA, P. D.; MOLINARI, F.; ACHARYA, U. R. Application of uncertainty quantification to artificial intelligence in healthcare: A review of last decade (2013–2023). *Computers in Biology and Medicine*, v. 165, p. 107441, 10 2023.

133 SHAFAEI, S.; KUGELE, S.; OSMAN, M. H.; KNOLL, A. Uncertainty in machine learning: A safety perspective on autonomous driving. *Lecture Notes in Computer Science (including subseries Lecture Notes in Artificial Intelligence and Lecture Notes in Bioinformatics)*, v. 11094 LNCS, p. 458–464, 2018.

134 MICHELMORE, R.; WICKER, M.; LAURENTI, L.; CARDELLI, L.; GAL, Y.; KWIATKOWSKA, M. Uncertainty quantification with statistical guarantees in end-to-end autonomous driving control. *Proceedings - IEEE International Conference on Robotics and Automation*, p. 7344–7350, 5 2020.

135 YANG, K.; TANG, X.; QIU, S.; JIN, S.; WEI, Z.; WANG, H. Towards robust decision-making for autonomous driving on highway. *IEEE Transactions on Vehicular Technology*, v. 72, p. 11251–11263, 9 2023.

136 HOEL, C. J.; WOLFF, K.; LAINE, L. Ensemble quantile networks: Uncertainty-aware reinforcement learning with applications in autonomous driving. *IEEE Transactions on Intelligent Transportation Systems*, v. 24, p. 6030–6041, 6 2023.

137 ABRECHT, S.; HIRSCH, A.; RAAFATNIA, S.; WOEHRLE, M. Deep learning safety concerns in automated driving perception. *IEEE Transactions on Intelligent Vehicles*, p. 1–12, 2024.

138 HüLLERMEIER, E.; WAEGEMAN, W. Aleatoric and epistemic uncertainty in machine learning: an introduction to concepts and methods. *Machine Learning*, v. 110, p. 457–506, 3 2021.

139 LAMPINEN, J.; VEHTARI, A. Bayesian approach for neural networks—review and case studies. *Neural Networks*, v. 14, p. 257–274, 4 2001.

140 LAKSHMINARAYANAN, B.; PRITZEL, A.; DEEPMIND, C. B. Simple and scalable predictive uncertainty estimation using deep ensembles. In: . c2017. p. 6405–6416.

141 SENSOY, M.; KAPLAN, L.; KANDEMIR, M. Evidential deep learning to quantify classification uncertainty. *Advances in Neural Information Processing Systems*, p. 3179–3189, 2018.

142 ABDAR, M.; POURPANAH, F.; HUSSAIN, S.; REZAZADEGAN, D.; LIU, L.; GHAVAMZADEH, M.; FIEGUTH, P.; CAO, X.; KHOSRAVI, A.; ACHARYA, U. R.; MAKARENKOV, V.; NAHAVANDI, S. A review of uncertainty quantification in deep learning: Techniques, applications and challenges. *Information Fusion*, v. 76, p. 243–297, 12 2021.

143 THEODORIDIS, S.; KOUTROUMBAS, K. *Pattern recognition.* Academic Press, 2008.

144 NASIR, V.; SASSANI, F. A review on deep learning in machining and tool monitoring: methods, opportunities, and challenges. *The International Journal of Advanced Manufacturing Technology 2021 115:9*, v. 115, p. 2683–2709, 5 2021.

145 TAIEBAT, M.; SASSANI, F. Distinguishing sensor faults from system faults by utilizing minimum sensor redundancy. *Transactions of the Canadian Society for Mechanical Engineering*, v. 41, n. 3, p. 469–487, 2017.

146 DIEZ-OLIVAN, A.; SER, J. D.; GALAR, D.; SIERRA, B. Data fusion and machine learning for industrial prognosis: Trends and perspectives towards industry 4.0. *Information Fusion*, v. 50, p. 92–111, 10 2019.

147 BOIKOV, A.; PAYOR, V.; SAVELEV, R.; KOLESNIKOV, A. Synthetic data generation for steel defect detection and classification using deep learning. *Symmetry 2021, Vol. 13, Page 1176*, v. 13, p. 1176, 6 2021.

148 MERRIFIELD, T. P.; GRIFFITH, D. P.; ZAMANIAN, S. A.; GESBERT, S.; SEN, S.; DE, J.; GUZMAN, L. T.; POTTER, R. D.; KUEHL, H. Synthetic seismic data for training deep learning networks. 2022.

149 RAJOTTE, J.-F.; BERGEN, R.; BUCKERIDGE, D. L.; EMAM, K. E.; NG, R.; STROME, E. Synthetic data as an enabler for machine learning applications in medicine. *iSCIENCE*, v. 25, p. 105331, 2022.

150 THEODOROU, D.; MELIGOTSIDOU, L.; KARAVOLTSOS, S.; BURNETAS, A.; DASSENAKIS, M.; SCOULLOS, M. Comparison of iso-gum and monte carlo methods for the evaluation of measurement uncertainty: Application to direct cadmium measurement in water by gfaas. *Talanta*, v. 83, p. 1568–1574, 2 2011.

151 MAHMOUD, G. M.; HEGAZY, R. S. Comparison of gum and monte carlo methods for the uncertainty estimation in hardness measurements. *International Journal of Metrology and Quality Engineering*, v. 8, p. 14, 2017.

152 CHEN, A.; CHEN, C. Comparison of gum and monte carlo methods for evaluating measurement uncertainty of perspiration measurement systems. *Measurement*, v. 87, p. 27–37, 6 2016.

153 LEE, Y.; OH, S. H. Input noise immunity of multilayer perceptrons. *ETRI Journal*, v. 16, p. 35–43, 4 1994.

154 REN, S.; CHEN, S.; HU, Y.; XU, H.; HOU, X.; YANG, Q.; WANG, G.; ZHANG, Y. Rethink training: Synthetic data powers efficient fiber-optics sensor demodulation neural networks. *IEEE Sensors Journal*, v. 24, p. 31408–31416, 10 2024.

155 VASWANI, A.; SHAZEER, N.; PARMAR, N.; USZKOREIT, J.; JONES, L.; GOMEZ, A. N.; KAISER, L. U.; POLOSUKHIN, I. Attention is all you need. In: . Editors GUYON, I.; LUXBURG, U. V.; BENGIO, S.; WALLACH, H.; FERGUS, R.; VISHWANATHAN, S.; GARNETT, R. Curran Associates, Inc., c2017. v. 30.

156 NIU, Z.; ZHONG, G.; YU, H. A review on the attention mechanism of deep learning. *Neurocomputing*, v. 452, p. 48–62, 9 2021.

157 CHOLLET, F. et al. Keras. `https://keras.io`, 2015.

158 KINGMA, D. P.; BA, J. Adam: A method for stochastic optimization. *arXiv preprint arXiv:1412.6980*, 2014.

159 GAL, Y.; GHAHRAMANI, Z. Dropout as a bayesian approximation: Representing model uncertainty in deep learning. In: . Editors BALCAN, M. F.; WEINBERGER, K. Q. New York, New York, USA: PMLR, c2016. v. 48 of *Proceedings of Machine Learning Research*. p. 1050–1059.